Quantum Dots and Doped Nanocrystals:

Synthesis, Optical Properties and Bio-applications

Cover art designed by Yaqin Yuan and Yiming Zhao

This thesis was funded by the “Nederlandse Organisatie voor Wetenschappelijk onderzoek (NWO) Chemische wetenschappen (CW)” (ECHO.06.B.047) and by the European Union 7th framework programme” NanoSpec” program (NMP-2009-1.2-1)
Printed by Ipskamp Drukkers
ISBN: 978-90-393-5975-4

Quantum Dots and Doped Nanocrystals:

Synthesis, Optical Properties and Bio-applications

Quantum Dots en Gedoteerde Nanokristallen:

Synthese, Optische Eigenschappen en Bio-toepassingen

(met een samenvatting in het Nederlands)

Proefschrift

ter verkrijging van de graad van doctor aan de Universiteit Utrecht op gezag van de rector magnificus, prof. dr. G.J. van der Zwaan, ingevolge het besluit van het college voor promoties in het openbaar te verdedigen op dinsdag 4 juni 2013 des middags te 12.45 uur

door

Yiming Zhao

geboren op 30 augustus 1985, te Wuhan, China

Promotoren:	Prof. dr. A. Meijerink
	Prof. dr. W.J.M. Mulder
Co-promotor:	Dr. C. de Mello Donegá

Contents

CHAPTER 1

Fundamentals and Bio-applications of Luminescent Nanocrystals

1.1 Introduction

Nanoscience and nanotechnology involve investigation and manipulation of matter on nanometer length scales (typically defined as 1-100 nm) and has led to the discovery of new phenomena and resulted in new applications.[1] It is one of fastest-growing research areas today and broadly considered to have tremendous developmental potential to offer new solutions and new applications in diverse fields, ranging from high tech electronics to probing disease at the molecular level. Therefore, it is not surprising that nanoscience and nanotechnology attract increasing investments from both governments and industries around the world.[2]

Research on colloidal nanocrystals (NCs) plays a central role in nanoscience and involves contributions from many disciplines, including chemistry, physics, biology and medicine. In chemistry, it is interesting and challenging to synthesize and tailor the properties of nanomaterials with high accuracy and reproducibility, in order to create new materials and new structures.[3] In physics, when the crystal enters the nanoscale size regime, spatial confinement effects give rise to size-dependent electronic, magnetic and optical properties.[4, 5] Further, the increase of surface-to-volume ratio is an important aspect for nanomaterials that is crucial for the efficiency for surface reactions and leads to a widespread application of nanomaterials in catalysis.[6] Finally, owing to their excellent chemical and physical properties, colloidal nanocrystals have great potential in bio-nanotechnology and nanomedicine for both diagnostic and therapeutic purposes.[7] On the other hand, the specific and stringent requirements for the different bio-applications bring new chemical and physical challenges. Research on colloidal nanocrystals, as well as on other nanomaterials, is thus highly interdisciplinary and integrative.[8]

This thesis focuses on luminescent nanocrystals, including lanthanide doped nanocrystals and semiconductor nanocrystals. The research involves the synthesis, optical properties and bio-applications. Prior to the experimental studies in the following chapters, a general introduction covering essential background information will be given in this chapter. The first part of this introduction explains the basic physics of the luminescence properties and the synthesis of semiconductor nanocrystals and lanthanide doped nanocrystals, respectively. The second part focuses on the bio-applications of luminescent nanoparticles, and covers the nanoparticles' biocompatibility, *in vivo* fluorescence imaging and targeting principles in cancer and atherosclerosis.

1.2 Semiconductor nanocrystals

1.2.1. Size-dependent optical properties of QDs

An important class of nanomaterials are semiconductor nanocrystals or quantum dots (QDs). The most distinct or “well-known” feature for QDs is their size-dependent photoluminescence color. As depicted in Figure 1.1, the emission color of CdSe QDs changes from red to blue along with decreasing the QD size. In order to understand these unique properties, in this section the basic physics will be given on the relation between size and the optical properties related to electronic structure of QDs. [9]

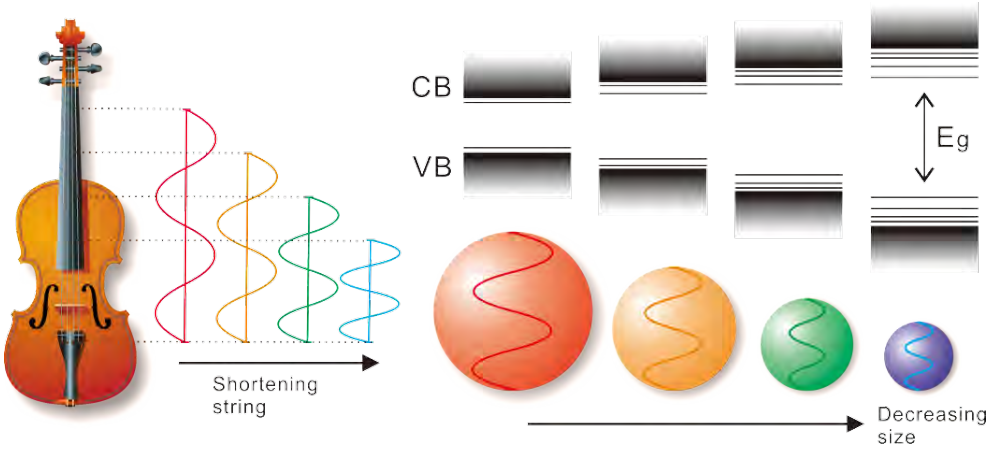

Figure 1.1. Schematic illustration of the quantum confinement effect in CdSe QDs. An analogy with a string instrument is presented on the left: decreasing the string length will produce sound waves with higher frequencies. In QDs a decrease in the size of a QD will reduce the size of exciton, resulting in the absorption and emission of light with higher frequencies (shorter wavelengths).

Nanocrystals bridge the gap between large molecules or clusters of atoms and bulk materials. The properties of NCs can also bridge this gap and may show size dependent properties varying from bulk properties to molecular or atomic like behavior. In the case of semiconductor NCs the change in properties can be described by a confinement of wave functions that exist in bulk semiconductors in a box (the nanocrystal) that is smaller than the wave functions in the bulk. This is

called the “top-down” approach. In another approach (bottom-up) the semiconductor NC can be described as a large molecule or a cluster built up by an increasing number of atoms. Here the top-down approach will be described to provide insight in the size-dependent optical properties of QDs.

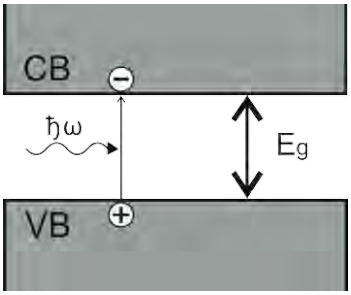

Figure 1.2. Simplified electronic structure of semiconductor with a band gap E_g, and an exciton is generated by excitation with a photon of energy ħω.

In the electronic band structure of semiconductor materials, an energy gap between electron states exists, which is called band gap, E_g. As illustrated in Figure 1.2, energy levels within the band gap do not exist, while in the band there is a continuum of energy levels. The lowest occupied energy band is called valence band (VB), and the highest unoccupied energy band is called conduction band (CB). For semiconductors, the band gap is typically smaller than 3 eV. An electron in the VB can be excited into the CB by absorption of a photon (electrical or thermal excitation are also possible). The promotion of the electron into the CB leaves a positively charged hole in the VB (Figure 1.2). The electron and hole are associated into a pair through Coulomb interactions forming an “exciton”. Since the exciton is a solid-state analogue of a hydrogen atom, the concept of Bohr radius a_B* can be used to describe the average distance between the electron and the hole. The Bohr radius of an exciton is often between 1-10 nm, depending on the material. Therefore, when the size of the semiconductor is close to or smaller than the Bohr radius, the exciton will be confined. This confinement can exist in different dimensions, *e.g.* in one dimension (1D) in thin films or nanoplatelets,[10] in two dimensions (2D) in nanorods [11] and nanowires,[12] or in three dimensions (3D) in quantum dots. The band gap of a QD, which is the lowest exciton energy, can be described as a sum of the band gap of bulk material (E_g^0) and the confinement energy for the electron and hole (E_{1s}^e and E_{1s}^h):

$$E_g^{NC} = E_g^0 + E_{1s}^e + E_{1s}^h = E_g^0 + \frac{\hbar^2 \chi_{nl}^2}{2m_e^* D^2} + \frac{\hbar^2 \chi_{nl}^2}{2m_h^* D^2} \quad (1.1)$$

where m_e^*, m_h^* are the effective masses of the electron and the hole, χ_{nl}^2 are the roots of Bessel functions (which depend on specific quantum numbers [9]), and *D* is the diameter of the NC. Therefore, from equation 1.1 we can see that as a result of this confinement, the NC band gap increases when the particle size decreases. Equation 1.1 also explains the aforementioned quantum size effect in Figure 1.1. To illustrate this effect, an analogy with a string instrument can be applied (Figure 1.1): shortening the string length will lead to sound waves with higher frequencies. In QDs, a decrease in the size of QD will reduce the size of exciton, resulting in the absorption and emission of light with higher frequencies, thus shorter wavelengths.

1.2.2 Core-shell quantum dots

The QDs applied in most biomedical applications are core-shell structures, which are composed of a quantum dot core of one material and a shell of a different material. The single-component QD passivated with organic ligands usually has low luminescence quantum efficiency due to surface trap states. Therefore, the original idea of growing an inorganic shell epitaxially around a QD core is to further passivate the surface trap state to enhance the quantum yield. In addition, the outer shell with chemically more stable materials also acts as a shield protecting the core from oxidation under ambient conditions. Moreover, through changing size, shape and composition of core and shell materials, the band alignment of core-shell QDs can be altered, which offers another approach to tune their luminescence properties. Here different types of core-shell structures and their physical properties are described.

Depending on the relative band alignment of the core and shell materials, after photoexcitation, three types of localization of the charge carriers can be identified, Type I, TypeI$^{1/2}$, and Type II.[13] A schematic representation of the band alignment and charge carriers' localization regimes is depicted in Figure 1.3. For Type I core-shell QDs, the band gap of the shell material is larger than that of the core, and hence both electrons and holes are confined in the core. In this case, the shell is used to passivate the NC surface by reducing the dangling bonds that can act as surface trap states. For example, CdSe/ZnS QDs, which possess a type I band alignment, are one of the earliest developed core-shell structures[14] and are still the most popular air-stable core-shell QDs for both fundamental research and bio-

applications. Although in a Type I NC, the wave-functions of the electron and hole are confined in the core and unaffected by the shell growth, the finite energy offset between the core and shell will allow the leakage of wave functions into the shell. As a result, a small red shift of absorption and emission spectra is observed with the shell growth.

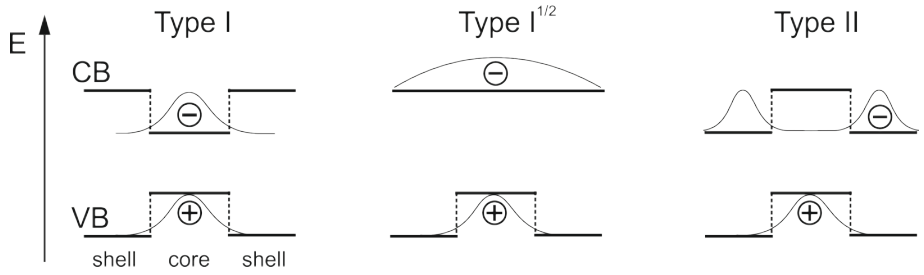

Figure 1.3. Schematic representation of the band alignment of three types of core-shell QDs, and the corresponding localization of electron and hole wave functions.

Type $I^{1/2}$ core-shell QDs, in earlier publications, were also referred as Type I QDs. However, for Type $I^{1/2}$ QDs, the clear difference is that the energy offset of conduction band (or valence band) is too small to confine the electron wave function, and therefore the wave function is delocalized over the whole core-shell structure, while the hole is still confined in the core. A typical example is a CdSe/CdS core-shell NC, and also CdSe/CdS dot core/rod shell nanorods (studied in Chapter 4) are Type $I^{1/2}$ structures.

A Type II core-shell QDs can be achieved by tuning the core size and shell thickness of different core-shell combinations: *e.g*. CdTe/CdSe, CdSe/ZnTe and ZnSe/CdS. Due to the special band alignment (Figure 1.3), the electron and hole wave functions are confined separately in the core and the shell. The reduced overlap between the electron and hole wave functions decreases the recombination rate of exciton and leads to longer radiative lifetimes. The staggered band alignment also makes the spatially indirect gap smaller than the band gap of either the core or the shell materials, and a significant red shift of the emission peak is observed upon growing the shell. These properties make Type II core-shell QDs promising materials that emit in the near-infrared (NIR) range (see the NIR QD for *in vivo* NIR imaging in Chapter 7). Moreover, Type II core-shell QDs also have a large Stokes shift and well separated absorption and emission spectra, which can be beneficial for application in luminescent solar concentrators, since they have the potential to minimize the efficiency losses induced by self-absorption. [15]

1.2.3 Colloidal synthesis of semiconductor nanocrystals

The general principle for the production of monodisperse colloids needs a temporal separation of nucleation events and the subsequent growth of particles on the nuclei generated (Figure 1.4)[16]. In heterogeneous nucleation conditions, the particle growth proceeds by deposition of material on already existing "seed" crystals in solution (region III in Figure 1.4). The key issues to achieve monodispersity with this method are having monodisperse seeds and keeping a low monomer concentration, which prevents the formation of new nuclei by homogeneous nucleation. In homogeneous nucleation conditions, the monodispersity is achieved by a fast nucleation burst and the subsequent crystal growth without further nucleation processes. To achieve the nucleation burst, normally two approaches are used, namely the "hot-injection" method [17] and the "heating-up" method [18], since temperature is the key parameter to control the reactivity of precursors. The precursors decompose thermally and release monomers. Either by rapidly injecting the precursors into the hot solution or by heating the reaction solution above the precursors' decomposition temperature, the concentration of monomers suddenly increases above the nucleation threshold (region I in Figure 1.4), creating a super-saturation, which drives the nucleation (region II in Figure 1.4). Due to the consumption of precursors or by a sudden decrease of reaction temperature (or both) during the nucleation period, the concentration of monomers falls below the nucleation threshold and the nucleation process stops (region III in Figure 1.4).

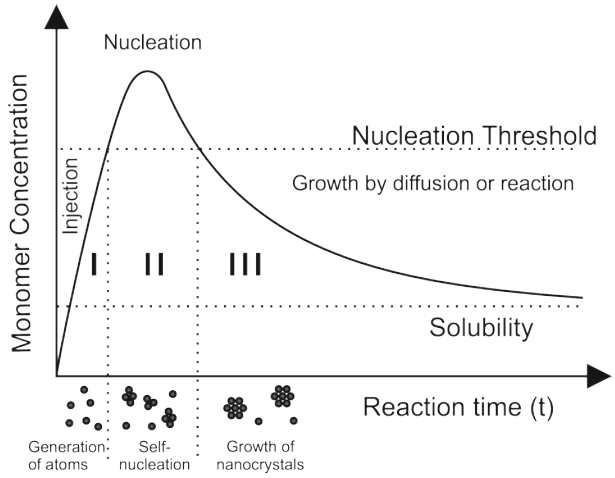

Figure 1.4. LaMer plot: the separation of nucleation and growth. The degree of saturation is plotted against reaction time.

Colloidal QDs can be synthesized from a variety of precursors in different solvents, both aqueous and organic. High boiling point organic solvents provide a wider range for the reaction temperatures and an abundant choice of precursors, and are more widely applied. The solvent can be non-coordinating (*e.g.* octadecene) acting as dispersant and controlling the diffusion of reactants. It can also be coordinating (*e.g*. oleylamine, trioctylphosphine oxide) and bind to the NC surface acting as surfactants/ligands. Ligands play an important role in the NC synthesis. In general, the ligand consists of two parts, a polar head group which binds to the NC surface (*e.g*. amines, carboxylic acids, phosphoric acids, thiols), and a hydrophobic tail, which provides the solubility in apolar solvents and also controls the diffusion speed. Both the binding strength of the polar group and the shape of the non-polar group affect the growth dynamics. Ligands also play a major role in the shape control of NCs. For instance, their difference in binding strength on different facets of the crystal may cause the weaker binding facet to grow faster. The difference in growth rates will enable the NC to grow anisotropically, yielding rods instead of spherical dots.

Synthesis of air-stable core-shell QDs is achieved by growing additional layers on pre-existing QD cores. Besides considering the electronic structure discussed in the previous section, an important crystallographic issue that needs to be considered for core-shell structures are the lattice parameters of the two materials. A general requirement for epitaxial shell growth is that the core and shell materials crystallize in the same structure and exhibit a small lattice mismatch.[19] Otherwise the strain introduced by the mismatch can cause defects states in the shell layer, which affect the optical properties and chemical stability of the NC. For example, the lattice mismatch between CdSe and ZnS is 12%, and the luminescence quantum yield has been observed to decrease when growing over two monolayers of ZnS shell, which is ascribed to strain induced by the lattice mismatch.[20, 21] Therefore, to create high quality and stable core-shell QDs for applications, both the energy offset and lattice mismatch are considered. The solution is a core/multi-shell structure, *e.g.* CdSe/CdS/(Cd,Zn)S/ZnS QDs,[21, 22] with a gradual increase of the band gap and a small lattice mismatch between adjacent layers. The core/multi shell QDs shows higher thermal quenching temperature as discussed in Chapter 4 and also demonstrate supreme stability in bio-applications as shown in Chapters 5, 6 and 7.

1.2.4 Quantum dots as FRET donor

Förster (or fluorescence) resonance energy transfer (FRET) is an energy transfer process between two chromophores. A donor in the excited state transfers its energy non-radiatively (without the appearance of a photon) to an acceptor through long-range dipole-dipole interactions.[23, 24] The rate of FRET depends on several factors, including: spectral overlap between the donor emission band and the acceptor absorption band, the relative orientation of donor and acceptor dipoles, and the distance between these two dipoles.[25] In most applications the distance is the only variable considered and the energy transfer rate k_T (r) can be given by

$$k_T(r) = \frac{1}{\tau_D}\left(\frac{R_0}{r}\right)^6 \tag{1.2}$$

where τ_D is the radiative decay time of donor, R_0 is the Förster distance or critical distance for energy transfer and r is the donor-acceptor distance. In a particular system, R_0 is a constant which can be calculate by $R_0 = 0.211(\kappa^2 n^{-4} Q_D J(\lambda))^{1/6}$ (in Å), where κ^2 is the orientation factor and is usually assumed to be 2/3 for a random distribution, and $J(\lambda)$ is the spectral overlap.[23] R_0 represents the critical distance for which the transfer rate equals the radiative decay rate. The efficiency of the energy transfer, E, is defined as the ratio of transfer rate divided by the total decay rate of the donor excited state:

$$E = \frac{k_T(r)}{k_T(r) + \tau_D^{-1}} = \frac{R_0^6}{R_0^6 + r^6} \tag{1.3}$$

and for a single donor and n acceptors:

$$E = \frac{nR_0^6}{nR_0^6 + r^6} \tag{1.4}$$

As seen from the equations above, the FRET efficiency is strongly dependent on the distance r, especially when r is close to R_0 (Figure 1.5). In applications, the change of FRET efficiency can be experimentally measured by monitoring the changes in emission spectra or changes in the lifetime of the donor emission.[26-28] Therefore the distance information can also be gained by experiment. This is also the principle on which the FRET experiments and FRET imaging are based in Chapters 5, 6, and 7.

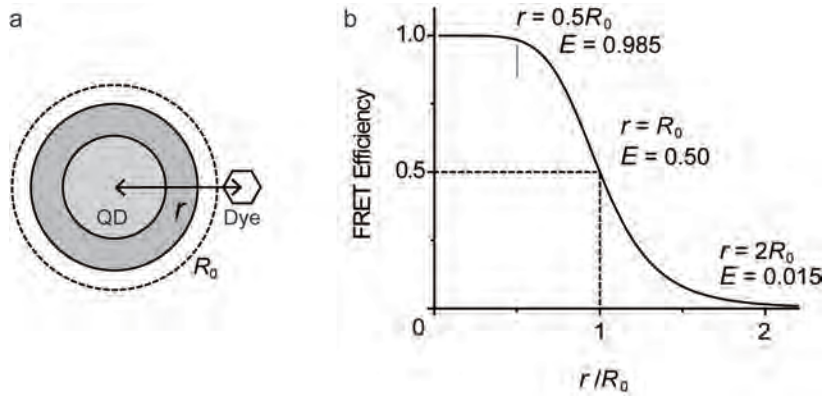

Figure 1.5. (a) The donor-acceptor distance *r* for a core-shell QD (the donor) and a surface attached dye molecule (the acceptor). (b) The efficiency of the energy transfer, *E*, depends on the distance *r*. R_0 is the Förster distance where the FRET efficiency is 0.5.

In biomedical studies, FRET is extremely useful and widely applied, since the favored FRET distance (1-10 nm) is of the same length scale as a protein or the thickness of a membrane.[23] It can be used as a spectroscopic "ruler" to determine the distance between macromolecules, or as a distance indicator to study the DNA recombination, protein folding, antibody-antigen binding and assemble-disassemble processes of nanostructures *etc*. FRET between QDs was first investigated by the Bawendi group in thin films,[29] and later Willard *et al.* showed that a QD can act as a FRET donor in biological assays.[30] Since then, many studies have appeared, mostly by using QDs as donor transferring its energy to organic dyes conjugated to surface bound macromolecules or engineered luminescent proteins.[27] Compared to organic dyes, there are many advantages to use QD as FRET donors, including a tunable emission wavelength to improve spectral overlap with a particular dye, a long fluorescent lifetime for a higher transfer efficiency, a wide excitation range and large apparent Stokes shift to minimize direct excitation of the acceptor, and the possibility for a single donor with a variable amount of acceptors for flexible tuning of the FRET efficiency. These advantages are exploited in the studies described in Chapters 5, 6, and 7.

1.3 Doped nanocrystals

1.3.1 Synthesis and properties of luminescent doped nanocrystals

Introducing impurities or dopants is a powerful method to control and introduce new functions to solid materials, including tailoring the optical, magnetic or electrical properties. The interest in doped nanocrystals started in 1994, after Bhargava *et al*.[31] published a paper claiming the observation of a six orders of magnitude faster radiative decay rate for Mn^{2+} emission in nanocrystalline ZnS compared to bulk ZnS:Mn^{2+}. Although later it was shown that the fast (ns) emission in ZnS:Mn^{2+} nanocrystal is a defect related emission, and that the lifetime of Mn^{2+} emission in NC is the same (ms) as in bulk, the interest in research on doped nanocrystals increased, in search of new physics and new applications. Two classes of doped nanocrystals can be distinguished: transition metal (TM) ion doped semiconductor nanocrystals and lanthanide (Ln) doped insulator nanocrystals.

Early research mainly focuses on doped semiconductor nanocrystals. Benefiting from the development of new colloidal synthesis methods yielding high quality semiconductor nanocrystals, similar techniques were applied to obtain doped quantum dots. Mn^{2+}, Cu^{2+} or Co^{2+} doped ZnS,[32] ZnSe,[33] CdS were the first successful examples. However, the convential synthesis methods for quantum dots did not always result in successful doping, and it was not always trivial to establish if the dopant is inside or on the surface of nanocrystals.[34, 35] Several theoretical models were applied to understand factors contributing to incorporation of dopant ions. The low content or absence of dopants in QDs, even though the dopant ion has a high solubility in the bulk semiconductor, were explained by self-purification based on thermodynamics[36] or a low surface affinity.[37] Nevertheless, new synthesis methods and more sophisticated approaches were introduced and lead to the successful and controllable doping of semiconductor nanocrystals, also for QD–dopant combinations which were previously considered to be not possible. For example, organo-metallic clusters can be used as single source precursors for doping Mn^{2+}, Co^{2+} in CdSe QDs,[38, 39] ion exchange for CdSe QDs in a solvent with Ag-precursors results in Ag^{+} doped CdSe [40] and Mn^{2+} doped ZnTe magic size nanoclusters.[41] Moreover, instead of simply decomposing the dopant and host lattice precursor together, the doping and growth can be decoupled and doping can be achieved in a step-by-step approach.[42] For example, NC cores of a host material can be synthesized first after which dopant ions are introduced by absorption on the NC surface. The subsequent growth of an additional shell of the host material will internalize the dopants. This strategy is called “growth-doping” method (also called isocrystal core/shell growth[43]) and was used for synthesis of Co^{2+}

doped CdS QDs,[43] Cu^{2+}, Mn^{2+} doped ZnSe QDs [44, 45] and Mn^{2+} doped CdS/ZnS QDs with Mn^{2+} in the ZnS shell.[46] Another strategy, called "nucleation-doping", is to synthesize a dopant core and then grow the host lattice material as a shell around the dopant core. Subsequent diffusion of dopant ions into the host material shell will lead to successful doping.[42] In Chapter 3, these different strategies are applied to synthesis Ce^{3+} and Eu^{2+} doped CaS and SrS nanocrystals.

Doping of transition metal ions in quantum dots has potential for application as luminescent labels for bio-imaging or for white light LEDs.[47] Highly efficient doped quantum dots with 60-70% quantum yield have been synthesized for Mn^{2+} doped ZnSe [47] and CdS/ZnS.[46] They can have important advantages over traditional quantum dots, such as better photo- and air-stability, reduced toxicity, and better thermal quenching behavior for the luminescence, which is important in high temperature applications.[45] Recently, electronic impurities (such as heterovalent ion substitution) doped quantum dots, CdSe:Ag^{+} have been synthesized and have the potential to create p- or n-type QD-films .[40]

The development of another category of doped nanocrystal, lanthanide-doped insulator nanocrystals, is more recent and has been triggered by the possibility to combine the high efficiency of luminescent lanthanide ions in a crystalline insulator with the benefits of nanocrystals (non-scattering, small size for bio-imaging). The luminescence properties of lanthanide ions in insulator nanocrystals include down-shifting, down-conversion, up-conversion [48], and afterglow (persistent luminescence).[49] They have potential for application in display devices, optical communication, solid-state lasers, and biological labeling.[50] So far, fluorides and orthophosphate are the most common host lattice materials for doped insulator NCs, and various wet chemical methods have been developed for the synthesis of colloidal lanthanide doped NCs.[51] Co-precipitation is a simple and convenient method first introduced by van Veggel *et al*.[52] for trivalent lanthanide doped LaF_3 NCs for down-conversion. Later this method was developed for other materials such as $NaYF_4$, $LuPO_4$, and $YbPO_4$. Co-doped with Er^{3+}, Tm^{3+} and Yb^{3+}, up-conversion NC can be achieved.[53] An alternative method is hydrothermal synthesis, which uses autoclaves to increase the solvent temperature above its ambient boiling point under a high pressure. This condition can increase the solubility of solids and speed up the reaction. Doped $NaYF_4$ NCs can be synthesized in this way. The thermal decomposition method uses a similar principle as the "hot-injection" method for semiconductor nanocrystals for producing highly monodisperse lanthanide doped NCs. It has been developed into a standard method for synthesis high quality colloidal Yb^{3+}/Er^{3+} or Yb^{3+}/Tm^{3+} doped $NaYF_4$ up conversion

NCs.[54] After surface modification and functionalization, these NC can be applied for *in vitro* and *in vivo* NIR imaging.[51]

1.3.2 Luminescence properties of lanthanides

The lanthanides are a group of metallic elements with atomic numbers from 57 to 71, also known as rare earth metals (lanthanides plus scandium and yttrium). The lanthanides are characterized by a partly filled 4*f*-shell and an electron configuration of [Xe]$4f^n6s^2$ where *n* can vary from 0 to 14. In compounds, the lanthanides easily lose their two 6*s* electrons and one 4*f* electrons resulting in the trivalent state (Ln^{3+}). A gradual decrease of the ionic radius is observed along the Ln-series from La^{3+} (102 pm) to Lu^{3+} (86 pm), which is known as the lanthanide contraction. In addition to the commonly observed trivalent state, tetravalent and divalent lanthanides can also be stable, for example Ce^{4+} or Pr^{4+} and Eu^{2+} or Yb^{2+}.

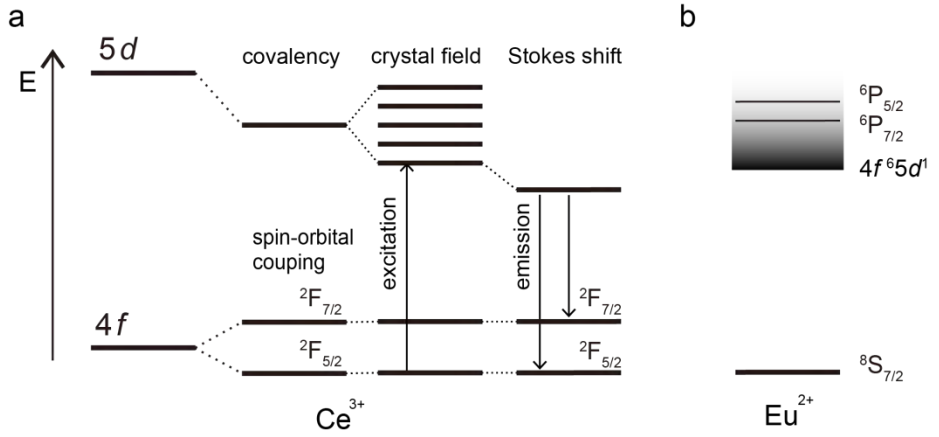

Figure 1.6. (a) The energy levels of Ce^{3+} ions in a host lattice. The energy of the *f-d* transition is influenced by nephelauxetic effect, crystal field splitting and Stokes shift. (b) The energy levels of Eu^{2+} ions. The $4f^6 5d^1$ level varies depending on the crystal field, and can be higher or lower in energy than f^7 levels.

The optical properties of trivalent lanthanide ions are characterized by their *f-f* intra-configurational transitions within the partly filled $4f^n$ shell. For *n* electrons in 14 available *f* orbitals there are 14 over *n* possible configurations and all configurations can have different energies. This gives rise to a rich energy level structure

with energy levels in the NIR, VIS and UV spectral range. Because the filled outer $5s^2$ and $5p^2$ shells shield the $4f^n$ inner shell, the electronic transitions are independent of the surrounding host materials. In the famous Dieke diagram all the energy levels in the energy range below 40,000 cm^{-1} are depicted for trivalent lanthanide ions.[55] An extension of Dieke diagram up to 70,000 cm^{-1} can be found in Ref 56.[56] The shielding also results in very weak electron-phonon coupling (small Huang-Rhys factor) and the absorption and emission spectra are characterized by sharp atomic like lines. The *f-f* transitions are forbidden by the parity selection rule. However, this rule is relaxed due to the uneven components of the crystal field and through admixture of opposite parity states the transitions become somewhat allowed as forced electric dipole transitions but the oscillator strengths are small and the *f-f* line emission is characterized by long radiative lifetimes (in milliseconds range). [57]

Some lanthanide ions also show efficient broadband emission, especially due to $4f^{n-1}5d \rightarrow 4f^n$ (*f-d*) transitions. For example, some trivalent ions (Ce^{3+}, Pr^{3+}, Tm^{3+}) and some divalent ions (Eu^{2+}, Sm^{2+}, Yb^{2+}) have been shown to yield efficient *f-d* emission. The *f-d* transitions are parity allowed and characterized by strong absorption bands and short radiative life times. In this thesis, *f-d* transitions are studied for Ce^{3+} and Eu^{2+}. Ce^{3+} ($4f^1$) has only one *f* electron. The ground state is split by spin-orbit coupling into two levels, $^2F_{5/2}$ and $^2F_{7/2}$ (see Figure 1.6a). The $5d^1$ excited state is strongly influenced by the crystal field and splits into 2 to 5 *d*-states depending on the local site symmetry [58]. The emission of Ce^{3+} originates from the lowest 5*d* state and the ground splitting of ~2000 cm^{-1} between the $^2F_{5/2}$ and $^2F_{7/2}$ levels results in the characteristic double peak emission band for Ce^{3+} with a lifetime of 20-70 ns.

Divalent Eu^{2+}($4f^7$) shows a broadband $4f^6 5d^1 \rightarrow 4f^7$ emission, with a lifetime around 1 µs. The position of emission peak is also strongly influenced by the host lattice (Figure 1.6b). If the crystal field is weak and the covalency is low, the $4f^6 5d$ level can be higher in energy than the $^6P_{7/2}$ level of the $4f^7$ configuration and sharp-line $^6P_{7/2} \rightarrow {}^8S_{7/2}$ emission is observed in the UV.[58] In host lattices where the Eu^{2+} ion occupies a site with a strong crystal field and/or high covalency, the $4f^6 5d^1 \rightarrow 4f^7$ emission can shift to the visible and even extend into the infrared spectral region.

1.4 Bio-applications of colloidal quantum dots

Fluorescence is one of the most important tools in biomedical research because it enables probing molecular and cellular process in a multiplex fashion.[23] Owing to their unique and incomparable optical properties, quantum dots have been widely applied as fluorescent labels for both live cell imaging as well as in *in vitro* diagnostics.[59] Compared to the traditional organic dyes, QDs have several distinct properties of interest to biologists and biomedical researchers, which include but are not limited to broad absorption/excitation profiles with high molar extinction coefficients, narrow and tunable (by different materials and size) emission spectra spanning from ultraviolet (UV) to the near infrared (NIR) range, large shift between excitation and emission and high resistance to photo-bleaching. [60, 61]

1.4.1 Quantum dots surface modification for biocompatibility

The majority of the synthesis pathways result in colloidal QDs that are coated with hydrophobic ligands.[60] Therefore, QDs for bio-applications require surface functionalization with hydrophilic ligands to make them suitable for an aqueous environment. To date, numerous ligands and methods have been developed for this purpose, of which three major routes are summarized below. The first method involves ligand exchange (or cap exchange) with hydrophilic ligands, replacing the native hydrophobic ligands on the surface of QDs. Each ligand is bound to the QD surface through its head group, while the tail part provides colloidal solubility, but also serves as a module for chemical conjugation of polymers or biomolecules. Typical head groups include pyridine, amines, phosphine, carboxyl groups, thiols, and phosphonic acids, in an approximate order of increasing binding strength to the QD surface.[56, 62] The binding strength is closely related to the colloidal stability of the nanoparticles. Moreover, two or multiple head groups have been observed to bind more effectively to the QDs surface and thereby provide better stability than the mono-dentate ligands.[63] The second method encompasses the encapsulation of QDs in a matrix material, which can consist of silica,[64] polymers,[65] or oils.[66] Subsequent modification of the matrix surface provides aqueous solubility.[64] The third method is the formation of self-assembled structures between hydrophobic ligand coated QDs and amphiphilic molecules, which include amphiphilic block copolymers,[65] phospholipids[67] and amphiphilic proteins.[68] In these hybrid structures the amphiphilic molecules are arranged so that the hydrophobic part faces the QD surface ligands, while the hydrophilic part is exposed to the aqueous environment and provides the aqueous solubility.

In order to apply QD hybrids in biological systems merely achieving aqueous solubility does not suffice. For nanoparticles with drug delivery or diagnostic purposes, their circulation half-life needs to be closely considered. They need to stay in the bloodstream long enough to reach the target site, but extremely long circulation half-lives may cause undesired systemic effects or can cause a poor target-to-background ratio in case of diagnostic materials. It is important to realize that *in vivo* conditions are far more complex than *in vitro* condition. The interactions between nanoparticles and plasma proteins, subsequent opsonization and removal of nanoparticles by the mononuclear phagocytic system (MPS) (previously named the reticuloendothelial system (RES)), are the major obstacles that have to be considered.[69] For example, intravenously injected QD hybrids are considered foreign by the immune system, and therefore are covered with opsonin proteins (C3, C4, C5, immunoglobulins and other blood proteins) which form a protein corona,[70] and facilitate the recognition by macrophages of the MPS, leading to their phagocytosis. This results in a rapid removal of QD hybrids from the circulation and their sequestration by MPS organs such as liver, spleen and lymph nodes.[71]

To avoid the effects described above, several methods to camouflage or mask the nanoparticles have been developed. These methods enable their reduced recognition by the MPS system and increase their circulation half-life. Most of the camouflaging methods are based on surface-modification and grafting of shielding groups that prevent protein binding and opsonization. It has been shown that hydrophilic, non-ionic surfaces can serve as a so-called stealth coating. Among many polymer materials studied, polyethylene glycol (PEG) and PEG containing copolymers are most effective and most commonly used.[69] They are highly flexible, hydrophilic, and neutral in charge, and thus can effectively prevent hydrophobic interactions, charge attractions and other interaction with blood proteins by steric repulsions.[72] PEG coated QDs with a circulation half-life over 4h have been reported.[73, 74] On the other hand, the potential toxicity of QDs may require their rapid elimination from the blood via renal excretion. This can be accomplished by the synthesis of small QDs that are coated with a thin hydrophilic layer of zwitterionic ligands,[75] or high-affinity small-molecule ligands which results in QD hybrids with an effective hydrodynamic radius of less than 5.5 nm that pass the kidney fenestrae.[76] The concern about cytotoxicity of heavy metals has generated criticisms and questions about the possibility of clinical applications of QDs. Although the safety of QDs is constantly debated and there is contradiction in results of *in vitro* and *in vivo* experiments for cytotoxicity of QDs,[77] recent experiment on small animals[78] and also on non-human primates[79] show that intravenously injected quantum dots do not exhibit evidence of toxicity for short

term. However, studies also show that the QD components, such as cadmium, remain in the liver, spleen and kidneys after 90 days, which suggests that longer-term toxicity studies about QD are still needed. [79]

1.4.2 In vivo fluorescence imaging of QDs

In vivo fluorescence imaging is similar to traditional fluorescence microscopy in principle, but acts at a macroscopic level instead. This technique allows whole-body imaging of small animals and permits the visualization of biological process in live animals in a native physiological state.[80]

To perform fluorescence imaging *in vivo*, there are some intrinsic limitations that have to be dealt with. The animal body absorbs and scatters photons, while tissues also generate auto-fluorescence under excitation light. Practically, to avoid auto-fluorescence and achieve better penetration, both excitation and emission need to be in the 700-1300 nm near infrared (NIR) range, which is known as the optical window. When also taking into account the sensitivity range of available detecting devices, two regions can be identified, as illustrated in Figure 1.7. A first NIR window lies in the 650-950 nm range and the second NIR window in the 1000-1350 nm range.[81, 82] Various synthetic organic dyes such as Cy5.5, Cy7, DiO *etc*. and QDs (Figure 1.8) such as CdTe, CdTe/CdSe, InP *etc.* are in the range of the first window.[83] Biocompatible fluorescent probes in the second window are scarce. Only until recently, several new materials, such as single wall carbon nanotubes,[82, 84] $AgSe_2$ [85] and AgS_2 [86] QDs were reported to be applicable for *in vivo* imaging in this spectra region and thus have opened up new imaging possibilities (Figure 1.8).

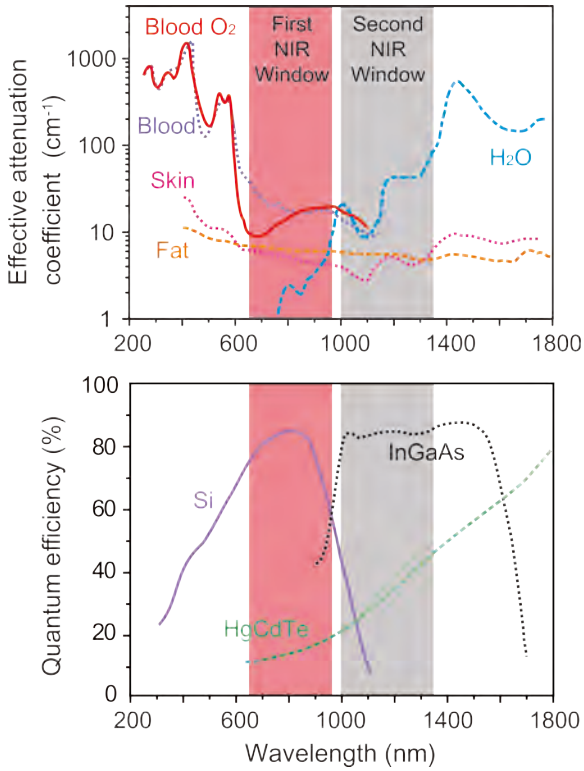

Figure 1.7. Schematic illustrations of optical windows in biological tissues. The upper graph represents the attenuation coefficient of typical elements encountered *in vivo*, including oxygenated and deoxygenated blood, water, skin and fat. The lower graph depicts the camera sensitivity with typical semiconductor detectors. The first and second NIR windows exist at the spectrum range with low tissue absorbance and high detecting sensitivity.

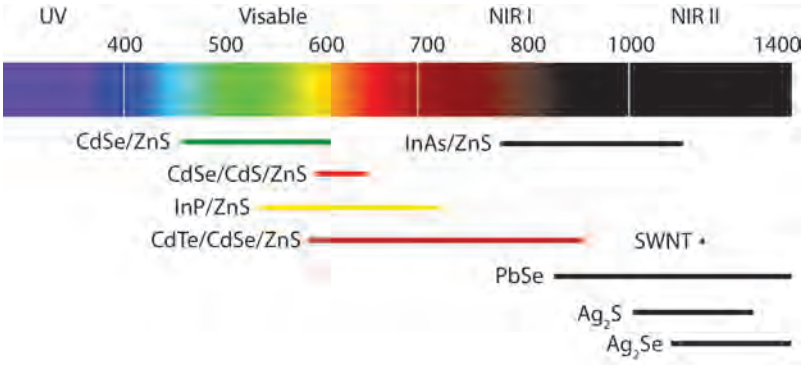

Figure 1.8. Summary of typical QDs materials that have been used for *in vivo* fluorescence imaging. Their tunable emission ranges are indicated in the spectrum.

1.4.3 Nanoparticles delivery to solid tumours

The targeted delivery of drug carriers or imaging agents to the solid tumours is realized through two major approaches: passive targeting and active targeting. Passive targeting is based on the characteristic features of the tumour vasculature which allows the extravasation and accumulation of macromolecules or nanoparticles in the tumour through the enhanced permeability and retention (EPR) effect.[87, 88] A tumor is a neoplasm, an abnormal growth of body tissue due to genetic mutation or other reasons. Fast tumour growth demands nutritional and oxygen supply, which is realized by stimulating the production of blood vessels through angiogenesis. Unlike the blood vessels in normal tissues, the tumour vasculature is highly irregular, heterogeneous in their spatial distribution, dilated and tortuous.[89] The endothelium, a cell monolayer that seperates the vessel lumen and wall, of tumour neovasculature has wide interendothelial junctions, rich of fenestrae and transendothelial channels formed by vesicles.[90] The direct results are irregular blood flow, increased permeability, and a leaky vessel wall, which permits the extravasation of nanoparticles up to hundreds of nanometers in size.[91] Moreover, the fast-growing tumour cells compress the lymphatic vessels and cause them to collapse, especially at the center of the tumour. This causes lymphatic drainage at the periphery of tumour. Combined, the leaky vessel wall and poor lymphatic drainage cause abnormal molecular and fluid transport dynamics, and subsequently lead to the extravasation and accumulation of long circulating nanoparticles in tumours. To date, there are realm of nanoparticle platforms that have been designed to exploit the EPR effect for cancer diagnostic and therapy.[92] Some of these nano-carrier base drugs are already approved by the FDA for clinical use and available on the market.[88]

However, passive targeting of nanoparticles by exploiting the EPR effect suffers from several limitations, and the random nature of the process also makes it less controllable. A potential way to improve the specificity is by attaching targeting ligands to the nanoparticles' surface, which enables them to actively bind to specific tumor cell surface receptors after extravasation. This approach is commonly referred to as active targeting. A prerequisite is that the targeting ligands display high selective binding to the tumour cell and that the target on the cancer cells is overexpressed.[92] An example of this targeting agent is a peptide, arginine-glycine-aspartic acid (RGD), which binds to the integrin $\alpha_v\beta_3$, which is expressed on a variety of cancer cells as well as on the endothelium cells of the tumor vasculature.[93] Interestingly, the specific binding can also enhance nanoparticle uptake by cells through receptor-mediated internalization.

1.4.4 Atherosclerosis targeting and lipoproteins

Atherosclerosis is a chronic inflammatory disease that causes thickening and hardening of the artery well, due to accumulation of fatty materials such as lipoproteins and cholesterol, which initiate the formation of atherosclerotic plaques. Rupture of atherosclerotic plaques is the primary cause of heart disease and stroke, which account for about 50% of all deaths in the Western World[94]. The development of atherosclerosis is a complex process and strongly dependent on lipoprotein metabolism.[95] For instance, it starts with dysfunction of endothelial cells under external stimulations and subsequent accumulation of oxidized low density lipoproteins (LDL) in the subendothelial matrix. LDL is a plasma protein that carries cholesterol and triglycerides, and the raise of circulation levels contributes to plaque formation[94] and therefore generally known as “bad cholesterol”. These trapped LDLs undergo a series of modification that cause an inflammatory response that initiates the recruitment of monocytes, which convert into macrophages. Eventually, macrophages that have engulfed oxidized LDLs become foam cells that contribute to the progression of atherosclerotic plaques. As a reverse process of the formation of foam cells, lipoprotein apo-A1produced in liver forming high-density lipoprotein (HDL) during circulation, and the HDL triggers the cholesterol efflux from the macrophages. Hence, HDL has a pivotal protective function against atherosclerosis, as it facilitates the removal of cholesterol from the peripheral tissue and its subsequent transportation to the liver for excretion or re-utilization. Therefore, HDL is often called “good cholesterol”.

Understanding the molecular and cellular process of atherosclerosis creates numerous opportunities for targeting the plaques using nanoparticles.[95, 96] Since the aforementioned HDL and LDL interact with plaques, a mimicking of these lipoproteins by reconstructed nanocrystal assemblies or labeled nature particles have shown efficient targeting to the plaques.[97-99] In advanced atherosclerotic lesions a variety of other targets become relevant, including neovascularization, fibrin by anticoagulant nanoparticles *etc*.[96]

1.5 Outline of this thesis

This thesis presents research starting from the chemical synthesis of (lanthanide doped) nanocrystals, continuing with the characterization and physical properties of semiconductor QDs and finally realizing their biomedical applications. The aim of the research is to provide a better understanding of the synthesis and optical properties of quantum dots and to use the control over the physical and chemical properties for application in biomedical imaging.

The first part of the thesis focuses on the chemical synthesis of lanthanide doped nanocrystals. Chapter 2 first presents the synthesis of colloidal CaS and SrS NCs via single source precursors. Through thermal decomposition of a metal-dithiocarbamate complex in oleylamine, small ~10 nm CaS and SrS NCs with a narrow size distribution can be made. Based on this work, in Chapter 3 the single source precursor method is further developed for the synthesis of Ce^{3+} or Eu^{2+} doped CaS and SrS NCs. Successful doping was achieved and shown to critically depend on reaction conditions. Formation of doped NCs is favored for comparable decomposition temperatures of dopant and lattice precursors. In combination with the application of more sophisticated doping strategies, including growth doping and nucleation doping, the potential of the single precursor method is demonstrated for the synthesis of new types of doped luminescent nanocrystals.

The second part of the thesis focuses on the optical properties of QDs. In Chapter 4, the thermal quenching behavior of various types of core-shell QDs were investigated in a high-temperature range (300-500 K). Thermal cycling (yoyo) experiments for QDs immobilized in a polymer matrix reveals both reversible and irreversible luminescence quenching processes. The reversible quenching is explained by the thermally activated creation or population of defect states.

The last part of the thesis concerns the application of QD for bio-imaging purpose. Chapter 5 discusses the dynamics of lipid exchange for lipid coated QDs. To investigate the dynamics QD micelles coated with PEG-lipids and with Cy5.5 labeled lipids are used and the lipid exchange dynamics are monitored by measuring fluorescence resonant energy transfer (FRET) between the QD core and dye-lipids attached to the surface. Modeling of the temperature dependent lipid exchange dynamics yields important information on the stability of QD-lipid micelles and the knowledge will be beneficial for biomedical imaging and pharmaceutical studies relying on lipid micelles.

The QD FRET system developed in Chapter 5 is applied to bio-imaging studies which comprise the last part of the thesis. In Chapter 6, a lipoprotein-based nanoparticle that consists of a QD core and a Cy5.5 labeled lipidic coating allows the study of lipoprotein-lipoprotein interactions, lipid exchange dynamics, and the influence of apolipoproteins on these processes. Moreover, the QD FRET system was used to study *in vitro* the HDL-cell interactions and exploit FRET to visualize HDL association with macrophage cells. In Chapter 7, the application of the FRET system was extended to *in vivo* experiments. The distribution, dissociation and fate of different components of the QD - dye lipid micelles was followed in time for our dual labeled nanoparticle by tuning its optical features (both QD emission and dye emission) to the near-infrared where the penetration depth is high. Through using advanced *in vivo* fluorescence imaging techniques, it is shown how the quantum dot core hybrid nanoparticles, after intravenous administration, encounter rapid lipid exchange processes with blood proteins during circulation in the blood stream. Accumulation and further dissociation occurs in tumours. The results show how self-assembled nanoparticles can quickly transform *in vivo* after injection, which affects their functionality. The study reveals that caution is required in the interpretation of imaging data when using lipid-coated nanocrystals as diagnostic agents.

References

1. Alivisatos, P.; Roco, M. C.; Williams, R. S. *NSF Report, XXV*; 2001.
2. Royal Society; Royal Academy of Engineering, *Nanoscience and Nanotechnologies: Opportunities and Uncertainties*. Royal Society: **2004**.
3. Peng, X., An essay on synthetic chemistry of colloidal nanocrystals. *Nano Research* **2009**, 2, 425-447.
4. Leutwyler, W. K.; Bürgi, S. L.; Burgl, H., Semiconductor clusters, nanocrystals, and quantum dots. *Science* **1996**, 271, 933.
5. Roduner, E., Size matters: why nanomaterials are different. *Chem. Soc. Rev.* **2006**, 35, 583-592.
6. Zhou, Z.-Y.; Tian, N.; Li, J.-T.; Broadwell, I.; Sun, S.-G., Nanomaterials of high surface energy with exceptional properties in catalysis and energy storage. *Chem. Soc. Rev.* **2011**, 40, 4167-4185.
7. Alivisatos, P., The use of nanocrystals in biological detection. *Nat. Biotechnol.* **2004**, 22, 47-52.
8. Porter, A. L.; Youtie, J., How interdisciplinary is nanotechnology? *J Nanopart Res* **2009**, 11, 1023-1041.
9. Gaponenko, S. V., *Optical Properties of Semiconductor Nanocrystals*. Cambridge University Press: **2005**.
10. Ithurria, S.; Tessier, M. D.; Mahler, B.; Lobo, R. P.; Dubertret, B.; Efros, A. L., Colloidal nanoplatelets with two-dimensional electronic structure. *Nat. Mater.* **2011**, 10, 936-41.
11. Talapin, D. V.; Shevchenko, E. V.; Murray, C. B.; Kornowski, A.; Förster, S.; Weller, H., CdSe and CdSe/CdS Nanorod Solids. *J. Am. Chem. Soc.* **2004**, 126, 12984-12988.
12. Groeneveld, E.*, et al.*, Highly Luminescent (Zn,Cd)Te/CdSe Colloidal Heteronanowires with Tunable Electron–Hole Overlap. *Nano Lett.* **2012**, 12, 749-757.
13. Donega, C. d. M., Synthesis and properties of colloidal heteronanocrystals. *Chem. Soc. Rev.* **2011**, 40, 1512-1546.
14. Hines, M. A.; Guyot-Sionnest, P., Synthesis and characterization of strongly luminescing ZnS-Capped CdSe nanocrystals. *J. Phys. Chem.* **1996**, 100, 468-471.
15. Krumer, Z.*, et al.*, Tackling self-absorption in luminescent solar concentrators with type-II colloidal quantum dots. *Sol. Energy Mater. Sol. Cells* **2013**, 111, 57-65.
16. LaMer, V. K.; Dinegar, R. H., Theory, Production and Mechanism of Formation of Monodispersed Hydrosols. *J. Am. Chem. Soc.* **1950**, 72, 4847-4854.
17. de Mello Donega, C.; Liljeroth, P.; Vanmaekelbergh, D., Physicochemical evaluation of the hot-injection method, a synthesis route for monodisperse nanocrystals. *Small* **2005**, 1, 1152-62.
18. Park, J.*, et al.*, Ultra-large-scale syntheses of monodisperse nanocrystals. *Nat. Mater.* **2004**, 3, 891-5.
19. Rogach, A. L., *Semiconductor Nanocrystal Quantum Dots*. Springer-Verlag/Wien: **2008**.
20. Dabbousi, B. O.*, et al.*, (CdSe)ZnS Core−Shell Quantum Dots: Synthesis and Characterization of a Size Series of Highly Luminescent Nanocrystallites. *The Journal of Physical Chemistry B* **1997**, 101, 9463-9475.
21. Xie, R.; Kolb, U.; Li, J.; Basche, T.; Mews, A., Synthesis and Characterization of Highly Luminescent CdSe - Core CdS/Zn0.5Cd0.5S/ZnS Multishell Nanocrystals. *J. Am. Chem. Soc.* **2005**, 127, 7480-7488.

22. Lim, J.; Jun, S.; Jang, E.; Baik, H.; Kim, H.; Cho, J., Preparation of highly luminescent nanocrystals and their application to light-emitting diodes. *Adv. Mater.* **2007**, 19, 1927-+.
23. Lakowicz, J. R., *Principles of Fluorescence Spectroscopy*. Springer London, Limited: **2009**.
24. Clapp, A. R.; Medintz, I. L.; Mattoussi, H., Forster resonance energy transfer investigations using quantum-dot fluorophores. *ChemPhysChem* **2006**, 7, 47-57.
25. Jares-Erijman, E. A.; Jovin, T. M., FRET imaging. *Nat. Biotechnol.* **2003**, 21, 1387-95.
26. Clapp, A. R.; Medintz, I. L.; Mauro, J. M.; Fisher, B. R.; Bawendi, M. G.; Mattoussi, H., Fluorescence Resonance Energy Transfer Between Quantum Dot Donors and Dye-Labeled Protein Acceptors. *J. Am. Chem. Soc.* **2004**, 126, 301-310.
27. Medintz, I. L.; Clapp, A. R.; Mattoussi, H.; Goldman, E. R.; Fisher, B.; Mauro, J. M., Self-assembled nanoscale biosensors based on quantum dot FRET donors. *Nat. Mater.* **2003**, 2, 630-638.
28. Mattoussi, H.; Mauro, J. M.; Goldman, E. R.; Anderson, G. P.; Sundar, V. C.; Mikulec, F. V.; Bawendi, M. G., Self-Assembly of CdSe-ZnS Quantum Dot Bioconjugates Using an Engineered Recombinant Protein. *J. Am. Chem. Soc.* **2000**, 122, 12142-12150.
29. Kagan, C. R.; Murray, C. B.; Nirmal, M.; Bawendi, M. G., Electronic Energy Transfer in CdSe Quantum Dot Solids. *Phys. Rev. Lett.* **1996**, 76, 1517-1520.
30. Willard, D. M.; Carillo, L. L.; Jung, J.; Van Orden, A., CdSe−ZnS Quantum Dots as Resonance Energy Transfer Donors in a Model Protein−Protein Binding Assay. *Nano Lett.* **2001**, 1, 469-474.
31. Bhargava, R. N.; Gallagher, D.; Hong, X.; Nurmikko, A., Optical properties of manganese-doped nanocrystals of ZnS. *Phys. Rev. Lett.* **1994**, 72, 416-419.
32. Suyver, J. F.; Wuister, S. F.; Kelly, J. J.; Meijerink, A., Luminescence of nanocrystalline ZnSe:Mn2+. *Phys. Chem. Chem. Phys.* **2000**, 2, 5445-5448.
33. Norris, D. J.; Yao, N.; Charnock, F. T.; Kennedy, T. A., High-Quality Manganese-Doped ZnSe Nanocrystals. *Nano Lett.* **2000**, 1, 3-7.
34. Norris, D. J.; Efros, A. L.; Erwin, S. C., Doped nanocrystals. *Science* **2008**, 319, 1776-9.
35. Bol, A. A.; van Beek, R.; Meijerink, A., On the Incorporation of Trivalent Rare Earth Ions in II−VI Semiconductor Nanocrystals. *Chem. Mater.* **2002**, 14, 1121-1126.
36. Dalpian, G. M.; Chelikowsky, J. R., Self-Purification in Semiconductor Nanocrystals. *Phys. Rev. Lett.* **2006**, 96, 226802.
37. Erwin, S. C.; Zu, L.; Haftel, M. I.; Efros, A. L.; Kennedy, T. A.; Norris, D. J., Doping semiconductor nanocrystals. *Nature* **2005**, 436, 91-4.
38. Hanif, K. M.; Meulenberg, R. W.; Strouse, G. F., Magnetic Ordering in Doped Cd1-xCoxSe Diluted Magnetic Quantum Dots. *J. Am. Chem. Soc.* **2002**, 124, 11495-11502.
39. Archer, P. I.; Santangelo, S. A.; Gamelin, D. R., Direct Observation of sp−d Exchange Interactions in Colloidal Mn2+- and Co2+-Doped CdSe Quantum Dots. *Nano Lett.* **2007**, 7, 1037-1043.
40. Sahu, A.*, et al.*, Electronic Impurity Doping in CdSe Nanocrystals. *Nano Lett.* **2012**, 12, 2587-2594.
41. Eilers, J.; Groeneveld, E.; de Mello Donegá, C.; Meijerink, A., Optical Properties of Mn-Doped ZnTe Magic Size Nanocrystals. *The Journal of Physical Chemistry Letters* **2012**, 3, 1663-1667.

42. Pradhan, N.; Goorskey, D.; Thessing, J.; Peng, X., An Alternative of CdSe Nanocrystal Emitters: Pure and Tunable Impurity Emissions in ZnSe Nanocrystals. *J. Am. Chem. Soc.* **2005**, 127, 17586-17587.
43. Radovanovic, P. V.; Gamelin, D. R., Electronic absorption spectroscopy of cobalt ions in diluted magnetic semiconductor quantum dots: demonstration of an isocrystalline core/shell synthetic method. *J. Am. Chem. Soc.* **2001**, 123, 12207-14.
44. Chen, D.; Viswanatha, R.; Ong, G. L.; Xie, R.; Balasubramaninan, M.; Peng, X., Temperature Dependence of lementary Processes in Doping Semiconductor Nanocrystals. *J. Am. Chem. Soc.* **2009**, 131, 9333-9339.
45. Pradhan, N.; Peng, X., Efficient and Color-Tunable Mn-Doped ZnSe Nanocrystal Emitters: Control of Optical Performance via Greener Synthetic Chemistry. *J. Am. Chem. Soc.* **2007**, 129, 3339-3347.
46. Yang, Y.; Chen, O.; Angerhofer, A.; Cao, Y. C., On doping CdS/ZnS core/shell nanocrystals with Mn. *J. Am. Chem. Soc.* **2008**, 130, 15649-61.
47. Pradhan, N.; Battaglia, D. M.; Liu, Y.; Peng, X., Efficient, Stable, Small, and Water-Soluble Doped ZnSe Nanocrystal Emitters as Non-Cadmium Biomedical Labels. *Nano Lett.* **2006**, 7, 312-317.
48. Wang, F.*, et al.*, Simultaneous phase and size control of upconversion nanocrystals through lanthanide doping. *Nature* **2010**, 463, 1061-5.
49. le Masne de Chermont, Q.*, et al.*, Nanoprobes with near-infrared persistent luminescence for *in vivo* imaging. *Proc. Natl. Acad. Sci. U. S. A.* **2007**, 104, 9266-71.
50. Wang, G.; Peng, Q.; Li, Y., Lanthanide-doped nanocrystals: synthesis, optical-magnetic properties, and applications. *Acc. Chem. Res.* **2011**, 44, 322-32.
51. Wang, F.; Liu, X., Recent advances in the chemistry of lanthanide-doped upconversion nanocrystals. *Chem. Soc. Rev.* **2009**, 38, 976-89.
52. Stouwdam, J. W.; van Veggel, F. C. J. M., Near-infrared Emission of Redispersible Er3+, Nd3+, and Ho3+ Doped LaF3 Nanoparticles. *Nano Lett.* **2002**, 2, 733-737.
53. Yi, G.-S.; Chow, G.-M., Colloidal LaF3:Yb,Er, LaF3:Yb,Ho and LaF3:Yb,Tm nanocrystals with multicolor upconversion fluorescence. *J. Mater. Chem.* **2005**, 15, 4460-4464.
54. Mai, H.-X.; Zhang, Y.-W.; Si, R.; Yan, Z.-G.; Sun, L.-d.; You, L.-P.; Yan, C.-H., High-Quality Sodium Rare-Earth Fluoride Nanocrystals: Controlled Synthesis and Optical Properties. *J. Am. Chem. Soc.* **2006**, 128, 6426-6436.
55. Dieke, G. H., *Spectra and Energy Levels of Rare Earth Ions in Crystals*. Wiley Interscience, New York: **1968**.
56. Wegh, R. T.; Meijerink, A.; Lamminmäki, R.-J.; Jorma, H., Extending Dieke's diagram. *J. Lumin.* **2000**, 87–89, 1002-1004.
57. Blasse, G., Vibronic transitions in rare earth spectroscopy. *Int. Rev. Phys. Chem.* **1992**, 11, 71-100.
58. Blasse, G.; Grabmaier, B. C., *Luminescent Materials*. Springer-Verlag: **1994**.
59. Klostranec, J. M.; Chan, W. C. W., Quantum Dots in Biological and Biomedical Research: Recent Progress and Present Challenges. *Adv. Mater.* **2006**, 18, 1953-1964.
60. Medintz, I. L.; Uyeda, H. T.; Goldman, E. R.; Mattoussi, H., Quantum dot bioconjugates for imaging, labelling and sensing. *Nat. Mater.* **2005**, 4, 435-46.
61. Michalet, X.*, et al.*, Quantum Dots for Live Cells, *in Vivo* Imaging, and Diagnostics. *Science* **2005**, 307, 538-544.
62. Schapotschnikow, P.; Hommersom, B.; Vlugt, T. J. H., Adsorption and Binding of Ligands to CdSe Nanocrystals. *The Journal of Physical Chemistry C* **2009**, 113, 12690-12698.

63. Uyeda, H. T.; Medintz, I. L.; Jaiswal, J. K.; Simon, S. M.; Mattoussi, H., Synthesis of compact multidentate ligands to prepare stable hydrophilic quantum dot fluorophores. *J. Am. Chem. Soc.* **2005**, 127, 3870-8.
64. Koole, R.*, et al.*, On the Incorporation Mechanism of Hydrophobic Quantum Dots in Silica Spheres by a Reverse Microemulsion Method. *Chem. Mater.* **2008**, 20, 2503-2512.
65. Gao, X.; Cui, Y.; Levenson, R. M.; Chung, L. W.; Nie, S., *In vivo* cancer targeting and imaging with semiconductor quantum dots. *Nat. Biotechnol.* **2004**, 22, 969-76.
66. Jarzyna, P. A.*, et al.*, Iron oxide core oil-in-water emulsions as a multifunctional nanoparticle platform for tumor targeting and imaging. *Biomaterials* **2009**, 30, 6947-54.
67. Dubertret, B.; Skourides, P.; Norris, D. J.; Noireaux, V.; Brivanlou, A. H.; Libchaber, A., *In Vivo* Imaging of Quantum Dots Encapsulated in Phospholipid Micelles. *Science* **2002**, 298, 1759-1762.
68. Skajaa, T.*, et al.*, Quantum Dot and Cy5.5 Labeled Nanoparticles to Investigate Lipoprotein Biointeractions via Forster Resonance Energy Transfer. *Nano Lett.* **2010**, 10, 5131–5138.
69. Owens, D. E., 3rd; Peppas, N. A., Opsonization, biodistribution, and pharmacokinetics of polymeric nanoparticles. *Int. J. Pharm.* **2006**, 307, 93-102.
70. Nel, A. E.*, et al.*, Understanding biophysicochemical interactions at the nano-bio interface. *Nat. Mater.* **2009**, 8, 543-57.
71. Aggarwal, P.; Hall, J. B.; McLeland, C. B.; Dobrovolskaia, M. A.; McNeil, S. E., Nanoparticle interaction with plasma proteins as it relates to particle biodistribution, biocompatibility and therapeutic efficacy. *Adv Drug Deliv Rev* **2009**, 61, 428-37.
72. Jeon, S. I.; Lee, J. H.; Andrade, J. D.; De Gennes, P. G., Protein—surface interactions in the presence of polyethylene oxide: I. Simplified theory. *J. Colloid Interface Sci.* **1991**, 142, 149-158.
73. Choi, H. S.; Ipe, B. I.; Misra, P.; Lee, J. H.; Bawendi, M. G.; Frangioni, J. V., Tissue- and organ-selective biodistribution of NIR fluorescent quantum dots. *Nano Lett.* **2009**, 9, 2354-9.
74. Schipper, M. L.*, et al.*, Particle Size, Surface Coating, and PEGylation Influence the Biodistribution of Quantum Dots in Living Mice. *Small* **2009**, 5, 126-134.
75. Choi, H. S.*, et al.*, Renal clearance of quantum dots. *Nat. Biotechnol.* **2007**, 25, 1165-70.
76. Choi, H. S.; Liu, W.; Liu, F.; Nasr, K.; Misra, P.; Bawendi, M. G.; Frangioni, J. V., Design considerations for tumour-targeted nanoparticles. *Nat. Nanotechnol.* **2010**, 5, 42-7.
77. Fischer, H. C.; Liu, L.; Pang, K. S.; Chan, W. C. W., Pharmacokinetics of Nanoscale Quantum Dots: In Vivo Distribution, Sequestration, and Clearance in the Rat. *Adv. Funct. Mater.* **2006**, 16, 1299-1305.
78. Hauck, T. S.; Anderson, R. E.; Fischer, H. C.; Newbigging, S.; Chan, W. C. W., *In vivo* Quantum-Dot Toxicity Assessment. *Small* **2010**, 6, 138-144.
79. Ye, L.*, et al.*, A pilot study in non-human primates shows no adverse response to intravenous injection of quantum dots. *Nat. Nanotechnol.* **2012**, 7, 453-8.
80. Rao, J.; Dragulescu-Andrasi, A.; Yao, H., Fluorescence imaging *in vivo*: recent advances. *Curr. Opin. Biotechnol.* **2007**, 18, 17-25.
81. Smith, A. M.; Mancini, M. C.; Nie, S., Bioimaging: second window for *in vivo* imaging. *Nat. Nanotechnol.* **2009**, 4, 710-1.

82. Welsher, K.; Liu, Z.; Sherlock, S. P.; Robinson, J. T.; Chen, Z.; Daranciang, D.; Dai, H., A route to brightly fluorescent carbon nanotubes for near-infrared imaging in mice. *Nat. Nanotechnol.* **2009**, 4, 773-80.
83. Aswathy, R. G.; Yoshida, Y.; Maekawa, T.; Kumar, D. S., Near-infrared quantum dots for deep tissue imaging. *Anal. Bioanal. Chem.* **2010**, 397, 1417-35.
84. Robinson, J. T.; Hong, G.; Liang, Y.; Zhang, B.; Yaghi, O. K.; Dai, H., *In vivo* fluorescence imaging in the second near-infrared window with long circulating carbon nanotubes capable of ultrahigh tumor uptake. *J. Am. Chem. Soc.* **2012**, 134, 10664-9.
85. Zhu, C.-N.; Jiang, P.; Zhang, Z.-L.; Zhu, D.-L.; Tian, Z.-Q.; Pang, D.-W., Ag2Se Quantum Dots with Tunable Emission in the Second Near-Infrared Window. *ACS Appl. Mater. Interfaces* **2013**.
86. Hong, G.; Robinson, J. T.; Zhang, Y.; Diao, S.; Antaris, A. L.; Wang, Q.; Dai, H., *In vivo* fluorescence imaging with Ag2S quantum dots in the second near-infrared region. *Angew. Chem. Int. Ed. Engl.* **2012**, 51, 9818-21.
87. Matsumura, Y.; Maeda, H., A new concept for macromolecular therapeutics in cancer chemotherapy: mechanism of tumoritropic accumulation of proteins and the antitumor agent smancs. *Cancer Res.* **1986**, 46, 6387-92.
88. Peer, D.; Karp, J. M.; Hong, S.; Farokhzad, O. C.; Margalit, R.; Langer, R., Nanocarriers as an emerging platform for cancer therapy. *Nat Nano* **2007**, 2, 751-760.
89. Jain, R. K.; Stylianopoulos, T., Delivering nanomedicine to solid tumors. *Nat. Rev. Clin. Oncol.* **2010**, 7, 653-64.
90. Roberts, W. G.; Palade, G. E., Neovasculature Induced by Vascular Endothelial Growth Factor Is Fenestrated. *Cancer Res.* **1997**, 57, 765-772.
91. Hobbs, S. K.; Monsky, W. L.; Yuan, F.; Roberts, W. G.; Griffith, L.; Torchilin, V. P.; Jain, R. K., Regulation of transport pathways in tumor vessels: role of tumor type and microenvironment. *Proc. Natl. Acad. Sci. U. S. A.* **1998**, 95, 4607-12.
92. Davis, M. E.; Chen, Z. G.; Shin, D. M., Nanoparticle therapeutics: an emerging treatment modality for cancer. *Nat. Rev. Drug Discov.* **2008**, 7, 771-82.
93. Hak, S.*, et al.*, The Effect of Nanoparticle Polyethylene Glycol Surface Density on Ligand-Directed Tumor Targeting Studied *in Vivo* by Dual Modality Imaging. *ACS Nano* **2012**, 6, 5648-5658.
94. Lusis, A. J., Atherosclerosis. *Nature* **2000**, 407, 233-41.
95. Lobatto, M. E.; Fuster, V.; Fayad, Z. A.; Mulder, W. J., Perspectives and opportunities for nanomedicine in the management of atherosclerosis. *Nat. Rev. Drug Discov.* **2011**, 10, 835-52.
96. Sanz, J.; Fayad, Z. A., Imaging of atherosclerotic cardiovascular disease. *Nature* **2008**, 451, 953-7.
97. Cormode, D. P.*, et al.*, Nanocrystal core high-density lipoproteins: a multimodality contrast agent platform. *Nano Lett.* **2008**, 8, 3715-23.
98. Cormode, D. P.*, et al.*, Comparison of synthetic high density lipoprotein (HDL) contrast agents for MR imaging of atherosclerosis. *Bioconjug. Chem.* **2009**, 20, 937-43.
99. Cormode, D. P.*, et al.*, Atherosclerotic plaque composition: analysis with multicolor CT and targeted gold nanoparticles. *Radiology* **2010**, 256, 774-82.

CHAPTER 2

Single-source Precursor Synthesis of Colloidal CaS and SrS Nanocrystals

Abstract

Colloidal CaS and SrS nanocrystals were prepared by thermal decomposition of calcium and strontiumdiisopropyldithiocarbamate complexes in oleylamine. The diameter of the nanocrystals was 8-10 nm with a narrow size distribution, showing that this single source precursor method gives access to monodisperse nanocrystals of small size.

2.1 Introduction

Semiconductor nanocrystals, also known as quantum dots, increasingly find application as materials for optoelectronics, photonics, spintronics, catalysis and biomedical applications. Because of these applications and their unique size-dependent properties, many research groups have pursued the synthesis and characterization of nanoparticles with various compositions, sizes, shapes and properties.[1-3] Nanocrystals of II^B-VI, III-V and IV-VI semiconductors in particular have been subject of extensive investigation, whereas other groups of semiconductors have received much less attention. One of these is the class of alkaline earth-chalcogenide II^A-VI semiconductors, of which CaS and SrS are members. In the bulk state these wide band gap semiconductors are versatile and excellent phosphor host materials,[4] which find application in luminescent devices [5, 6] and in optical data storage. [7] While the synthesis protocols for colloidal nanocrystals of II^B-VI semiconductors have reached a very mature level, allowing monodisperse ensembles of nanocrystals with well-defined size and shape to be routinely prepared,[1-3] there are no methods to prepare high-quality nanocrystals of II^A-VI compounds. The few synthetic methodologies currently available yield only large particles of dimensions in the tens to hundreds nanometers, with undefined shapes and large size distributions.[6-8]

The development of a reproducible synthesis method for well-defined and monodisperse II^A-VI nanocrystals is important in the design of Cd-free biolabels. At present, the application of luminescent quantum dots for *in vivo* imaging and treatments is hampered by the presence of harmful heavy metals. Doped bulk CaS, which is non-toxic, is well-known for efficient persistent luminescence[9] so that the synthesis of doped CaS nanocrystals is expected to lead to the development of biocompatible afterglow nanolabels. This is of great interest for *in vivo* imaging applications, as it offers the prospect of background free imaging by circumventing tissue autofluorescence.[10] In addition, doped CaS nanocrystals may be applied as spectral converters in luminescent solar concentrators. All these applications require a reproducible synthesis route of well-defined colloidal CaS nanocrystals. Preferably the produced nanocrystals are small (< 10 nm) since this suppresses light scattering and increases the stability of the nanoparticles in colloidal suspensions, which is beneficial for biomedical and optical applications.

Here we report a synthesis route of small colloidal CaS nanocrystals, which is based on hot injection of a single-source precursor. While the benefits of the hot injection approach, i.e. controlled nanoparticle growth and formation of a high

quality product, have been well documented, [1, 2, 11] single-source precursors have the additional advantage that the metal-chalcogenide bond is already present. This generally results in materials with fewer defects, better stoichiometry and narrow size distributions ,[12] and allows the synthesis of large quantities of materials from relatively harmless and easy to handle reagents. Calcium diisopropyl - dithiocarbamate, $Ca(DPTC)_2$, is used here as single-source precursor (see reaction 1). Calcium dithiocarbamates belong to the few molecular compounds in which calcium-sulphur coordination occurs,[13] and therefore are one of the few candidates to be utilized as single-source precursor of CaS nanocrystals. Dialkyldithiocarbamate complexes of other metals, in presence of coordinating surfactants, have already been utilized in the synthesis of sulfide containing nanocrystals, e.g. of CdS,[14]ZnS,[15] and EuS.[16, 17] As described below, the method is also applicable to the synthesis of SrS nanoparticles. SrS is chemically similar to CaS, and the same uses and applications for nanocrystals of this material are foreseen.

2.2 Materials and methods

Precursor synthesis

Calciumdiisopropyldithiocarbamate, $Ca(DPTC)_2$, was prepared as described by Purdy and George[18]. Essentially the same method was used for the synthesis of strontium diisopropyldithiocarbamate$Sr(DPTC)_2$. Deionized water (200 ml) in a 500 mL two-necked flask was degassed by repeated evacuation and refilling with nitrogen. Subsequently, 25 mL (0.18 mol) diisopropylamine and 3.0 mL (50 mmol) carbon disulfide were added. The biphasic mixture was stirred for 1 hour under N_2 atmosphere and turned gradually into a yellow homogenous solution. Metallic strontium (2.2 g, 25.1 mmol) was introduced in small portions, and the solution was stirred for 3 days under N_2. Subsequently, the slightly turbid yellow mixture was filtered. Water was evaporated from the filtrate in a rotary evaporator. The resulting solid was twice dissolved in 50 ml ethanol and evaporated to dryness, and dried further in a vacuum desiccator over P_2O_5 overnight. The solid was dissolved in 50 mL THF and the solution was filtered to remove insoluble parts. The filtrate was concentrated by rotary evaporation to give 9.0 g (20.4 mmol, 82 %) of an off-white solid. IR (ATR): 2968 (m), 2924 (m), 1477(m), 1439 (m), 1366 (m), 1309 (s), 1199 (m-s), 1150 (m), 1038 (m-s), 948 (w), 847 (w), 787(w). ^{1}H NMR (DMSO-d_6): 6.24 (b), 4.25 (sept), 3.71 (b), 1.59 (b), 1.31 (d), 1.04 (b); in common with its Caanalog,[13] the spectrum reflects the involvement of the compound in a tempera-

ture dependent equiliåbrium by showing broad coalescence peaks of chemically different isopropyl groups.^{13}C NMR: (DMSO-d_6): 211.6 (C-S), 53.6 (C-H), 48.3(C-H), 21.0 (CH_3), 19.8 (CH_3), all broad.

Nanocrystal synthesis

A 100 mM solution of the appropriate precursor (see Supplementary Material) in oleylamine was freshly made. In a glovebox, 3 mL of this solution was injected into 6 mL oleylamine kept at 250°C, upon which the temperature dropped to 210-225 °C. The temperature was raised again to 250 °C, and subsequently aliquots of 1-2 mL were brought into either hexanethiol (a volume equal to the aliquot), 6 mL of oleic acid:toluene 1:5 v/v, or 6 mL of TOP:toluene 1:6 v/v. The remainder of the reaction mixture was allowed to cool down, and became turbid. All nanocrystal manipulations were conducted under nitrogen as much as possible. We did however not notice any sign of decomposition upon exposure to ambient conditions.

Instrumental

TEM and electron diffraction measurements were performed with a Philips Tecnai scripting microscope (FEI) operating at 120 kV. Electron diffraction patterns were recorded with a camera constant of λL = 900 mmÅ. X-Ray Diffraction (XRD) diagrams were obtained by using a PW 1729 Philips diffractometer, equipped with a Cu Kα X-ray source (λ=1.5418 Å), operating at 40 kV and 20 mA. Samples were prepared by depositing a concentrated nanoparticles solution on a Si wafer substrate and drying in an inert atmosphere.

2.3 Results and discussion

The CaS nanocrystals were prepared by injection of a 100 mM oleylamine solution of $Ca(DPTC)_2$ in oleylamine at 250 °C. This led to the formation of a transparent, colorless product, which had the tendency to become turbid upon cooling and standing. The nanocrystals could be stabilized by addition of the co-surfactants hexanethiol, trioctylphosphine (TOP) or oleic acid, although with the latter detergent a slight degree of turbidity was observed at high concentrations. Thus, the use of the cation coordinating ligand oleylamine as the sole surfactant is not sufficient to yield a stable colloidal suspension, possibly due to the dynamic nature of the bonding between the amine donor and the metal ions [1]. The harder base

carboxylate (which is formed by deprotonation of oleic acid by the amine) improves the stability, which is not surprising given the hardness of Ca^{2+}. The beneficial effect of TOP suggests that anion coordination is also important for the stability of colloidal CaS nanocrystals.

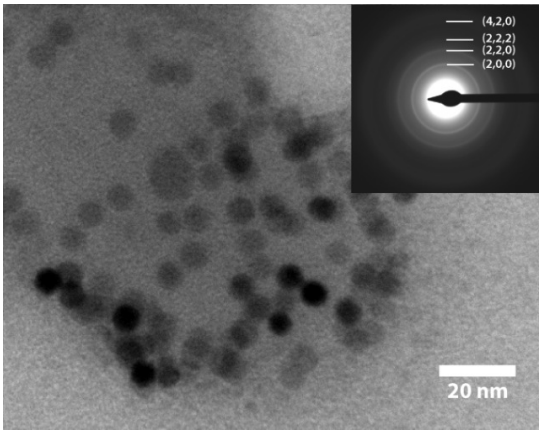

Figure 2.1 TEM image of CaS nanocrystals prepared by thermal decomposition of calcium (diisopropyldithiocarbamate) stabilized by hexanethiol. The insert shows the electron diffraction pattern with indication of the reflections.

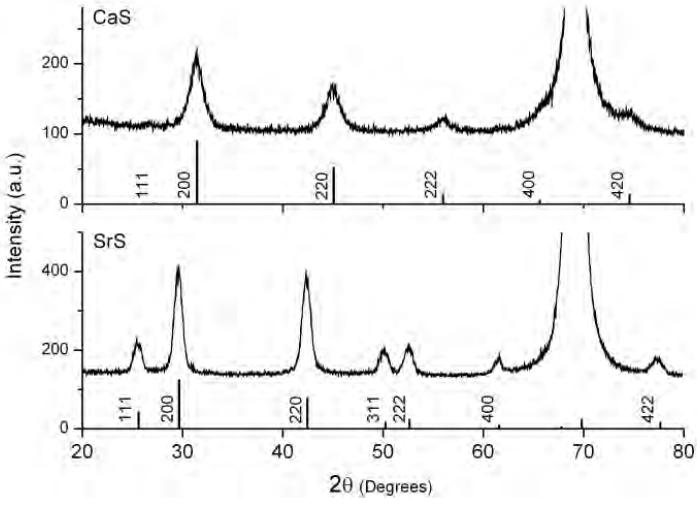

Figure 2.2 X-ray diffraction patterns of CaS (top) and SrS (bottom) nanocrystals with indices. The strong reflection near 70º originates from the silicon wafer used for deposition of the samples. It hides the 420 reflection of SrS.

Figure 2.1 shows a TEM image of the reaction product. It is seen that nearly spherical particles with a diameter of 7.6 ± 0.6 nm were formed, demonstrating that the method reported here yields small and monodisperse CaS nanoparticles. Preparation methods reported by others yielded CaS nanocrystals which were an order of magnitude larger, and moreover with a considerable variation in size and shape (*vide supra*). According to elemental analysis by energy dispersive X-ray spectroscopy, in the particles calcium and sulfur are present in an atomic ratio of 51.3 (±6.6): 48.7 (±7.7), providing clear evidence that CaS nanocrystals were formed. The electron diffraction pattern depicted in Figure 2.1 shows rings corresponding to distances of 2.86, 2.02, 1.63 and 1.29 Å. These maxima are assigned to the (2,0,0), (2,2,0), (2,2,2) and (4,2,0) reflections, respectively, of the cubic CaS crystal structure with a lattice constant of 5.686 Å (PDF-4+ database 01-077-2011) [6, 7]. The pattern is indicative of a high degree of crystallinity of the material. The electron diffraction results are confirmed by the X-ray diffraction pattern of the nanocrystals, which shows the same reflections (Figure 2.2). Hence, the data show that the single-source precursor method presented here gives access to small CaS nanocrystals with a narrow size distribution.

The diisopropyldithiocarbamate method also proved to be applicable to the synthesis of SrS nanocrystals. Thus, injection of a 100 mM oleylamine solution of $Sr(DPTC)_2$ in oleylamine at 250 °C gave SrS nanocrystals which could be stabilized by addition of TOP and oleic acid. The TEM image (Figure 2.3) reveals that also in this case nearly spherical particles with a narrow size distribution were formed. The diameter of the particles typically was somewhat larger than in the case of CaS, about 10 ± 1 nm. In the electron diffraction pattern reflections corresponding to distances of 3.47, 3.03, 2.14, 1.74, 1.52, 1.35 and 1.23 Å are present. These are consistent with the cubic SrS lattice with 6.020 Å lattice constant (PDF-4+ database 01-075-0895) [7]. The X-ray pattern of the SrS nanocrystals also is in agreement with this lattice (Figure 2.2), while according to the energy dispersive X-ray spectrum strontium and sulphur occur in an atomic ratio of 52.4 (±4.7): 47.6 (±1.5).

The synthesis of the CaS and SrS nanoparticles was repeated a number of times and in each case particles with comparable characteristics were obtained. Although not yet systematically investigated, factors as reaction temperature and reaction time seemed to have little effect on the nanoparticle size. This is in line with the formation of EuS nanoparticles from an europium dithiocarbamate complex, of which the size was hardly affected by the reaction conditions.[17]

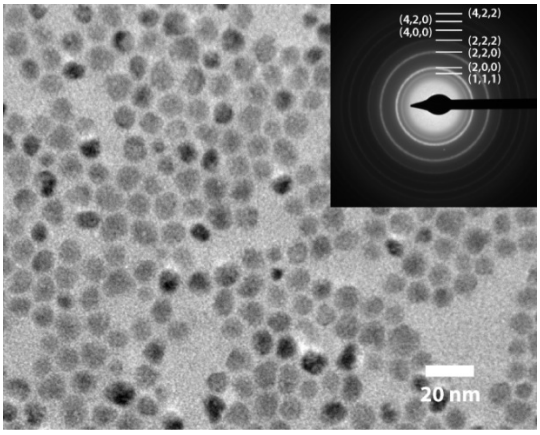

Figure 2.3 TEM image of SrS nanocrystals prepared by thermal decomposition of strontium (diisopropyldithiocarbamate) stabilized by oleic acid. Insert: electron diffraction pattern with indicated reflections. The (3,1,1) reflection is not resolved from the (2,2,2) reflection.

2.3 Conclusions

In conclusion, we have reported a hot injection method with a single-source precursor that enables the reproducible preparation of well-defined monodisperse 8-10 nm colloidal CaS and SrS nanocrystals. These nanocrystals might serve as host material for luminescent centers emitting in the visible or IR spectral region.

References

1. De Mello Donegá, C., Synthesis and properties of colloidal heteronanocrystals. *Chem. Soc. Rev.* **2011**, 40, 1512-1546.
2. Rogach, A. L., *Semiconductor Nanocrystal Quantum Dots. Synthesis, Assembly and Applications*. Springer: Wien, **2008**.
3. Yin, Y.; Alivisatos, A. P., Colloid nanocrystal synthesis and the organic-inorganic interface. *Nature* **2005**, 437, 664.
4. Lehmann, W., Activators and co-activators in calcium sulfide phosphors. *J. Lumin.* **1972**, 5, 87-107.
5. Crandall, R. S., Mechanism of electroluminescence in alkaline earth sulfides. *Appl. Phys. Lett.* **1987**, 50, 551-553.
6. Kumar, V.; Mishra, V.; Biggs, M. M.; Nagpure, I. M.; Ntwaeaborwa, O. M.; Terblans, J. J.; Swart, H. C., Electron beam induced green luminescence and degradation study of CaS:Ce nanocrystalline phosphors for FED applications. *Appl. Surf. Sci.* **2010**, 256, 1720-1724.
7. Wang, C.; Tang, K.; Yang, Q.; An, C.; Hai, B.; Shen, G.; Qian, Y., Blue-light emission of nanocrystalline CaS and SrS synthesized via a solvothermal route. *Chem. Phys. Lett.* **2002**, 351, 385-390.
8. Sun, B.; Yi, G.; Chen, D.; Zhou, Y.; Cheng, J., Synthesis and characterization of strongly fluorescent europium doped calcium sulfide nanoparticles. *J. Mater. Chem.* **2002**, 12, 1194-1198.
9. Kojima, Y.; Aoyagi, K.; Yasue, T., Afterglow mechanism and thermoluminesce of red-emitting $CaS:Eu^{2+}$, Pr^{3+} phosphor with incorporated Li^{+} ion upon visible light irradiation. *J. Lumin.* **2007**, 126, 319-322.
10. Le Masne de Chermont, Q*., et al.*, Nanoprobes with near-infrared persistent luminescence for *in vivo* imaging. *PNAS* **2007**, 104, 9266-9271.
11. Murray, C. B.; Norris, D. J.; Bawendi, M. G., Synthesis and characterization of nearly monodisperse CdE (E = S, Se, Te) semiconductor nanocrystallites. *J. Am. Chem. Soc.* **1993**, 115, 8706-8715.
12. Malik, M. A.; Afzaal, M.; O'Brien, P., Precursor Chemistry for Main Group Elements in Semiconducting Materials. *Chem. Rev.* **2010**, 110, 4417-4446.
13. Purdy, A. P.; George, C. F., Anhydrous dithiocarbamates. Potential precursors to alkaline earth sulfide materials. *Main Group Chem.* **1996**, 1, 229-240.
14. Trindade, T.; O'Brien, P.; Zhang, X.-M., Synthesis of CdS and CdSe nanocrystallites using a novel single-molecule precursors approach. *Chem. Mater.* **1998**, 9, 523-530.
15. Jung, Y. K.; Kim, J. I.; Lee, J.-K., Thermal decomposition mechanism of single-molecule precursors forming metal sulfide nanoparticles. *J. Am. Chem. Soc.* **2009**, 132, 178-184.
16. Hasegawa, Y.; Okada, Y.; Kataoka, T.; Sakata, T.; Mori, H.; Wada, Y., Synthesis and photophysical properties of EuS nanoparticles from the thermal reduction of novel Eu(III) complex. *J. Phys. Chem. B* **2006**, 110, 9008-9011.
17. Regulacio, M. D.; Kar, S.; Zuniga, E.; Wang, G.; Dollahon, N. R.; Yee, G. T.; Stoll, S. L., Size-dependent magnetism of EuS nanoparticles. *Chem. Mater.* **2008**, 20, 3368-3376.
18. Purdy, A. P.; George, C. F., Anhydrous dithiocarbamates. Potential precursors to alkaline earth sulfide materials. *Main Group Chem.* **1996**, 1, 229-240.

CHAPTER 3

Lanthanide Doped CaS and SrS Luminescent Nanocrystals

Abstract

In this chapter we introduce a single source precursor approach that successfully leads to monodisperse Ce^{3+} and Eu^{2+} doped CaS and SrS colloidal nanoparticles with diameters smaller than 10 nm. We found that the use of host and dopant precursors with similar decomposition temperatures is one of the key factors to successful doping. Growth-doping and nucleation-doping strategies allows us to achieve enhanced dopant incorporation and better control over the dopant concentration and location. For the growth-doping strategy, an additional shell of the host material is grown around a doped nanocrystal. This internalizes surface adsorbed Ce^{3+} or Eu^{2+} ions, hence greatly improving the luminescent properties of the doped nanocrystals. The nucleation-doping strategy can be applied when the decomposition temperatures of the precursors of the host material and of the dopant are largely different. The single-source precursor approach proposed here allows for a flexible design of synthesis strategies and has the potential to be widely applicable to the doping of sulfide-based colloidal nanoparticles with transition metal and lanthanide ions.

3.1 Introduction

Doped nanocrystals can address key problems in applications such as light emitting devices, photovoltaics, spintronics, and bioimaging, since doping enables further control over the electrical, optical, transport, and magnetic properties of nanomaterials.[1] Therefore, in recent years, a vast research effort has been devoted to the development of doped colloidal nanocrystals.

These efforts have focused primarily on two major classes of doped nanocrystals: (a) transition metal doped semiconductor nanocrystals, with mainly IIB-VI group compounds as host materials (*e.g.* CdSe,[2, 3] ZnSe,[4] and ZnS[5]), and (b) lanthanide doped wide band gap nanocrystals, which so far have been limited mainly to fluorides and phosphates.[6, 7] Binary alkali earth sulfides have not yet been obtained as colloidally stable monodisperse nanoparticles, despite their excellent properties as host material for a wide range of luminescent dopant ions (*e.g.*, low phonon energy, thermal stability, *etc*.).[8] The luminescence of bulk alkaline earth sulfides doped with lanthanide ions, like Ce^{3+} and Eu^{2+}, has been extensively studied. The high quantum efficiencies, saturated emission colors, and high thermal stability of these materials make them interesting phosphors for color conversion in LED-based lighting. Moreover, CaS:Ce^{3+},Sm^{3+} and CaS:Eu^{2+},Sm^{3+} are well-known afterglow (or persistent luminescent) materials.[9, 10] Therefore, lanthanide doped alkaline earth sulfide nanoparticles are promising materials for a number of applications. For example, CaS:Ce^{3+},Sm^{3+} and CaS:Eu^{2+},Sm^{3+} colloidal nanoparticles are excellent candidates for non-toxic afterglow nanolabels for background-free biomedical imaging.[11] There are also potential applications such as spectral converters, down-shifters in luminescent solar concentrators,[12] or color converters in white light LEDs.[13]

The incorporation of dopants into colloidal nanocrystals is, however, not always straightforward, and is often the limiting factor in the development of new materials.[14] Previously reported synthetic protocols for doped nanoparticles of IIA-VI materials have relied on co-precipitation or hydrothermal methodologies,[15] but yielded only relatively large particles (tens to hundreds of nanometers), with undefined shapes and large size distributions.[16] The lack of synthetic methodologies for well-defined and monodisperse doped IIA-VI nanoparticles has greatly hampered the development of this class of materials.

To achieve doping in nanocrystals, in addition to simply introducing impurity precursors into traditional colloidal synthetic protocols, alternative methods, such as the use of inorganic clusters,[17, 18] and cation exchange,[19, 20] have also been

successfully reported. More sophisticated synthetic strategies, *e.g*. growth-doping and nucleation-doping.[21, 22] have also been developed in recent years.

The use of single-source precursors was originally developed for the synthesis of II-VI semiconductor nanocrystals[23] and transition metal sulfide nanocrystals.[24-26] As an extension of this method, we have recently successfully synthesized monodisperse alkaline earth sulfide (*viz*., CaS and SrS) nanocrystals (8-10 nm diameter) by using dithiocarbamate complexes as single-source precursors (see Chapter 2).[27] In this chapter, we successfully adapt the single-source precursor methodology to the synthesis of monodisperse (*viz*. < 10% size dispersion) Ce^{3+} and Eu^{2+} doped CaS and SrS colloidal nanocrystals. In order to identify the correct conditions for successful doping, we studied the relation between the properties of the precursors and the doping efficacy for different doping strategies (i.e., nucleation or growth doping). The single-source precursor approach proposed here allows for a flexible design of synthesis strategies and has the potential to be widely applicable to the doping of sulfide-based colloidal nanoparticles with transition metal and lanthanide ions.

3.2 Experimental

Single-source precursors synthesis.

Calcium diisopropyldithiocarbamate, $Ca(DPTC)_2$, was prepared following the procedures reported by Purdy and George.[28] A similar method was applied for the synthesis of strontium diisopropyldithiocarbamate $Sr(DPTC)_2$.[27] The dopant precursor Europium dietyldithiocarbamate dietylammonium salt, $Eu(DDTC)_4$, was prepared according to literature.[29]

Cerium diethyldithiocarbamate diethylammonium salt, $Ce(DDTC)_4$, was prepared under N_2 atmosphere. 10 ml 0.1M $Ce(NO_3)_3 \cdot 6H_2O$(99.99%, Aldrich) solution in anhydrous iso-propanol was mixed with 10ml 0.3 M solution of diethylammonium diethyldithiocarbamate (98%, Alfa) in iso-propanol. A bright yellow crystalline precipitate was obtained and isolated by centrifugation. The powder obtained was washed with iso-propanol, dried under vacuum, and stored under N_2 to prevent oxidation.

Europium butyldithiocarbamate butylamonium salt, $Eu(BDTC)_4$, was synthesized as follows. n-Butylamine (1 ml, 10mmol) and carbon disulfide (0.3 ml, 5 mmol) were added into 5 ml anhydrous iso-propanol, and stirred under N_2 for 10 min.

Then, 0.32 g anhydrous europium chloride ($EuCl_3$, 1.25 mmol) dissolved in 5 ml anhydrous iso-propanol was added dropwise. The initially colorless solution turned orange/red and eventually produced an orange/red precipitate, which was collected through centrifugation, washed with anhydrous iso-propanol and dried under vacuum.

Determination of amine-assisted decomposition temperature of precursors

The amine-assisted decomposition temperatures of $Ce(DDTC)_4$, $Eu(BDTC)_4$ and $Eu(DDTC)_4$ were determined by observing the change in the solution color while heating up in Oleylamine. Since $Ca(DPTC)_2$ and $Sr(DPTC)_2$ do not change color while decomposing in oleylamine, their decomposition temperatures were determined by conducting the generated H_2S gas into an aqueous solution of lead acetate in which PbS black precipitate was formed.

Synthesis of Ce^{3+} doped SrS and CaS nanocrystals through growth doping method.

The nanocrystal (NC) syntheses were carried out in a N_2 filled glovebox. Oleylamine (70%, Aldrich) was dried under vacuum at 180 ºC for 3 h before use to remove moisture and oxygen. For a typical synthesis, 0.1 M (0.2 M for larger or 0.025M for smaller particle sizes) $Sr(DPTC)_2$ ($Ca(DPTC)_2$ for CaS NC synthesis) solution in oleylamine and a calculated amount of $Ce(DDTC)_4$ in oleylamine were freshly prepared before use. Then 2 ml of $Sr(DPTC)_2$ and 1 ml $Ce(DDTC)_4$ precursor solution were mixed and quickly injected into a three necked round bottom flask containing 6 ml oleylamine at 250 ºC. After the injection, the temperature dropped to about 220 ºC, and was brought back to 250 ºC. At this temperature, 1 ml 0.05 M $Sr(DPTC)_2$ solution was added 0.2 ml/min into the reaction flask for growing a SrS shell. During the shell growth, the solution turned from light yellow to deep yellow. Subsequently, the reaction temperature was increased to 270 ºC for 1 hour. Aliquots were taken at different steps of the reaction. The as-synthesized SrS or CaS NCs are capped by oleylamine, which does not provide sufficient colloidal stability at temperatures below 120 ºC, leading to partial NC aggregation and turbidity. Therefore, the aliquots or product solution were taken out at temperatures above 120 ºC and immediately redispersed into 10 ml of a solution containing 0.6 ml oleic acid and 20 mg tetradecylphosphonic acid (TDPA, 97% Aldrich) in toluene. In this way, the surface of the NCs is capped with oleic acid and TDPA, which are much stronger ligands than oleylamine. After recapping, the NCs can be washed several times by precipitation with methanol followed by centrifugation, without losing their colloidal stability. The nanoparticles can be

redispersed in a number of non-polar solvents, such as toluene and hexane, yielding colloidally stable and optically transparent suspensions.

Synthesis of Eu^{2+} doped SrS and CaS nanocrystals through growth doping method.

The method used to synthesize Eu^{2+} doped SrS (or CaS) NCs was similar to that used for Ce doped CaS (SrS) NCs, using $Eu(BDTC)_4$ as the dopant precursor. The only difference is that the shell growth and annealing temperatures were decreased to 200 ºC. The annealing was carried out for 15 min.

Synthesis of Eu^{2+} doped SrS and CaS nanocrystals through nucleation doping method.

Firstly, EuS NC cores were synthesized by injecting 1 ml of freshly prepared 0.05 M $Eu(DDTC)_4$ solution in oleylamine into a three-necked round bottom flask containing 6 ml oleylamine at 320 ºC. The reaction solution turned purple immediately after injection. The subsequent growth of a SrS or CaS shell was performed in the same reaction flask at 250 ºC by slowly adding 2 ml 0.1 M SrS (or CaS) in oleylamine. Aliquots were taken at different steps of the reaction for analysis. The NCs were recapped and washed using the same procedure described above for growth doping method.

Characterization

X-Ray Diffraction (XRD) diagrams were obtained by using a PW 1729 Philips diffractometer, equipped with a Cu Kα X-ray source (λ=1.5418 Å), operating at 40 kV and 20 mA. The sample for XRD analysis was prepared by depositing a concentrated solution of NCs on a Si wafer substrate and evaporating the solvent under inert atmosphere. For optical measurements, washed nanocrystals were redispersed in hexane and loaded in sealed quartz cuvets. Absorption spectra were recorded on a Perkin-Elmer Lambda 950 UV/VIS/IR spectrophotometer. Emission and excitation spectra were measured on Edinburgh Instruments FLS920 spectrofluorometer equipped with a 450 W Xe lamp and double monochromators for both emission and excitation (gratings blazed at 300 nm or 500 nm). The emitted light was detected with a Hamamatsu R928 PMT detector. The spectra were corrected for the instrumental response.

3.3 Results and discussion

Growth doping method for SrS:Ce^{3+} and CaS:Ce^{3+} NCs

The successful synthesis of SrS and CaS NCs by thermal decomposition of $Sr(DPTC)_2$ and $Ca(DPTC)_2$ in oleylamine,[27] opens up the way to a potentially straight-forward method to synthesize Ce^{3+} doped SrS or CaS nanoparticles by introducing Ce dithiocarbamate complex ($Ce(DDTC)_4$) as a single source impurity precursor, and thermally decomposing the precursors of both the host material and the dopant together through a hot-injection strategy. We observed that the sizes of the NCs collected from the reaction solution only a few seconds after precursor injection and after several minutes do not significantly differ (data not shown). This implies that the NCs nucleate and reached their final size within a few seconds in oleylamine at 250 ºC. Therefore, the size of SrS:Ce^{3+} or CaS:Ce^{3+} NCs are mainly controlled by adjusting the concentration of precursors, with higher concentrations leading to larger NC sizes. The coordinating solvent, oleylamine, also assists the decomposition of dithiocarbamate salts by lowering the decomposition temperature.[25] This mechanism has been described in detail recently.[30]

Figure 3.1a shows the absorption spectrum of the SrS:Ce^{3+} NCs obtained after the co-injection of Sr and Ce precursors (5% $Ce(DDTC)_4$). The broad absorption band at 430 nm can be ascribed to the $4f^1$->$5d^1$ transition of Ce^{3+} ions in SrS, and is good agreement with the values reported for bulk SrS:Ce.[31] The emission spectrum of the SrS:Ce^{3+} NCs obtained after the co-injection (Figure 3.1b) consists of a broad emission band centered at ~480 nm with a shoulder at ~540 nm. An emission spectrum showing two bands split by about 2000 cm^{-1} is typical for Ce^{3+} emission. Transitions from the 5*d* excited state to the 2F ground state give rise to the double band structure due to the 2000 cm^{-1} spin-orbit splitting of the ^2F ground state into a $^2F_{5/2}$ and $^2F_{7/2}$ state. The position of the absorption and emission bands are sensitive to the local surroundings. Usually, Ce^{3+} emission is in the ultraviolet or blue spectral region. The emission wavelength is determined by the energy of the lowest 5*d* state, the emitting state. Only for a few host lattices Ce^{3+} emission is observed in the yellow or orange spectral region. In case of a very large crystal field splitting and/or in a highly covalent host lattice the energy of the lowest energy excited 5*d* state is shifted to sufficiently low energies to give yellow or orange emission (see also Figure 1.6a). In SrS and CaS, the highly covalent character of the S^{2-} ligands is the main reason for the shift of the *d-f* emission to the yellow spectral region. The emission spectra for Ce^{3+} in the CaS and SrS nanocrystals are the same as for Ce^{3+} in the bulk CaS or SrS. The emission results from a localized transition on the Ce^{3+} ion and the energy is determined by the interaction

between Ce^{3+} and the coordinating ligands. In this way, the absorption and emission spectra of Ce^{3+} are a sensitive probe to confirm successful doping of Ce^{3+} into the CaS or SrS nanocrystal. For Ce^{3+} absorbed on the surface the local coordination will be different and the differences in crystal field and covalency of the local surroundings will influence the energy of the lowest 5*d* state resulting in absorption and emission spectra that differ from those for Ce^{3+} inside the CaS or SrS crystals. The similarity of the absorption and emission spectra shown in Figure 3.1 to those observed for Ce^{3+} in bulk SrS and CaS confirm that Ce^{3+} has been successfully incorporated in the sulfide nanocrystals. Moreover, luminescence quenching can be expected for Ce^{3+} at the surface due to surface defect states. The ability to assign emission of Ce^{3+} to ions incorporated in the nanocrystals based on the luminescence spectra is important, since there are few analytical techniques that are able to distinguish between dopant ions at the surface and dopant ions incorporated in the nanocrystal.[1]

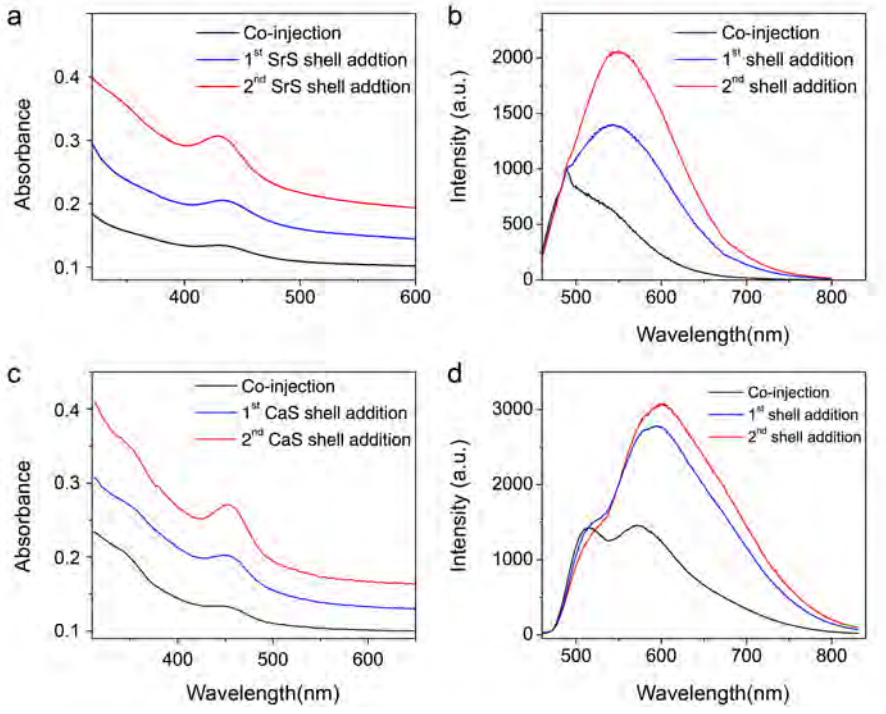

Figure 3.1. (a) Absorption and (b) emission spectra of SrS:Ce^{3+} nanocrystals (NCs) obtained by the growth doping method. (c) Absorption and (d) emission spectra of CaS:Ce^{3+} nanocrystals (NCs) through the growth doping method.

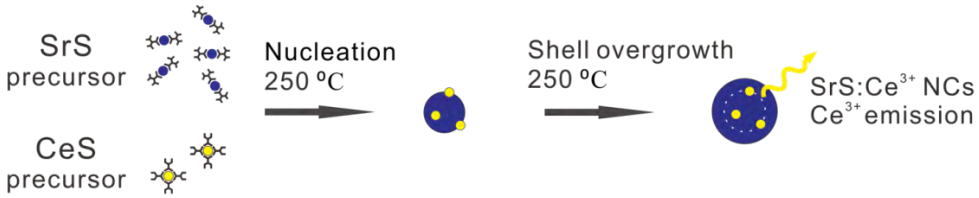

Figure 3.2. Schematic illustration of the synthesis of SrS:Ce^{3+} NCs by using the single-source precursors and growth doping strategy.

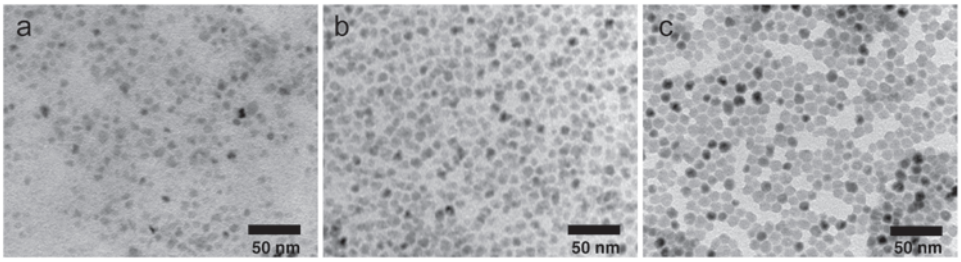

Figure 3.3. TEM images of SrS:Ce^{3+} NCs obtained by the growth doping method. (a) After co-injection of lattice and dopant precursors. (b) After shell growth. (c) After annealing at 250 ºC for 1h.

Although the results clearly show that Ce^{3+} doping in SrS can be achieved through the co-injection of Ce and Sr precursors, the relatively weak Ce^{3+} absorption peak and low emission intensities suggest that a substantial fraction of the Ce^{3+} ions are at the surface of the SrS NCs. Previously, in many doped NC systems (*eg.* CdS:Co^{2+},[32] ZnSe:Mn^{2+}[21] and CdS/ZnS:Mn^{2+} [33]), surface-bound impurity ions have been internalized through epitaxial growth of additional layers of host materials. In a similar way, a SrS shell was grown over the SrS:Ce^{3+} NCs formed after the co-injection, by slowly adding $Sr(DPTC)_2$ precursor solution to the reaction mixture at 250 ºC (as schematically illustrated in Figure 3.2). Figure 3.3 shows that the SrS:Ce^{3+} NCs formed after the co-injection have irregular nearly spherical shapes and diameters around 8-10 nm with a rather large polydispersity. After the addition of the SrS shell precursors, the size of the NCs increased to 10-12 nm (Figure 3.3b), confirming the growth of a SrS shell around the preexisting SrS:Ce NCs. After annealing at 270 ºC for 1h, the NCs became more spherical and the size distribution was narrowed (Figure 3.3c). During the addition of shell precursors, the solution color darkened from light to deep yellow. This color change is

clearly reflected in the absorption spectra (Figure 3.1a), since the Ce^{3+} absorption peak at 430 nm gradually increases with the precursor addition. Correspondingly, the intensity of the Ce^{3+} emission dramatically increases and the peak position shifts to longer wavelengths (Figure 3.1b). The emission peak at 540 nm ($5d \rightarrow {}^2F_{7/2}$) increases more pronouncedly than the peak at 480 nm ($5d \rightarrow {}^2F_{5/2}$) and becomes dominant. These observations indicate that the SrS shell growth has successfully internalized Ce^{3+} ions in the SrS NCs. The red-shift of the emission peak was also observed with increasing of the Ce^{3+} concentration in the NCs, and will be discussed in more detail below.

The growth doping strategy was also successfully applied for the synthesis of CaS:Ce^{3+} NCs, owing to the chemical similarities between Ca and Sr. After the co-injection of Ca and Ce precursors, a small absorption peak at 450 nm and the corresponding double emission peak at 514 nm and 572 nm appeared (Figure 3.1c,d), consistent with the absorption and emission peaks of Ce^{3+} in bulk CaS.[31, 34] Similar to the case of SrS:Ce NCs discussed above, the intensity of the Ce^{3+} absorption and emission peaks increased upon growth of CaS shells over the CaS:Ce NCs formed after the co-injection, confirming the internalization of Ce^{3+} ions in the CaS NCs.

The as-synthesized SrS:Ce^{3+} and CaS:Ce^{3+} NCs are capped with oleylamine and tend to aggregate in solution due to detaching of surface ligands, since oleylamine is a rather dynamic surfactant. Therefore, a recapping process with oleic acid and TDPA, which binds stronger to the SrS or CaS surface, is performed immediately after the NC syntheses to provide colloidal stability to the doped NCs. The final product can be dispersed well in common non-polar solvents yielding optically transparent and stable suspensions even after several washing cycles. High-resolution TEM images (Figure 3.4a) confirm the single-crystalline nature of the NCs, since no grain boundaries are observed within individual nanoparticles. Electron diffraction patterns are consistent with the rock salt structure of SrS (Figure 3.4b).

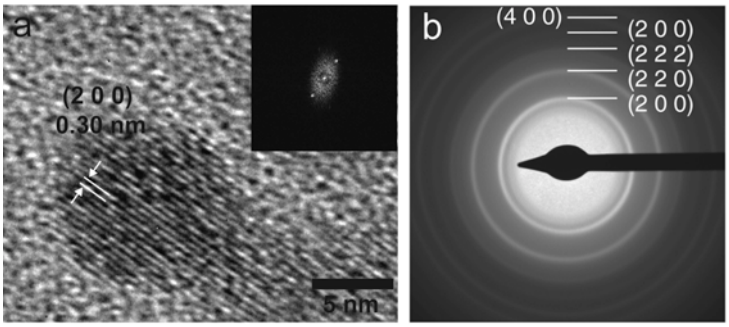

Figure 3.4. (a) HR-TEM image of SrS: Ce^{3+}. Insert is the Fourier transform transition of the image. (b) Electron diffraction pattern of SrS:Ce^{3+} and the assignments of diffraction rings.

Effect of the Ce^{3+} concentration on luminescence of SrS and CaS: Ce^{3+} NCs.

To investigate the concentration dependence of the optical properties, a series of SrS:Ce^{3+} and CaS: Ce^{3+} NCs was synthesized by the growth doping method with varying amount of Ce precursors. The emission spectra are observed to significantly red-shift and broaden with increasing Ce^{3+} concentration in the reaction mixture for both SrS:Ce and CaS:Ce NCs (Figure 3.5a, b). A dramatic change in the relative intensity of two emission peaks (viz., $^2D(5d)$-$^2F_{5/2}(4f)$ and $^2D(5d)$-$^2F_{4/2}(4f)$) is also observed. Similar concentration effects have been reported for bulk SrS:Ce^{3+} or CaS:Ce^{3+} phosphors, and were ascribed to radiative (self-absorption) and non-radiative energy transfer from Ce^{3+} ions emitting at higher energy (donors) to Ce^{3+} ions emitting at lower energies.[35] This effect is quite pronounced in the SrS and CaS NCs, leading to a change of luminescence color for CaS:Ce3+ NCs from green (to page 53)

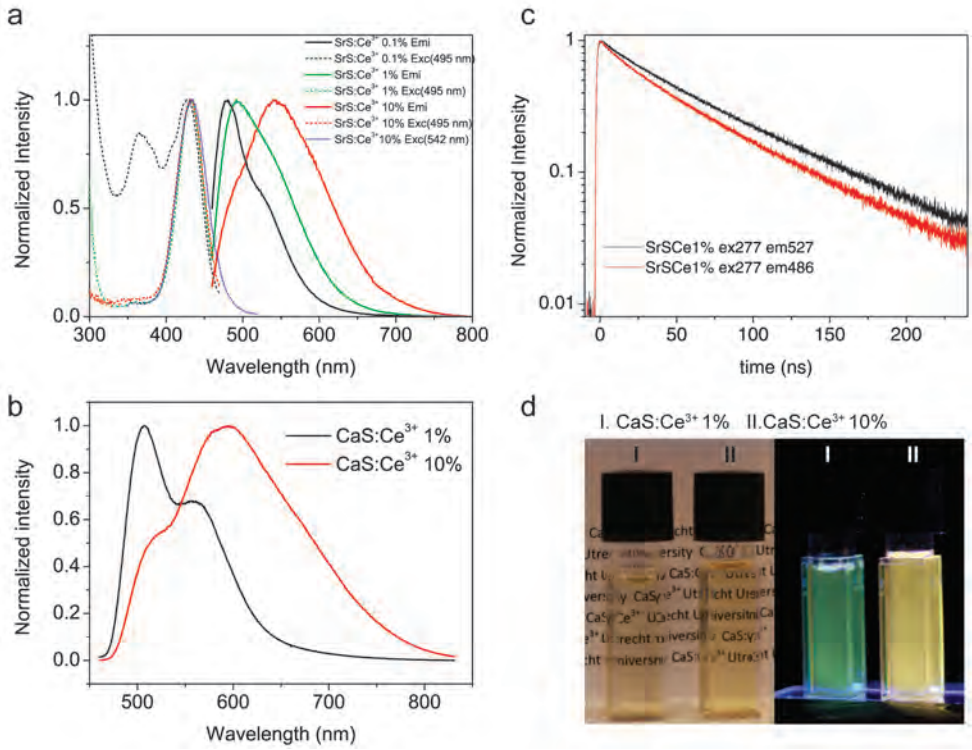

Figure 3.5. (a) Emission (solid line) and excitation (dashed line) spectra of SrS:Ce^{3+} with 0.1%, 1%, and 10% Ce in the reaction mixture. All emission spectra are recorded under excitation at 430 nm. Excitation spectra are recorded at indicated emission wavelengths. The peak at 430 nm is direct excitation of the Ce^{3+} ions, and 375nm is due to energy transfer from defect state to Ce^{3+} ions. Only for low Ce^{3+} concentration (0.1%), the 375 nm band is observed. At higher Ce^{3+} concentrations, the direct excitation at 430 nm became dominant. (b) Emission spectra of CaS:Ce^{3+} with 1% and 10% of Ce in the reaction mixture, excited at 450 nm. (c) luminescence decay curve of SrS:Ce^{3+} emission at 488 nm and 527 nm, excited with a pulsed UV diode laser at 277 nm. (d) Solution of a colloidal suspension of CaS:Ce^{3+} 1% and 10% NCs in toluene under day light (left) and UV irradiation (right).

to yellow, when the Ce^{3+} concentration increases from 1% to 10% (Figure 3.5d). Another possible explanation for the red-shift of the Ce^{3+} emission is that the local crystal field splitting may change due to the distortion of the SrS or CaS lattice caused by increasing the Ce^{3+} concentration.[36] However, in the present case the

excitation spectra of the Ce^{3+} emission in SrS NC remained essentially unaffected by the increasing Ce^{3+} concentration and are also independent of emission wavelength (Figure 3.5a). This implies that the change of crystal field is too small to significantly contribute to the spectral shift. Luminescence decay measurements on SrS:Ce^{3+} NCs while monitoring the 480 and 540 nm emission peaks gave nearly single-exponential decay curves, with fitted life time of 56 ns and 65 ns, respectively (Figure 3.5c). These values are larger than those reported for bulk SrS:Ce (27-36 ns).[37, 38] The excitation wavelength (277 nm) corresponds to absorption by the SrS lattice, showing that energy transfer from the lattice to the Ce^{3+} ions is fast and efficient, which again confirms the successful doping of Ce^{3+} ions in the SrS lattice.

Growth doping method for SrS: Eu^{2+} NCs.

Based on the success of the growth doping method for Ce^{3+} in SrS and CaS, we applied this strategy also to the doping of Eu^{2+} in SrS and CaS NCs. Since $Eu(DDTC)_4$ was previously used as single-source precursor for the synthesis of EuS nanoparticles,[29, 39] we tried to use it as Eu^{2+} dopant precursor in the growth doping method. However, the doping was not successful and no evidence of incorporation of Eu^{2+} in the SrS NCs was found. Only when the reaction temperature was increased to temperatures as high as 340 ºC, weak Eu^{2+} emission was observed in some syntheses, but with poor reproducibility. These observations lead to the hypothesis that the difference of decomposition temperature (or decomposition rate at fixed temperature) between dopant and lattice precursors is a crucial factor for the successful doping via single-source precursor method. In the present case, as summarized in Table 1, CeDPTC and $Sr(DPTC)_2$ have very close decomposition temperatures (difference <10 ºC), while the difference between $Eu(DDTC)_4$ and $Sr(DPTC)_2$ is very large (>120 ºC). Therefore, using an Eu single-source precursor with a decomposition temperature closer to that of $Sr(DPTC)_2$ could potentially lead to successful Eu doping. It is known that the metal complex chelated with monoalkyl dithiocarbamate as ligand decomposes at lower temperatures than the complex with dialkyldithiocarbamate.[40] To that end, Eu butyldithiolcarbamate, $Eu(BDTC)_4$ was synthesized and indeed decomposes in oleylamine at a much lower temperature (viz. 131 ºC), forming EuS.

Table 1. Decomposition temperatures of single-source precursors in oleylamine.

Precursors	Decomposition Temperature (ºC)	Phenomenon used to indicate decomposition
$Ca(DDTC)_2$	140	Generation of H_2S gas, formation of CaS
$Sr(DDTC)_2$	140	Generation of H_2S gas, formation of SrS
$Ce(DDTC)_4$	150	Dark brown solution, formation of CeS
$Eu(DDTC)_4$	>260	Purple solution, formation of EuS
$Eu(BDTC)_4$	131	Purple solution, formation of EuS

Next, $Eu(BDTC)_4$ was used as the dopant precursor for $SrS:Eu^{2+}$ NCs using the growth doping method. After the co-injection of Eu and Sr precursors at 250 ºC, additional $Sr(DPTC)_2$ precursors were slowly added at a lower growth temperature (200 ºC). Upon shell growth, the solution color gradually changed from light orange to red. Absorption spectra show that a broad absorption peak at 445 nm appeared after the co-injection and gradually increased with the shell growth (Figure 3.6a). This peak is ascribed to the $4f^7 \rightarrow 4f^6 5d^1(T_{2g})$ transition of Eu^{2+} in SrS, based on the similar shape and wavelength associated for the *f-d* transition in the bulk $SrS:Eu^{2+}$ phosphors.[31, 41] Therefore, like in the case of Ce^{3+} doping, the increase in the intensity of this absorption peak is a good indicator for the incorporation of Eu^{2+} into the nanocrystal during the SrS shell growth. Accordingly, the characteristic Eu^{2+} emission peak at 610 nm also gradually increased and red-shifted with additional SrS shell growth, as a result of the increasing amount of incorporated Eu^{2+} (Figure 3.6b). It should be noted that Eu^{2+} emission could only be observed when the shell growth was carried out at relatively low temperatures (200 ºC). The use of higher temperatures (*e.g.*, 250 ºC, which was successful for $SrS:Ce^{3+}$ doping), leads to incorporation of Eu^{2+}, as indicated by increase of Eu^{2+} absorption (data not shown), but no emission or very weak emission. This observation can be explained by considering that at higher shell growth temperatures Eu^{2+} ions will be able to diffuse into and through the SrS shell, thereby reaching the surface layer, where they will experience emission quenching due to interaction with surface defect states. This mechanism is schematically depicted in Figure 3.7.

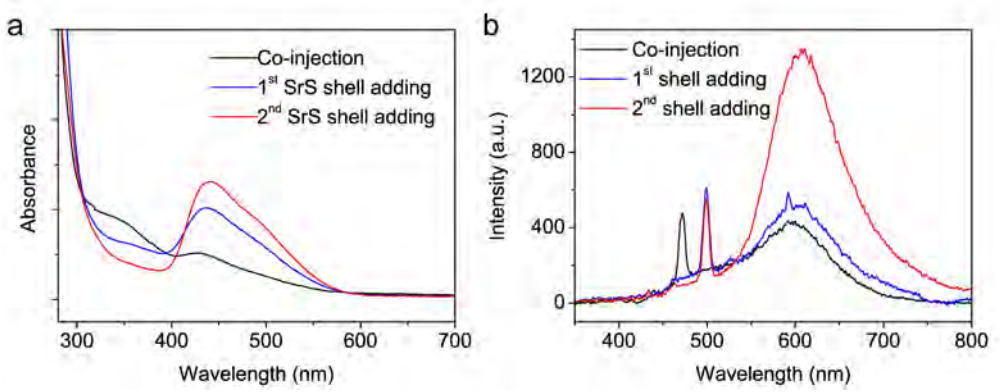

Figure 3.6. (a) Absorption and (b) emission spectra of SrS:Eu^{2+} NCs obtained by the growth doping method, excited at 430 or 450 nm. The peak at 460 and 500 nm are Raman scattering of the excitation light.

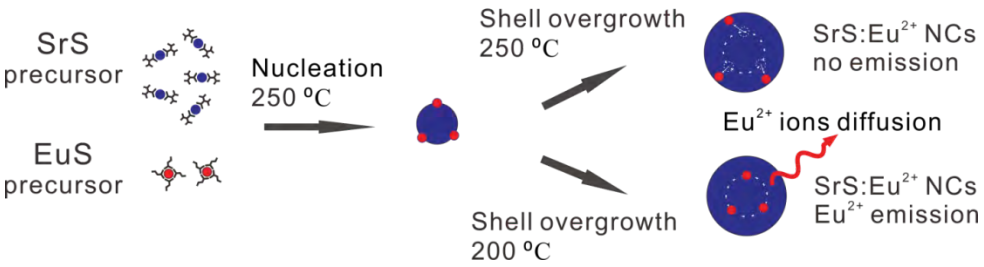

Figure 3.7. Schematic illustration of the synthesis of SrS: Eu^{2+} NCs by using single-source precursors method and the growth doping strategy. Eu^{2+} emission can be obtained only when the shell growth temperature is lower than 250 ºC.

Nucleation doping method for SrS: Eu^{2+} NCs.

The results discussed above suggest that at sufficiently high temperatures Eu^{2+} is able to diffuse through SrS. This is not unexpected, since Eu^{2+} in VI coordination and Sr^{2+} have the same charge and very similar ionic radii (1.17 and 1.18 Å, respectively). Based on this assumption, we applied another doping strategy, nucleation doping, to the synthesis of SrS:Eu^{2+}. This strategy relies on diffusion of dopant ions from nuclei of the pure dopant material into a shell of the host material grown around the nuclei. It was first introduced by Peng *et al.* for the synthesis of

Mn^{2+} doped ZnSe nanoparticles.[21] Here we show that this approach can be successfully extended to lanthanide ion doped wide band-gap nanocrystals (Figure 3.8).

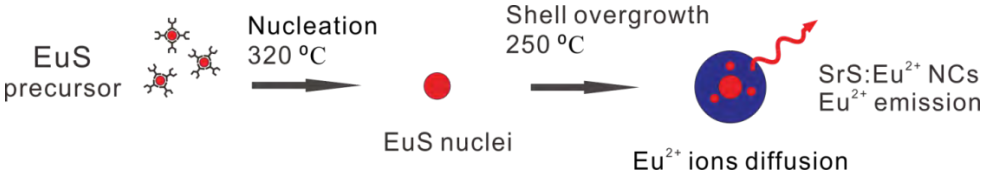

Figure 3.8. Schematic illustration of the synthesis of SrS:Eu^{2+} NCs by using single-source precursors and the nucleation doping strategy.

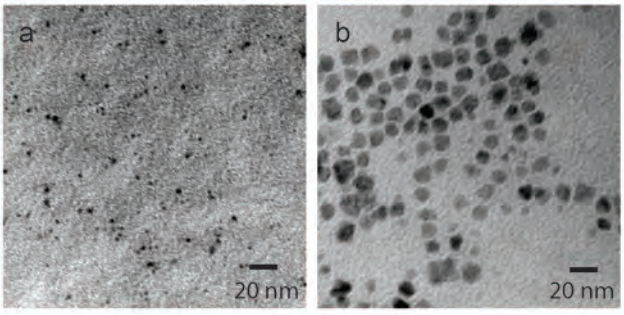

Figure 3.9. Synthesis of SrS:Eu^{2+} NCs by the nucleation doping strategy. (a) EuS core NCs. (b) EuS/SrS core/shell NCs after SrS shell growth.

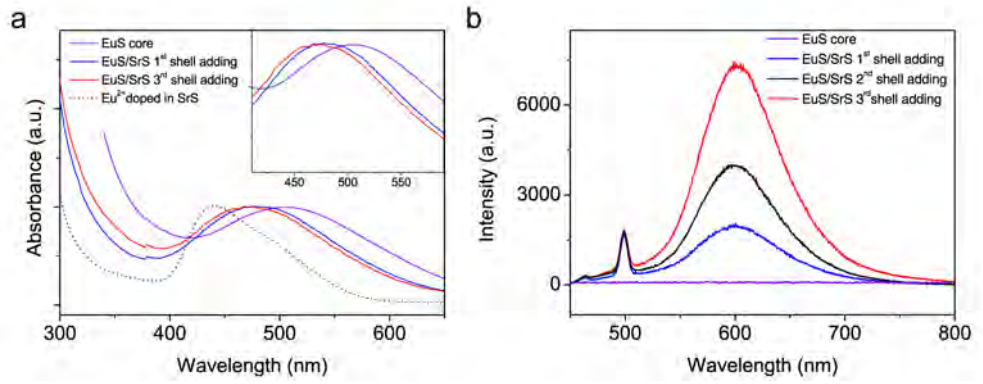

Figure 3.10. (a) Absorption and (b) emission spectra of SrS:Eu^{2+} nanocrystals (NCs) through the nucleation doping method. The emission spectra are collected with excitation at 450 nm. The peak at 600 nm are Raman scattering of the excitation light.

First, small sized (3-4 nm) EuS cores were synthesized through rapid decomposition of $Eu(DDTC)_4$ in oleylamine at 320 ºC. The formation of small EuS nuclei was confirmed by TEM imaging (Figure 3.9a) and optical absorption spectroscopy (Figure 3.10a). The EuS NCs have characteristic absorption band centered at 504 nm ($4f^7$->$4f^6 5d^1$ (T_{2g}) transition [39, 42]). Here, the $Eu(DDTC)_4$ precursor with higher decomposition temperature (Table 1) was used for the synthesis of the EuS core NCs to achieve smaller particle sizes. In contrast, decomposition of $Eu(BDTC)_4$ lead to larger particle sizes and wider size distribution. Subsequently, in the same reaction solution, the synthesized EuS core NCs were used as "seeds" for heterogeneous nucleation and growth of a SrS shell through slow addition of $Sr(DPTC)_2$ precursor at 250 ºC. The final EuS/SrS core/shell NCs have sizes ranging from 12 to 20 nm (Figure 3.9b). Absorption and emission spectra were measured on purified NC samples taken during the SrS shell growth over the EuS core NCs (Figure 3.10a), and show that the lowest energy absorption band shift from 504 nm to 480 nm after addition of SrS precursors. This blue shift continues with the thickening of the SrS shell. This indicates that although EuS/SrS NCs still contained an EuS core, a significant amount of Eu^{2+} ions has diffused into the SrS shell, leading to a shift of the absorption peak towards the values observed for SrS:Eu^{2+} (440 nm). At the same time, the intensity of the Eu^{2+} emission at 610 nm gradually increased during the shell growth, similar to the SrS:Eu^{2+} emission observed in the growth doping method.

The results presented above show that the nucleation doping strategy is not only an alternative way to achieve doping, but also complementary to the growth doping strategy. For single source precursor method, it can be applied for systems which have large differences in decomposition temperatures between dopant and lattice precursors, since the decoupling of NC growth and doping allows decomposing the precursors under different conditions.

3.4 Conclusions

In conclusion, through a single-source precursor approach, we have successfully synthesized monodisperse and colloidally stable Ce^{3+} and Eu^{2+} doped SrS and CaS luminescent nanocrystals with diameters around 10 nm. We found that the use of host and dopant precursors with similar decomposition temperatures is one of the key factors to successful doping by using the growth doping method. The single-source precursor method can be applied in various sophisticated synthetic strategies to achieve efficient doping. In the growth doping strategy, co-decomposition of dopant and lattice precursors is followed by an additional shell growth of the host material, which internalizes surface bound Ce^{3+} or Eu^{2+} ions, hence greatly improving the luminescence properties of the doped nanocrystals. In the nucleation doping strategy, small nanocrystals of the dopant material are first synthesized and subsequently over-coated with a shell of the lattice material. The shell growth is accompanied by diffusion and intermixing of dopant ions into the shell, leading to successful doping. The single-source precursor approach proposed here allows for a flexible design of synthesis strategies and has the potential to be widely applicable to the doping of binary sulfides-based colloidal nanoparticles with various kinds of ions.

References

1. Norris, D. J.; Efros, A. L.; Erwin, S. C., Doped nanocrystals. *Science* **2008**, 319, 1776-9.
2. Beaulac, R. m.; Archer, P. I.; van Rijssel, J.; Meijerink, A.; Gamelin, D. R., Exciton Storage by Mn^{2}+ in Colloidal Mn^{2+}-Doped CdSe Quantum Dots. *Nano Lett.* **2008**, 8, 2949-2953.
3. Sahu, A.*, et al.*, Electronic Impurity Doping in CdSe Nanocrystals. *Nano Lett.* **2012**, 12, 2587-2594.
4. Pradhan, N.; Peng, X., Efficient and Color-Tunable Mn-Doped ZnSe Nanocrystal Emitters: Control of Optical Performance via Greener Synthetic Chemistry. *J. Am. Chem. Soc.* **2007**, 129, 3339-3347.
5. Suyver, J. F.; Wuister, S. F.; Kelly, J. J.; Meijerink, A., Luminescence of nanocrystalline ZnSe:Mn2+. *Phys. Chem. Chem. Phys.* **2000**, 2, 5445-5448.
6. Wang, G.; Peng, Q.; Li, Y., Lanthanide-doped nanocrystals: synthesis, optical-magnetic properties, and applications. *Acc. Chem. Res.* **2011**, 44, 322-32.
7. Wang, F.; Liu, X., Recent advances in the chemistry of lanthanide-doped upconversion nanocrystals. *Chem. Soc. Rev.* **2009**, 38, 976-89.
8. Smet, P. F.; Moreels, I.; Hens, Z.; Poelman, D., Luminescence in Sulfides: A Rich History and a Bright Future. *Materials* **2010**, 3, 2834-2883.
9. Jia, D. D.; Zhu, J.; Wu, B. Q., Trapping centers in CaS : Bi3+ and CaS : En(2+),Tm3+. *J. Electrochem. Soc.* **2000**, 147, 386-389.
10. Tamura, Y.; Shibukawa, A., Optical Studies of Caseu, Sm Infrared Stimulable Phosphors. *Jpn J Appl Phys 1* **1993**, 32, 3187-3196.
11. le Masne de Chermont, Q.*, et al.*, Nanoprobes with near-infrared persistent luminescence for in vivo imaging. *Proc. Natl. Acad. Sci. U. S. A.* **2007**, 104, 9266-71.
12. Krumer, Z.*, et al.*, Tackling self-absorption in luminescent solar concentrators with type-II colloidal quantum dots. *Sol. Energy Mater. Sol. Cells* **2013**, 111, 57-65.
13. Zhao, Y.; Riemersma, C.; Pietra, F.; Koole, R.; de Mello Donegá, C.; Meijerink, A., High Temperature Luminescence Quenching of Colloidal Quantum Dots. *ACS Nano* **2012**.
14. Erwin, S. C.; Zu, L.; Haftel, M. I.; Efros, A. L.; Kennedy, T. A.; Norris, D. J., Doping semiconductor nanocrystals. *Nature* **2005**, 436, 91-4.
15. Sun, B. Q.; Yi, G. S.; Chen, D. P.; Zhou, Y. X.; Cheng, J., Synthesis and characterization of strongly fluorescent europium-doped calcium sulfide nanoparticles. *J. Mater. Chem.* **2002**, 12, 1194-1198.
16. Kumar, V.; Mishra, V.; Biggs, M. M.; Nagpure, I. M.; Ntwaeaborwa, O. M.; Terblans, J. J.; Swart, H. C., Electron beam induced green luminescence and degradation study of CaS:Ce nanocrystalline phosphors for FED applications. *Appl. Surf. Sci.* **2010**, 256, 1720-1724.
17. Archer, P. I.; Santangelo, S. A.; Gamelin, D. R., Direct Observation of sp−d Exchange Interactions in Colloidal Mn^{2+}- and Co^{2+}-Doped CdSe Quantum Dots. *Nano Lett.* **2007**, 7, 1037-1043.
18. Hanif, K. M.; Meulenberg, R. W.; Strouse, G. F., Magnetic Ordering in Doped Cd1-xCoxSe Diluted Magnetic Quantum Dots. *J. Am. Chem. Soc.* **2002**, 124, 11495-11502.
19. Mocatta, D.; Cohen, G.; Schattner, J.; Millo, O.; Rabani, E.; Banin, U., Heavily doped semiconductor nanocrystal quantum dots. *Science* **2011**, 332, 77-81.

20. Eilers, J.; Groeneveld, E.; de Mello Donegá, C.; Meijerink, A., Optical Properties of Mn-Doped ZnTe Magic Size Nanocrystals. *The Journal of Physical Chemistry Letters* **2012**, 3, 1663-1667.
21. Pradhan, N.; Goorskey, D.; Thessing, J.; Peng, X., An Alternative of CdSe Nanocrystal Emitters: Pure and Tunable Impurity Emissions in ZnSe Nanocrystals. *J. Am. Chem. Soc.* **2005**, 127, 17586-17587.
22. Chen, D.; Viswanatha, R.; Ong, G. L.; Xie, R.; Balasubramaninan, M.; Peng, X., Temperature Dependence of lementary Processes in Doping Semiconductor Nanocrystals. *J. Am. Chem. Soc.* **2009**, 131, 9333-9339.
23. Brennan, J. G.; Siegrist, T.; Carroll, P. J.; Stuczynski, S. M.; Brus, L. E.; Steigerwald, M. L., The preparation of large semiconductor clusters via the pyrolysis of a molecular precursor. *J. Am. Chem. Soc.* **1989**, 111, 4141-4143.
24. Pradhan, N.; Efrima, S., Single-precursor, one-pot versatile synthesis under near ambient conditions of tunable, single and dual band fluorescing metal sulfide nanoparticles. *J. Am. Chem. Soc.* **2003**, 125, 2050-1.
25. Pradhan, N.; Katz, B.; Efrima, S., Synthesis of High-Quality Metal Sulfide Nanoparticles from Alkyl Xanthate Single Precursors in Alkylamine Solvents. *The Journal of Physical Chemistry B* **2003**, 107, 13843-13854.
26. Trindade, T.; O'Brien, P., Synthesis of CdS and CdSe nanoparticles by thermolysis of diethyldithio-or diethyldiseleno-carbamates of cadmium. *J. Mater. Chem.* **1996**, 6, 343-347.
27. Zhao, Y.; Rabouw, F. T.; Donegá, C. d. M.; Meijerink, A.; van Walree, C. A., Single-source precursor synthesis of colloidal CaS and SrS nanocrystals. *Mater. Lett.* **2012**, 80, 75-77.
28. Purdy, A. P.; George, C. F., Anhydrous Dithiocarbamates. Potential Precursors to Alkaline Earth Sulfide Materials. *Main Group Chemistry* **1996**, 1, 229-240.
29. Regulacio, M. D.; Kar, S.; Zuniga, E.; Wang, G.; Dollahon, N. R.; Yee, G. T.; Stoll, S. L., Size-Dependent Magnetism of EuS Nanoparticles. *Chem. Mater.* **2008**, 20, 3368-3376.
30. Jung, Y. K.; Kim, J. I.; Lee, J.-K., Thermal Decomposition Mechanism of Single-Molecule Precursors Forming Metal Sulfide Nanoparticles. *J. Am. Chem. Soc.* **2009**, 132, 178-184.
31. Jia, D.; Wang, X.-j., Alkali earth sulfide phosphors doped with Eu^{2+} and Ce^{3+} for LEDs. *Optical Materials* **2007**, 30, 375-379.
32. Radovanovic, P. V.; Gamelin, D. R., Electronic absorption spectroscopy of cobalt ions in diluted magnetic semiconductor quantum dots: demonstration of an isocrystalline core/shell synthetic method. *J. Am. Chem. Soc.* **2001**, 123, 12207-14.
33. Yang, Y.; Chen, O.; Angerhofer, A.; Cao, Y. C., On doping CdS/ZnS core/shell nanocrystals with Mn. *J. Am. Chem. Soc.* **2008**, 130, 15649-61.
34. Okamoto, F.; Kato, K., Preparation and Cathodoluminescence of CaS: Ce and CaSrS: Ce Phosphors. *J. Electrochem. Soc.* **1983**, 130, 432.
35. Bachmann, V.; Ronda, C.; Meijerink, A., Temperature Quenching of Yellow Ce(3+) Luminescence in YAG:Ce. *Chem. Mater.* **2009**, 21, 2077-2084.
36. Kim, G. C.; Park, H. L.; Yun, S. I.; Moon, B. G., Solid Solubility Limit of Cerium in Cas-Ce-3+ Phosphor. *J. Mater. Sci. Lett.* **1986**, 5, 359-360.
37. Ravotti, F.*, et al.*, Time-resolved photoluminescence and optically stimulated luminescence measurements of picosecond-excited SrS : Ce,Sm phosphor. *J. Appl. Phys.* **2007**, 102.
38. Huttl, B.; Troppenz, U.; Velthaus, K. O.; Ronda, C. R.; Mauch, R. H., Luminescence properties of $SrS:Ce^{3+}$. *J. Appl. Phys.* **1995**, 78, 7282-7288.

39. Mirkovic, T.; Hines, M. A.; Nair, P. S.; Scholes, G. D., Single-Source Precursor Route for the Synthesis of EuS Nanocrystals. *Chem. Mater.* **2005**, 17, 3451-3456.
40. Malik, M. A.; Afzaal, M.; O'Brien, P., Precursor chemistry for main group elements in semiconducting materials. *Chem. Rev.* **2010**, 110, 4417-46.
41. Van Haecke, J. E.; Smet, P. F.; De Keyser, K.; Poelman, D., Single crystal CaS : Eu and SrS : Eu luminescent particles obtained by solvothermal synthesis. *J. Electrochem. Soc.* **2007**, 154, J278-J282.
42. Huxter, V. M.; Mirkovic, T.; Nair, P. S.; Scholes, G. D., Demonstration of Bulk Semiconductor Optical Properties in Processable Ag_2S and EuS Nanocrystalline Systems. *Adv. Mater.* **2008**, 20, 2439-2443.

CHAPTER 4

High Temperature Luminescence Quenching of Colloidal Quantum Dots

Abstract

Thermal quenching of quantum dot (QD) luminescence is important for application in luminescent devices. Systematic studies of the quenching behavior above 300 K are however lacking. Here, high temperature (300-500 K) luminescence studies are reported for highly efficient CdSe core-shell quantum dots (QDs), aimed at obtaining insight into temperature quenching of QD emission. Through thermal cycling ('yoyo') experiments for QDs in polymer matrices, reversible and irreversible luminescence quenching processes can be distinguished. For a variety of core-shell systems, reversible quenching is observed in a similar temperature range, between 100-180 °C. The irreversible quenching behavior varies between different systems. Mechanisms for thermal quenching are discussed.

4.1 Introduction

A high luminescence efficiency is an important property of colloidal Quantum Dots (QDs) and quantum yields higher than 90% have been reported for core-shell QDs.[1] High efficiencies are especially important for application of QDs as luminescent biolabels,[2] in QD lasers,[3] in spectral converters for warm white LEDs,[4, 5] electroluminescent devices,[6] and solar concentrators.[7] Luminescence efficiencies are strongly temperature dependent.[8] Extensive temperature dependent luminescence studies for colloidal QDs have been conducted at cryogenic temperatures (0.3-300K).[9-15] In this temperature region, interesting effects were observed, including a prolonged lifetime below 20 K related to bright-dark state splitting,[11, 16] thermally activated quenching due to surface defect states,[9, 10, 17] and temperature anti-quenching assigned to a phase transition in the capping layer.[14, 15] However, the luminescence properties of QDs above room temperature (RT) are hardly investigated and yet, for most applications in luminescent devices, the working temperature is higher than 300 K. An interesting example is the recent application of QDs as color converters in warm-white LEDs,[18] in which QDs serve as narrow band red emitters under excitation with blue light from a (In,Ga)N LED. The narrow emission bandwidth renders QDs superior to classical phosphors based on broad band emission from luminescent ions.[19] In high power LEDs for general lighting applications, the heat generated in the p-n junction and phosphor converter layer leads to temperatures as high as 150-200 °C in the layer applied on top of the blue diode.[20] To avoid these high temperatures, the QD phosphor layer can be placed in a more remote configuration. Still, temperatures in such a configuration are expected to be well above 50 °C due to heat dissipation of the QDs themselves (excess energy from converting the blue into red light). Clearly, the quenching of QD luminescence at elevated temperatures is relevant for application of QDs in luminescent devices and a better insight in the quenching behavior is needed.

Despite its importance, research on luminescence temperature quenching above RT is very limited for QDs. It is theoretically expected for a QD to have a very high luminescence quenching temperature (T_q). Three generally accepted mechanisms for thermal quenching involve thermally activated cross-over from the excited state to the ground state, multi-phonon relaxation and thermally activated photo-ionization. The first mechanism is generally depicted in a simple configurational coordinate diagram.[8, 21] The energy difference between the minimum of the excited state parabola and the crossing point between the excited state and ground state parabola is considered as activation energy for thermal quenching. For electronic transitions with a small Huang-Rhys factor *S* (*i.e.,* small electron-phonon coupling) this activation energy is high. For QD luminescence *S* has been shown to

be very small (~0.1-0.2) from the low relative intensity of the phonon side bands in single dot emission spectra.[22] For these small values of *S* temperature quenching is not expected.[21] Multi-phonon relaxation is a quenching process in which the energy gap between the excited state and the ground state is bridged by the simultaneous emission of phonons (21 vibrational quanta). If the gap can be bridged by 5 phonons, radiative and non-radiative decay compete.[8] For larger gaps radiative decay dominates and high quantum yields are possible. For QD emission in the red spectral region at least 50 vibrational quanta are required to bridge the gap due to the low Cd-Se vibrational energy and thus multi-phonon relaxation is not expected to play a role. Coupling with high-energy vibrations of the capping molecules can also result in fast non-radiative relaxation, and 5 or 6 high-energy (3000 cm^{-1}) C-H vibrations can bridge he energy gap. However, the temperature dependence for this (reversible) quenching process is negligible since thermal occupation of 3000 cm-1 vibrational mode is close to zero at 500 K. Clearly, this type of multi-phonon relaxation can not explain a strong temperature dependence below 300 °C. Finally, thermally activated photo-ionization can cause luminescence quenching by escape of a charge carrier from a luminescent center by thermally activated ionization. In traditional phosphors the process involves ionization from a localized dopant excited state to the host conduction band. For a QD it can be viewed as thermally activated escape of a charge carrier to a nearby trap state. Contrary to the other quenching mechanisms, which are intrinsic to the nature of the luminescent center, quenching processes involving traps or defects are not intrinsic and therefore the quenching temperature can vary for the same type of luminescent center depending on the nature and location of the defects or traps. Traps and defects have been used to explain luminescence quenching above 50 K for organically capped CdSe[11] and CdTe[10] QDs. For core-shell QDs, the quenching temperature increased to 200 K or above RT for CdSe/CdS/ZnS multi-shells[12] or CdSe/CdS nanorods.[23] These observations suggest that thermal quenching of QDs is related to carrier trapping in (surface) defect states and surface passivation through inorganic shells can suppress this process. The luminescence quenching behavior of core-shell QDs at elevated temperature has not yet been systematically studied and therefore the intrinsic quenching temperature of QDs remains to be determined. In this work, we focus on the high temperature region (300-500 K) and systematically study the thermal behavior of different types of highly efficient core-shell QDs, aiming at obtaining insight into the origin and mechanism of temperature quenching of colloidal QDs. To reduce the influence from surrounding media, the nanocrystal (NC) samples were immobilized and isolated in a cross-linked polymer matrix. We were able to distinguish the reversible and irreversible quenching effects by recording both photoluminescence

(PL) spectra and PL decay curves during successive heating and cooling cycles to increasingly higher temperatures (hereafter referred to as “yoyo” measurements).

4.2 Experimental Section

Synthesis of organically capped colloidal quantum dots (QDs) and nanorods. Colloidal CdSe QDs capped by trioctylphosphineoxide and hexadecylamine were synthesized following a procedure reported in the literature. [24] The diameter of the CdSe QDs was estimated from a sizing curve relating the first exciton peak energy with the nanocrystal size.[17] High quality CdSe/CdS/ZnS core-shell-shell QDs were prepared according to the one-pot multistage method reported by Lim *et al*.[25] The core diameter was 3.4 nm, and after overcoating with about 3 monolayers of CdS and 2 monolayers of ZnS, the particle size increased to 7 nm. CdSe/CdS dot core/rod shell nano-rods were synthesized following the procedure described by Manna *et al*, [26] using CdSe QDs with 3.2 nm in diameter as seeds. For CdS shell growth, octadecylphosphonic acid (ODPA) was used as the only capping ligand, as it results in better reaction control and favors the formation of nanorods. The nano-rods obtained are 21 nm long and 5.5 nm in diameter (aspect ratio: 4), as determined by TEM measurements. CdTe/CdSe core-shell QDs were synthesized as described by Zhang *et al.*[27] The CdTe cores were 3.4 nm in diameter and the final particle diameter increased to 6.1 nm after overcoating with the CdSe shell. Photoluminescence (PL) spectra and PL quantum yields were determined on an Edinburgh Instruments FL920 spectrofluorimeter equipped with an integrating sphere.

Incorporation of QDs or nanorods into polymer matrices. In order to immobilize and isolate the nanocrystal (NC) dispersion, CdSe QDs, CdSe/CdS/ZnS core-shell-shell QDs, CdSe/CdS dot core/ rod shell nanorods and CdTe/CdSe core/shell QDs were incorporated in crosslinked-Poly(methyl methacrylate) (cPMMA) or crosslinked-Poly(lauryl methacrylate) (cPLMA) matrix through a bulk polymerization method.[28] The procedure starts with washing the NCs twice by precipitation and centrifugation from a chloroform/acetone solution, followed by redispersion in chloroform. The clear NC solution was dried under vacuum to remove the solvent and the NCs were subsequently redispersed in a monomer mixture. The NC concentration in the matrix was kept low to avoid self-absorption. The monomer used for cPLMA (P(LMA-co-EGDMA)) matrix was 80 wt % lauryl methacrylate (LMA) and 20 wt % ethylene glycol dimethacrylate (EGDMA) as cross-linker; for cPMMA (P(MMA-co-EGDMA)) matrix, 97 wt % methyl methacrylate (MMA) and 3 wt %

EGDMA were used. For photo-initiated polymerization, 0.25 wt% photo-initiator, 2-hydroxy-2-methylpropiophenone (97%, Aldrich) was added to the solution and 2 ml of the reaction mixture was loaded into a glass tube and sealed under N_2 atmosphere. The glass tube was illuminated by two 360 nm UV lamps from both sides for 1h. The polymerization can also be thermally initialized. In that case, 0.3 wt % thermal initiator, AIBN (Janssen Chimica, re-crystallized from ethanol before use) were added into the monomer solution. The sealed tube was then embedded in water bath at 70°C for overnight curing.

Temperature dependent PL spectra and exciton lifetime measurements. For temperature dependent PL measurements, the sample sealed in a glass tube was immersed in a transparent paraffin oil bath in a Pyrex glass container. The bath was heated on a heating-plate and the temperature was controlled by a thermocouple immersed in the paraffin bath at the same height as the excitation laser beam. Photoluminescence (PL) spectra were measured under excitation at 406 nm by a PicoQuant PDL 800-B pulsed diode laser. The emitted light was collected through an optical fiber and dispersed in a 0.3 m monochromator (Acton Pro SP-300i, 150 lines/mm, blazed at 500 nm) and detected by a liquid nitrogen cooled Princeton Instruments CCD camera (1024 × 256 pixels). PL decay curves were recorded using a Picoquant time-correlated single-photon counting setup, with the same excitation scheme as described above, operating at a 2.5 MHz repetition rate. The emission was collected using another optical fiber and dispersed by a 0.1 m monochromator (1350 lines/mm blazed at 500 nm). A fast Hamamatsu photomultiplier tube (H5738P-01) and a Time Harp 200 time correlated photon counting card were used for detection and analysis. Care was taken to prevent effects of inter-pulse pile-up by keeping the photon count rate well below 5% of the laser repetition rate. At each temperature, first PL spectra were recorded after which a PL decay curve was obtained at the wavelength of emission maximum. The average lifetime values were calculated from the PL decay curve through a Gaussian distribution fitting in PicoQuant FluoFit 3.3.

4.3 Results and discussion

To gain understanding on the quenching behavior of QDs at elevated temperature, it is important to also monitor the role of the environment. To this effect, temperature dependent PL intensity and PL decay time measurements were performed on QDs in different matrices (liquid and solid). To investigate the influence of the medium, CdSe/CdS/ZnS core-shell-shell QD samples were dispersed in the high

boiling point solvent octadecene (ODE), or incorporated in solid polymer matrices: crosslinked- Poly(methyl methacrylate) (cPMMA) or crosslinked- Poly(lauryl methacrylate) (cPLMA). Both polymers show high transparency and limited deformation in the temperature range investigated (up to 220 °C). The temperature dependence of the emission intensity of the QDs was measured in the different matrices and is depicted in Figure 4.1. With increasing temperature, the PL intensity of the QDs in ODE solution drops significantly faster than that in the solid matrix, and it is almost gone above 150 °C (423 K), as clearly shown by the photographs taken during the experiment (Figure 4.1a). Along with the quenching of the excitonic QD emission, a red-shifted emission band appears which is assigned to defect emission. After cooling back down to RT, the intensity of the QD emission in ODE does not recover, indicating irreversible quenching. The lifetime measurements for the QD emission confirm the much lower quenching temperature (quenching above 70 °C) in solution than in solid matrices (quenching above 110 °C) (See Appendix Figure A4.1). The temperature dependent emission from

QD samples in cPLMA and cPMMA show a reproducible and similar behavior with higher T_q. Both the luminescence intensity and lifetime are partly recovered during the cooling process (detailed behavior in the solid matrices will be discussed later). These results show that T_q is strongly influenced by the surrounding medium. In an ODE solution at elevated temperatures the irreversible quenching is probably caused by surface states created by loss of capping ligands due to detachment. It is well-known that loss of capping ligands leads to surface states in the forbidden gap, which quench the luminescence of quantum dots.[29] These dynamic effects in solution occur at relatively low temperatures and obscure the observation of intrinsic quenching processes of QDs and make it necessary to incorporate the QDs in a solid matrix. In a solid matrix the passivating ligands cannot detach and leave the surface, thus preventing the irreversible quenching mechanism that dominates for QDs in solution at relatively low temperatures. For QDs dispersed in a solid environment (cPMMA or cPLMA), very similar and reproducible quenching behavior is observed. The higher T_q and partially reversible quenching behavior confirm that a solid matrix which immobilizes QDs is a good environment for studying temperature quenching of QD luminescence. The two polymer materials have a very different glass transition temperature (T_g) and stiffness (without crosslinking, PMMA has a T_g >100 °C while PLMA has a T_g <-65 °C).[30] The similarity of the luminescence quenching indicates that the physical properties of the polymer matrices are not very important.

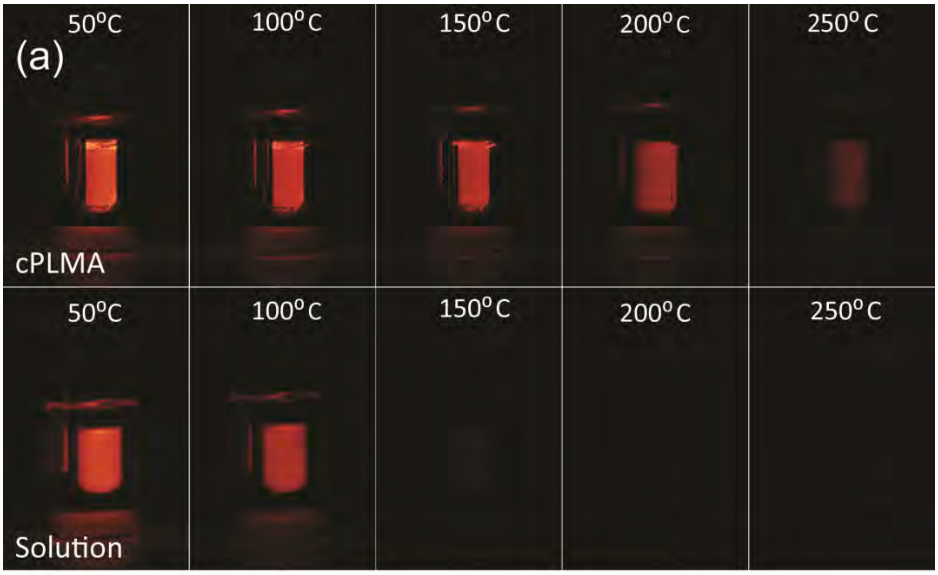

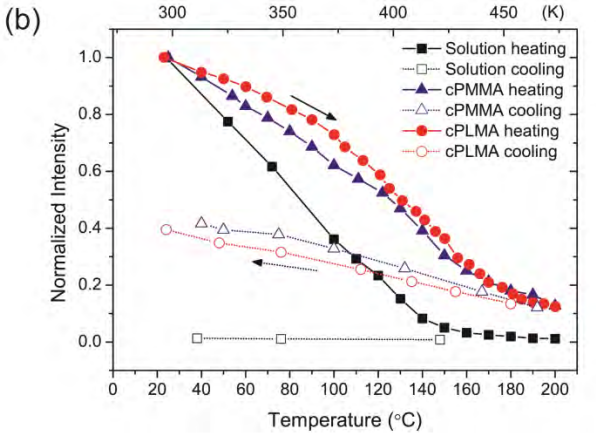

Figure 4.1. Temperature dependent photoluminescence (PL) of CdSe/CdS/ZnS core-shell-shell QDs measured in various environments. (a) Photographs taken under UV irradiation at the temperatures indicated. The QDs are incorporated in crosslinked-PLMA (upper row), or dispersed in ODE solution (bottom row), and sealed in glass tubes under N_2. (b) The temperature dependent PL intensity of CdSe/CdS/ZnS QDs in ODE solution (black squares), crosslinked PMMA (blue triangles) and crosslinked PLMA (red circles). The solid symbols mark the heating stages and the open symbols the cooling stages.

To better understand the thermal quenching processes it is important to distinguish between reversible and irreversible quenching. One way to achieve this is to study the reversibility of both the decrease of the luminescence intensity and radiative lifetime upon heating and the recovery upon subsequent cooling. Irreversible quenching is related to a change in the QD structure and is not intrinsic quenching, while the reversible quenching can originate from the QD structure itself and be related to intrinsic quenching processes. To study the quenching processes, we performed "yoyo" measurements on various types of QDs, including organically capped CdSe QDs, CdSe/CdS/ZnS core-shell-shell QDs, CdSe/CdS dot core/rod shell nanorods and CdTe/CdSe core/shell QDs. The CdSe core sizes of the structures are similar (~3.0 to 3.4 nm) and the luminescence quantum yields are high (60-70 %, except for the bare QDs which have a lower QY). The characteristics of the samples are given in the Table 4.1. By monitoring the luminescence intensity and life time for successive heating and cooling cycles, we are able to differentiate between irreversible and reversible quenching processes and determine the temperature range for quenching.

Table 4.1. Characteristics of the colloidal nanocrystals used in the experiments. The core sizes have been determined from the position of the first absorption peak and known sizing curves.[17] Total particle sizes are based on analysis of TEM images of multiple NCs. The PL wavelength and quantum yield are measured by using the set-up described in the main text.

Sample name	Core diameter (nm)	Particle size[a] (nm)	PL wavelength (nm)	Quantum Yield (%)
CdSe QDs	3.4	3.4	573	28
CdSe/CdS/ZnS QDs	3.4	7.0	610	64
CdSe/CdS nanorods	3.2	5.5/21.1	604	72
CdTe/CdSe QDs	3.0	6.1	614	59

a. For spherical QDs, the particle sizes are given as average diameter. For nanorods, the average diameter and length are given.

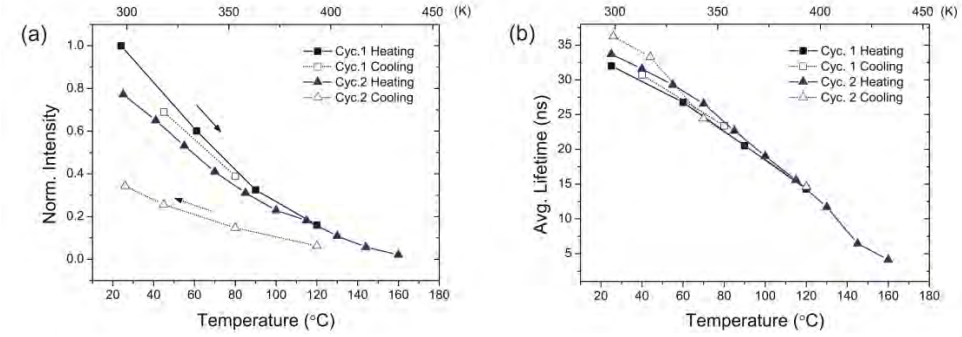

Figure 4.2. The temperature dependent (a) intensity and (b) average lifetime of organically capped CdSe QDs incorporated in cPMMA. Data from the first thermal cycle (25-120°C) are represented by squares, while triangles indicate the second cycle (25-160°C). Solid symbols refer to the heating process, while cooling process is indicated by open symbols.

The initial “yoyo” measurements are done on CdSe QDs embedded in cPMMA. In Figure 4.2, the PL intensity and life time are plotted as a function of temperature for subsequent heating and cooling cycles. Upon raising the temperature, both the intensity and average lifetime decrease but the decrease in intensity is more pronounced. This result is consistent with previous observations at lower temperatures,[9, 11, 12] and can be regarded as the higher temperature extension of the quenching process which starts below RT. The cooling measurements reveal that the decrease in lifetime is completely reversible while the PL intensity recovers only partly. There is a 20% permanent loss of intensity after heating up to 120 °C and this loss increases to 60% after heating to 160 °C in the second cycle. It indicates that part of the dots turn permanently ‘dark’ during the heating process. The PL lifetime is biased towards the remaining ‘bright’ QDs and the complete recovery shows that these are reversibly quenched at high temperatures.

For practical applications the thermal quenching of CdSe/CdS/ZnS core-multishell QDs is important since this type of dots can be synthesized with high quantum efficiency and stability, and is the most commonly used QD-structure in applications (biolabels,[2] QD-LEDs[6] and color converters[4, 25]). We did yoyo experiments in three temperature regions: 25-100 °C (I), 100-150 °C (II) and 150-210 °C (III). The results for the PL intensity and lifetime measurements are presented in Figure 4.4a. In region I, up to 100 °C, the total PL intensity decreases while the

average lifetime increases slightly. Both changes are fully reversible. These observations show that the PL intensity is not always a good indicator to study the thermal quenching of QDs. The overall intensity may decrease due to complete quenching of a fraction of the QDs. The exciton lifetime probes the remaining bright fraction of QDs and is thus a better indicator for intrinsic quenching mechanisms in QDs. The slight increase in lifetime can be explained by thermally activated delocalization of the electron wave function from the CdSe core to the CdS shell due to the shallow offset between the conduction bands of CdSe and CdS. Further delocalization of the electron wave function reduces the wave function overlap with the hole and has been suggested as explanation for the increase in life time.[23] An alternative explanation is thermal population of higher energy dark exciton states (for which emission to the ground state is forbidden). The exciton energy level structure of CdSe QDs has been intensively studied. The shortening in lifetime between 4 and 50 K can be explained by thermal population of the ($\pm 1^L$) bright exciton fine-structure state situated just above the lowest energy dark exciton state (± 2).[11, 16] Another optically inactive excited state (0^L) is situated above the bright state ($\pm 1^L$) (20 meV higher in energy for 3.1nm CdSe QDs).[31] With increasing temperature, this dark state is thermally populated and this can also explain the observed lengthening of the lifetime between 20 and 100 °C. The observed redshift of the emission can also contribute to the increase of the life time, but based on size dependent radiative decay rates, only a ~1.4 ns increase is expected for the observed 10 nm shift around 600 nm.[17] The absence of life time shortening gives evidence that there is no intrinsic quenching up to 100 °C.

A strong decrease in both the PL intensity and the exciton lifetime occurs between 100 and 150 °C (region II). When the CdSe/CdS/ZnS QDs were heated above 100 °C, a steeper decrease in intensity is observed. This change is accompanied by a decrease of lifetime which competes with the lifetime increase process observed in region I. To illustrate the initial lengthening followed by a shortening of the exciton lifetime, several PL decay curves are presented in Figure 4.4a, for different temperatures. The decrease of lifetime starting above 100 °C is a direct evidence for TQ. The changes of the intensity and lifetime are not totally reversible after heating to 150 °C. Upon cooling down to 100 °C, there is also permanent loss of intensity and shortening of lifetime giving evidence for an irreversible structural change in part of the QD ensemble.

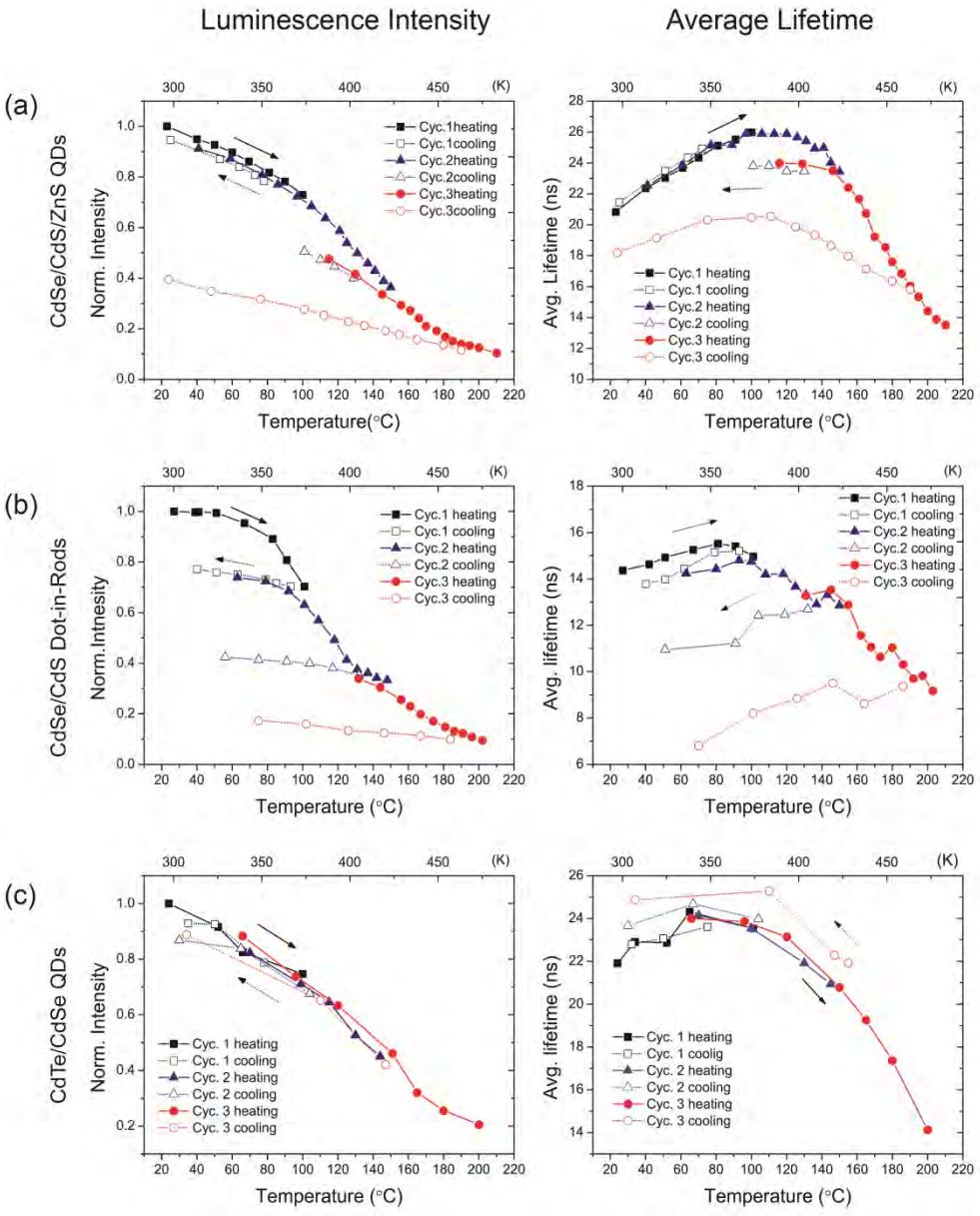

Figure 4.3. The temperature dependent PL intensity (left column) and average luminescence lifetime (right column) of (a) CdSe/CdS/ZnS QDs incorporated in cPLMA, (b) CdSe/CdS nanorods incorporated in cPLMA and (c) CdTe/CdSe incorporated in cPMMA. Squares mark the first thermal cycle (20-100°C), triangles the second cycle (20-150°C), and the circles the third cycle (20-210°C). The solid symbols refer to heating and open symbols to cooling.

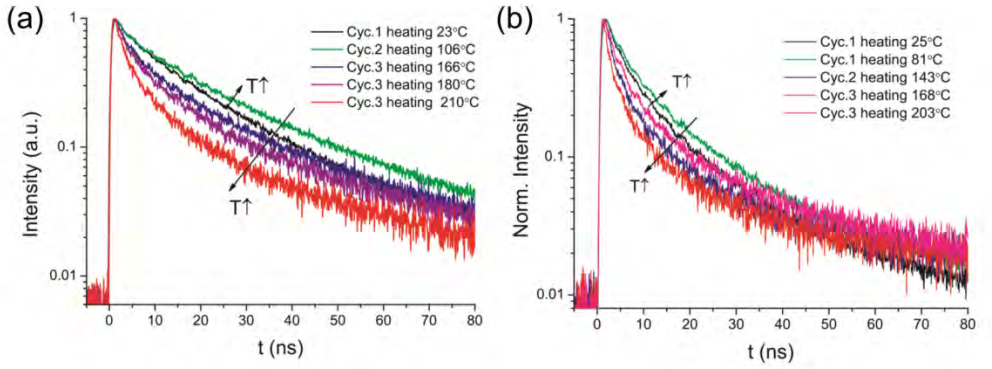

Figure 4.4. PL decay curves of (a) CdSe/CdS/ZnS core-shell-shell QDs in cPMMA and (b) CdSe/CdS nanorods incorporated in cPLMA for excitation at 406 nm and emission at ~600 nm at the temperatures indicated.

In the last cycle, with heating over 150 °C, the decay of the intensity and lifetime follows the same trend as the decrease in region II until 210 °C, where the intensity is less than 10% of the initial value. During cooling there is a partial recovery for both intensity and lifetime. In this region, the TQ quenching process clearly contains an irreversible and a reversible part. There is also a continuous red shift of the PL peak with increasing temperature which is consistent with low temperature studies where the shift in bandgap is described by the Varshni equation.[9, 12] The shift is totally reversible (Appendix Figure A4.2).

A third system that was investigated in the present work is the CdSe/CdS dot core/rod shell nanorods. The unique optical properties of these nanostructures include a high QY, polarized absorption and emission, and suppression of blinking and Auger recombination. Based on these characteristics they have been proposed as materials for opto-electronic devices.[23] We performed yoyo cycling experiments in three temperature regions for CdSe/CdS dot core/rod shell nanorods (core diameter: 3.2 nm, rod length: ~20 nm) embedded in cPLMA. The temperature dependent PL intensity and average lifetime are plotted in Figure 4.3b. Up to 80 °C the intensity is constant while the lifetime shows a small increase upon heating. This result is consistent with measurements at lower temperatures,[23] where between 70 to 300 K an increase of lifetime and a constant intensity were reported. Upon raising the temperature above 80 °C the intensity decreases and the lifetime becomes shorter (Figure 4.4b). These changes are irreversible as both the intensity and lifetime do not recover after cooling down. In the second and third cycle, where the nanorods were heated up to 150 °C and 200 °C, a similar trend is

observed: an irreversible decrease of intensity and lifetime occurs with increasing temperature. At 200 °C the intensity has dropped below 10% of the initial value and does hardly recover upon subsequent cooling (Figure 4.3b). During heating up to high temperatures, a broad defect related emission band also appears at longer wavelength.

The final nanostructures investigated are CdTe/CdSe core-shell QDs. Depending on the thickness of the core and shell, a type-II band alignment can be realized for the CdTe/CdSe system,[32] but for the presently studied system (3 nm core, 1.3 nm shell) the short luminescence life time (~26 ns at RT) indicates that there is strong delocalization of the electron over the heteronanostructure (*i.e.*, the QDs are still in the type-$I^{1/2}$ or "*quasi*" Type-II localization regime[32, 33]). The results of the 'yoyo' measurements on CdTe/CdSe QDs embedded in cPMMA are presented in Figure 4.3c for three temperature ranges (RT-100 °C, 100-150 °C and 150-200 °C). Similar to the observations for other systems, in all three temperature regions the intensity decreases with the strongest decrease between 100 and 160 °C. The behavior of the lifetime is also analogous to other systems: a slight increase between RT-80 °C is followed by a decrease above 100 °C. However, different from the systems described above, both the PL intensity and the exciton lifetime recover fully upon cooling, indicating that the temperature quenching in the CdTe/CdSe core/shell QDs is totally reversible up to 200 °C. This observation is important. It reveals that irreversible quenching is not necessarily present in every QD structure and that depending on the band structure and/or core-shell heterointerface, the irreversible formation of surface/interface or defect states that quench the luminescence can be avoided.

The thermal quenching studies for the luminescence of four different QD systems show several general trends. A decrease in intensity is observed starting above RT. Initially the decrease is slow and a more rapid drop in intensity occurs for all systems studied between 100 and 150 °C. For the core-shell structures, the luminescence lifetime shows a slight increase between RT and ~80 °C, while for organically capped CdSe QDs no increase in luminescence lifetime is observed. Between 100 and 180 °C a clear shortening of the lifetime is observed for all QD structures, along with a strong decrease in emission intensity. The reversibility of the drop in emission intensity and reduction of the life time in heating/cooling cycles varies: for CdTe/CdSe QDs the intensity and life time fully recover upon cooling, while for CdSe cores in CdS nanorods the loss in intensity is mostly permanent. For the CdSe QDs and CdSe/CdS/ZnS core-shell-shell QD structures, both reversible and irreversible quenching contribute. In earlier work on luminescence quenching below RT, luminescence quenching is usually ascribed to

thermally activated carrier trapping.[11] Surface states, defects or impurities in the immediate surroundings of the QD can act as trapping centers and carrier trapping is followed by non-radiative recombination or red-shifted defect related emission. The present observations for highly efficient core-shell structures with RT quantum yields of 60-70%, show an onset for temperature quenching around 100 °C. This temperature is significantly higher than that for organically capped CdSe QDs which are already partly quenched at RT. This clearly demonstrates the importance of inorganic shell coating for confining the wave functions, eliminating the surface defects states and suppressing the surface trapping states, hence improving QD's high temperature optical performance.

The yoyo measurements reveal details and differences for the thermal behavior of the core-shell structures, giving insight into the origin of thermal quenching. Two different thermal quenching processes can be distinguished: irreversible and reversible quenching. In Figure 4.5, different quenching mechanisms are schematically depicted. Since the irreversible quenching behavior varies between different structures and complicates the interpretation, we consider it first. For CdSe/CdS/ZnS QDs and CdSe cores embedded in CdS nanorods, the average PL lifetime and PL intensity start to decrease sharply, after heating above ~100 °C. The PL intensity drop and lifetime shortening is only partly reversible. After heating to 210 °C and cooling down to RT, there is a 60% permanent loss of intensity for CdSe/CdS/ZnS QDs and over 80% for CdSe cores embedded in CdS nanorods. The most likely origin of this irreversible quenching is the formation of surface states or defects related to an irreversible structural change (Figure 4.5c). The thermally induced irreversible structural changes are possibly due to the lattice mismatch between core and shell materials, which generate interfacial strain and favors dislocation of atoms. Upon raising the temperature, the difference in expansion of core and shell materials and increased mobility of the atoms may result in the formation of temporary or permanent trapping centers. One may argue that structural changes at these temperatures is unexpected since the synthesis temperatures for the QDs are much higher, typically between 200 and 350 °C, and yet high QYs are realized. However, the synthesis of core-shell QDs (or nanorods) is carried out under a high chemical potential environment with a large excess of surrounding ligands and precursors, resulting in high quality QDs.[33] It is known that after long time annealing at elevated temperature in the reaction mixture, the QY decreases[24] and the shape of QDs and nanorods may also change upon heating.[33, 34] Therefore, local structural changes for core-shell dots (or rods) can be expected during thermal cycling. Surface states and defects created in the shell material may also quench the luminescence due to delocalization of charge carriers over the shell. The strongly irreversible quenching observed for the CdSe/CdS

nanorods may be related to the large surface area of the rods which increases the probability for the creation of a defect or surface state in the CdS nanorod which can trap the delocalized charge carrier.

From a practical point of view, the irreversible quenching can be a crucial limiting factor for applications of core-shell nanostructures at elevated temperatures. Interestingly, the results on CdTe/CdSe core/shell QDs indicate that the irreversible quenching process is absent in this system. During the yoyo measurements in the whole temperature region up to 200 °C, the intensity and lifetime variation is totally reversible. Interfacial diffusion between Se and Te may reduce the interfacial strain. Chin *et al.* [35] previously reported a slight anti-quenching behavior in the range of 300-360 K for CdTe/CdSe core-shell nanostructures with core size and emission wavelength comparable to those investigated here. This indicates that, depending on the sample, the QY may even increase due to thermal annealing effects. The results demonstrate that CdTe/CdSe heteronanocrystals are interesting materials for high temperature lighting applications.

Reversible luminescence quenching may be related to intrinsic quenching. Traditional luminescent materials applied in lighting show fully reversible temperature quenching due to thermally activated cross-over from the excited state to the ground state (Figure 4.5a) or multi-phonon relaxation (Figure 4.5b), as discussed above. The quenching is an intrinsic and characteristic property of the luminescent species. For the core-shell QDs reversible quenching is observed between 100 and 180 °C and is most reliably observed in the temperature dependence of the luminescence decay time. The temperature range is similar for the different core-shell structures investigated. It is unlikely that the quenching is due to one of the two traditional reversible quenching processes. The electron-phonon coupling is weak for excitonic emission and is reflected by a small Huang-Rhys parameter *S* (for CdSe *S* is about 0.1-0.2).[36] In the configurational coordinate diagram the off-set in equilibrium distance between the ground state and excited state parabola is very small. Hence the crossing point is at very high energies and for systems with a Huang-Rhys parameter below 1 no thermal quenching due to thermally activated cross-over has been observed.

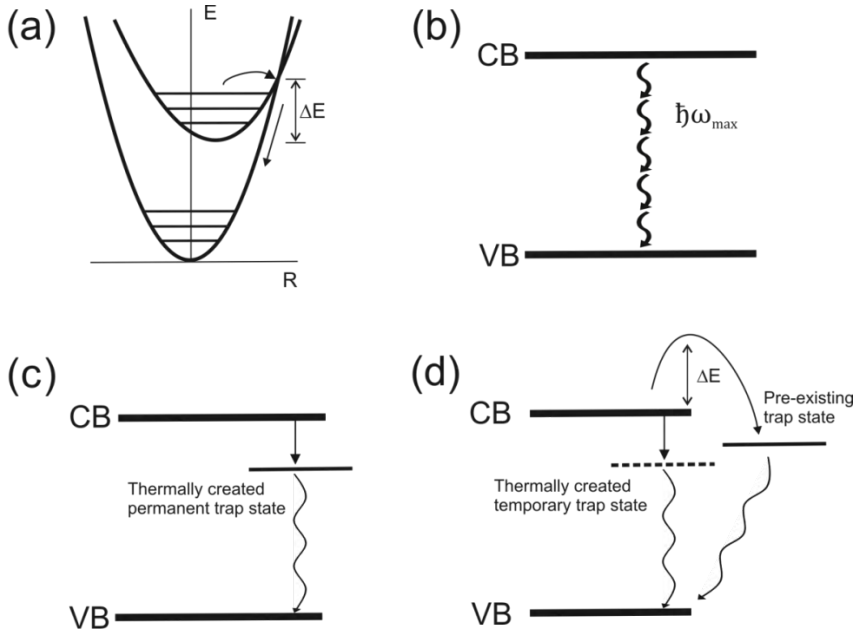

Figure 4.5. Schematic representation of luminescence quenching mechanisms. Two traditional models for intrinsic quenching of luminescence are based on (a) thermally activated cross-over, and (b) multi-phonon relaxation. Quenching related to traps are shown for (c) irreversible quenching, which is related to thermally created permanent trap states, and (d) reversible quenching, which is related to thermally created temporary trap states or thermally activated trapping processes involving pre-existing trap states.

A quenching mechanism for luminescent species characterized by a small parabola offset is multi-phonon relaxation, where the energy gap is bridged by the simultaneous emission of phonons[8, 37] (Figure 4.5b). The non-radiative multi-phonon relaxation rate decreases exponentially with the number of phonons *p* (with $p=\Delta E/\hbar\omega_{max}$, where ΔE is the energy gap and $\hbar\omega_{max}$ is the maximum phonon energy). Multi-phonon relaxation can compete with radiative decay if the energy gap can be bridged by ~5 phonons. If more than 5 phonons are required, radiative decay dominates while for less than 5 phonons non-radiative decay dominates.[21] For the presently studied systems with ~3-3.5 nm CdSe cores the bandgap (ΔE) is about 2 eV and the LO phonon energies for CdSe are ~25meV, thus *p*=80 which indicates that the gap is too large for effective multi-phonon relaxation. Coupling with high energy vibrations of surrounding ligands (*e.g.*, C-H or N-H stretching

vibrations of ~0.4 eV) can give rise to multi-phonon relaxation (p=5), but cannot explain the temperature dependence. The multi-phonon relaxation rate is only enhanced at higher temperatures if the phonon occupation number or Bose-Einstein factor n ($n = 1/(e^{\hbar\omega/kT})-1$) increases, which can be viewed as stimulated multi-phonon emission in the presence of 'phonon field', similar to stimulated photon emission.[21, 38] For high energy 0.4 eV vibrations there is no thermal population (n close to 0) below 1000 K and multi-phonon relaxation can therefore not explain the observed temperature dependence. The large distance to the high energy ligand vibrations, especially for core-shell systems where the ligands are on the surface of the shell, also reduces the coupling strength (which scales with R^{-6}) and makes multi-phonon relaxation highly unlikely.

As discussed above, the two traditional models for intrinsic quenching of luminescent materials cannot explain the reversible quenching of luminescence in QDs. An alternative explanation is thermally activated creation of surface states or defects which trap the charge carriers (Figure 4.5d), similar to the process explaining the irreversible quenching. However, upon cooling the thermally created traps relax back and the original configuration with high quantum yields is restored. The creation of trap states is induced by ion mobility at elevated temperatures. Ion exchange experiments on CdSe and PbSe QDs at temperatures between RT and 100 °C show that the ions in these semiconductors QDs are mobile at relatively low temperatures,[39, 40] and thus the creation of surface (interface) states and defects by local changes in the QD structure at temperatures between 100 and 200 °C can be due to displacement of (surface) atoms. The temperature range in which reversible quenching takes place is similar, between 100 and 180 °C, for the different types of 3-3.5 nm CdSe core-shell structures, which is consistent with the formation of defects due to increased ionic mobility in the CdSe QDs at similar elevated temperatures. For the CdTe/CdSe QDs anion disordering at the core/shell interface facilitates relaxation upon cooling. An Arrhenius fit describes the observed temperature dependence of the luminescence intensity well and yields a thermal activation energy of ~0.3-0.4 eV (Appendix Figure A4.3 and Table A4.1). This activation energy is about 10 times larger than activation energies between 10 and 70 meV reported for luminescence temperature quenching in CdSe in the low temperature regime. [9, 41, 42] A similar activation energy (0.24 eV) was recently reported as activation energy for enhanced blinking in excitation wavelength dependent blinking studies.[43] For the CdSe/CdS/ZnS core-shell-shell QDs and CdSe cores embedded in CdS nanorods the thermally induced mobility gives rise to the formation of trap states which do not relax back upon cooling. Finally, part of the reversible quenching may also be related to thermally activated carrier escape to pre-existing trap states. This mechanism is usually invoked to explain low tempera-

ture quenching processes (below 200 K) where the creation of trap states is unlikely. Thermally activated escape of charge carriers can explain the observed decrease in emission intensity. Naturally, this process is fully reversible and the high quantum yield is restored upon cooling. For the presently observed high temperature quenching thermally activated carrier escape with high activation energy may also contribute to the observed reversible quenching.

The present observations have revealed a universal quenching behavior for 3-3.5 nm CdSe QDs above 100 °C with contributions from reversible and irreversible processes. Further research is required to obtain deeper insight in the exact mechanism for quenching. Different types (*e.g.*, InP and PbSe) and different sizes of core-shell structures need to be investigated to relate the observed trends in the quenching behavior to material properties and particle size. Electron paramagnetic resonance (with and without illumination) may be used to monitor the thermally induced creation of paramagnetic defects. Based on insights obtained from these studies QDs with higher quenching temperatures may be realized, which is especially important in optical applications where the temperature is raised above 100 °C.

4.3 Conclusions

In conclusion, we have investigated the temperature dependent photoluminescence intensity and emission lifetime of three representative core-shell CdSe QDs systems at high temperatures (RT-200 °C). Different types of highly efficient (60-70 % QY) CdSe QD systems emitting in the red spectral region and incorporated in a cross-linked polymer matrix were studied. Thermal cycling ('yoyo') experiments make it possible to differentiate between reversible and irreversible luminescence quenching processes. Irreversible quenching originates from thermally induced permanent structural changes, giving rise to trap states, and was found in CdSe/CdS/ZnS core-shell-shell QDs and CdSe/CdSe dot core/rod shell nanorods, but not in CdTe/CdSe core/shell QDs. Reversible quenching was observed to contribute to luminescence quenching for QDs in all three core-shell systems in a similar temperature range (quenching between 100-180 °C). Reversible quenching is explained either by thermally activated escape of carriers to existing (surface) trap states and/or the thermally activated creation of trap states which relax upon cooling. The quenching temperature for QD emission estimated based on classical models for luminescence quenching (thermally activated cross-over or multi-phonon relaxation) is much higher than 200 °C and cannot explain the

observed quenching behavior. The results have important implications for application of QDs in optical devices (*e.g.* warm white LEDs, electroluminescent devices and QD-lasers) with operating temperatures above 100°C. Further studies on different QD systems are required to gain further insight in the quenching mechanism and to find efficient QDs with higher luminescence quenching temperatures.

References

1. Coe-Sullivan, S., Quantum dot developments. *Nat. Photonics* **2009**, 3, 315-316.
2. Skajaa, T.*, et al.*, Quantum Dot and Cy5.5 Labeled Nanoparticles to Investigate Lipoprotein Biointeractions via Forster Resonance Energy Transfer. *Nano Lett.* **2010**, 10, 5131–5138.
3. Klimov, V. I.*, et al.*, Optical gain and stimulated emission in nanocrystal quantum dots. *Science* **2000**, 290, 314-317.
4. Jang, E.; Jun, S.; Jang, H.; Lim, J.; Kim, B.; Kim, Y., White-light-emitting diodes with quantum dot color converters for display backlights. *Adv. Mater.* **2010**, 22, 3076-80.
5. Lee, J.; Sundar, V. C.; Heine, J. R.; Bawendi, M. G.; Jensen, K. F., Full color emission from II-VI semiconductor quantum dot-polymer composites (vol 15, pg 1104, 2000). *Adv. Mater.* **2000**, 12, 1311-1311.
6. Cho, K.-S.*, et al.*, High-performance crosslinked colloidal quantum-dot light-emitting diodes. *Nat Photon* **2009**, 3, 341-345.
7. Bomm, J.*, et al.*, Fabrication and full characterization of state-of-the-art quantum dot luminescent solar concentrators. *Sol. Energy Mater. Sol. Cells* **2011**, 95, 2087-2094.
8. Blasse, G.; Grabmaier, B. C., *Luminescent Materials*. Springer-Verlag: **1994**.
9. Valerini, D.; Cretí, A.; Lomascolo, M.; Manna, L.; Cingolani, R.; Anni, M., Temperature dependence of the photoluminescence properties of colloidal CdSe⁄ZnS core/shell quantum dots embedded in a polystyrene matrix. *Physical Review B* **2005**, 71, 235409.
10. Morello, G.; De Giorgi, M.; Kudera, S.; Manna, L.; Cingolani, R.; Anni, M., Temperature and Size Dependence of Nonradiative Relaxation and Exciton−Phonon Coupling in Colloidal CdTe Quantum Dots. *The Journal of Physical Chemistry C* **2007**, 111, 5846-5849.
11. Donega, C. D.; Bode, M.; Meijerink, A., Size- and temperature-dependence of exciton lifetimes in CdSe quantum dots. *Physical Review B* **2006**, 74, 9.
12. Jing, P.*, et al.*, Temperature-Dependent Photoluminescence of CdSe-Core CdS/CdZnS/ZnS-Multishell Quantum Dots. *The Journal of Physical Chemistry C* **2009**, 113, 13545-13550.
13. Jones, M.; Lo, S. S.; Scholes, G. D., Quantitative modeling of the role of surface traps in CdSe/CdS/ZnS nanocrystal photoluminescence decay dynamics. *Proceedings of the National Academy of Sciences* **2009**, 106, 3011-3016.
14. Wuister, S. F.; van Houselt, A.; de Mello Donega, C.; Vanmaekelbergh, D.; Meijerink, A., Temperature antiquenching of the luminescence from capped CdSe quantum dots. *Angew. Chem. Int. Ed. Engl.* **2004**, 43, 3029-33.

15. Wuister, S. F.; de Mello Donega, C.; Meijerink, A., Luminescence temperature antiquenching of water-soluble CdTe quantum dots: role of the solvent. *J. Am. Chem. Soc.* **2004**, 126, 10397-402.
16. Crooker, S. A.; Barrick, T.; Hollingsworth, J. A.; Klimov, V. I., Multiple temperature regimes of radiative decay in CdSe nanocrystal quantum dots: Intrinsic limits to the dark-exciton lifetime. *Appl. Phys. Lett.* **2003**, 82, 2793-2795.
17. Donega, C. D.; Koole, R., Size Dependence of the Spontaneous Emission Rate and Absorption Cross Section of CdSe and CdTe Quantum Dots. *J. Phys. Chem. C* **2009**, 113, 6511-6520.
18. Nizamoglu, S.; Erdem, T.; Sun, X. W.; Demir, H. V., Warm-white light-emitting diodes integrated with colloidal quantum dots for high luminous efficacy and color rendering. *Opt. Lett.* **2010**, 35, 3372-4.
19. Lin, C. C.; Liu, R.-S., Advances in Phosphors for Light-emitting Diodes. *The Journal of Physical Chemistry Letters* **2011**, 2, 1268-1277.
20. Bachmann, V.; Ronda, C.; Meijerink, A., Temperature Quenching of Yellow Ce(3+) Luminescence in YAG:Ce. *Chem. Mater.* **2009**, 21, 2077-2084.
21. Henderson, B.; Imbusch, G. F., *Optical Spectroscopy of Inorganic Solids*. Oxford University Press: **2006**.
22. Empedocles, S. A.; Norris, D. J.; Bawendi, M. G., Photoluminescence spectroscopy of single CdSe nanocrystallite quantum dots. *Phys. Rev. Lett.* **1996**, 77, 3873-3876.
23. Rainò, G.; Stöferle, T.; Moreels, I.; Gomes, R.; Kamal, J. S.; Hens, Z.; Mahrt, R. F., Probing the Wave Function Delocalization in CdSe/CdS Dot-in-Rod Nanocrystals by Time- and Temperature-Resolved Spectroscopy. *ACS Nano* **2011**, 5, 4031-4036.
24. de Mello Donega, C.; Hickey, S. G.; Wuister, S. F.; Vanmaekelbergh, D.; Meijerink, A., Single-Step Synthesis to Control the Photoluminescence Quantum Yield and Size Dispersion of CdSe Nanocrystals. *The Journal of Physical Chemistry B* **2003**, 107, 489-496.
25. Lim, J.; Jun, S.; Jang, E.; Baik, H.; Kim, H.; Cho, J., Preparation of highly luminescent nanocrystals and their application to light-emitting diodes. *Adv. Mater.* **2007**, 19, 1927-+.
26. Baranov, D*., et al.*, Assembly of Colloidal Semiconductor Nanorods in Solution by Depletion Attraction. *Nano Lett.* **2010**, 10, 743-749.
27. Zhang, W.; Chen, G.; Wang, J.; Ye, B. C.; Zhong, X., Design and synthesis of highly luminescent near-infrared-emitting water-soluble CdTe/CdSe/ZnS core/shell/shell quantum dots. *Inorg. Chem.* **2009**, 48, 9723-31.
28. Bomm, J.; Buchtemann, A.; Fiore, A.; Manna, L.; Nelson, J. H.; Hill, D.; van Sark, W. G., Fabrication and spectroscopic studies on highly luminescent CdSe/CdS nanorod polymer composites. *Beilstein J Nanotechnol* **2010**, 1, 94-100.
29. Bullen, C.; Mulvaney, P., The Effects of Chemisorption on the Luminescence of CdSe Quantum Dots. *Langmuir* **2006**, 22, 3007-3013.
30. Rogers, S.; Mandelkern, L., Glass Transitions of the Poly-(n-Alkyl Methacrylates). *The Journal of Physical Chemistry* **1957**, 61, 985-991.
31. Efros, A. L.; Rosen, M.; Kuno, M.; Nirmal, M.; Norris, D. J.; Bawendi, M., Band-edge exciton in quantum dots of semiconductors with a degenerate valence band: Dark and bright exciton states. *Physical Review B* **1996**, 54, 4843-4856.
32. de Mello Donegá, C., Formation of nanoscale spatially indirect excitons: Evolution of the type-II optical character of CdTe/CdSe heteronanocrystals. *Physical Review B* **2010**, 81, 165303.
33. Donega, C. d. M., Synthesis and properties of colloidal heteronanocrystals. *Chem. Soc. Rev.* **2011**, 40, 1512-1546.

34. Grodzinska, D.; Pietra, F.; van Huis, M. A.; Vanmaekelbergh, D.; Donega, C. D., Thermally induced atomic reconstruction of PbSe/CdSe core/shell quantum dots into PbSe/CdSe bi-hemisphere hetero-nanocrystals. *J. Mater. Chem.* **2011**, 21, 11556-11565.
35. Chin, P. T. K.; de Mello Donegá, C.; van Bavel, S. S.; Meskers, S. C. J.; Sommerdijk, N. A. J. M.; Janssen, R. A. J., Highly Luminescent CdTe/CdSe Colloidal Heteronanocrystals with Temperature-Dependent Emission Color. *J. Am. Chem. Soc.* **2007**, 129, 14880-14886.
36. Norris, D. J.; Efros, A. L.; Rosen, M.; Bawendi, M. G., Size dependence of exciton fine structure in CdSe quantum dots. *Physical Review B* **1996**, 53, 16347-16354.
37. van Dijk, J. M. F.; Schuurmans, M. F. H., On the nonradiative and radiative decay rates and a modified exponential energy gap law for 4f--4f transitions in rare-earth ions. *The Journal of Chemical Physics* **1983**, 78, 5317-5323.
38. Tilstra, L. G.; Arts, A. F. M.; de Wijn, H. W., Optically excited ruby as a saser: Experiment and theory. *Physical Review B* **2007**, 76, 024302.
39. Camargo, P. H.; Lee, Y. H.; Jeong, U.; Zou, Z.; Xia, Y., Cation exchange: a simple and versatile route to inorganic colloidal spheres with the same size but different compositions and properties. *Langmuir* **2007**, 23, 2985-92.
40. Miszta, K.; Dorfs, D.; Genovese, A.; Kim, M. R.; Manna, L., Cation Exchange Reactions in Colloidal Branched Nanocrystals. *ACS Nano* **2011**, 5, 7176-7183.
41. Kim, J. C.; Rho, H.; Smith, L. M.; Jackson, H. E.; Lee, S.; Dobrowolska, M.; Furdyna, J. K., Temperature-dependent micro-photoluminescence of individual CdSe self-assembled quantum dots. *Appl. Phys. Lett.* **1999**, 75, 214-216.
42. Bhattacharyya, S.; Estrin, Y.; Moshe, O.; Rich, D. H.; Solovyov, L. A.; Gedanken, A., Highly Luminescent ZnxCd1−xSe/C Core/Shell Nanocrystals: Large Scale Synthesis, Structural and Cathodoluminescence Studies. *ACS Nano* **2009**, 3, 1864-1876.
43. Knappenberger, K. L.; Wong, D. B.; Xu, W.; Schwartzberg, A. M.; Wolcott, A.; Zhang, J. Z.; Leone, S. R., Excitation-Wavelength Dependence of Fluorescence Intermittency in CdSe Nanorods. *ACS Nano* **2008**, 2, 2143-2153.

Appendix 4.1Supporting figures

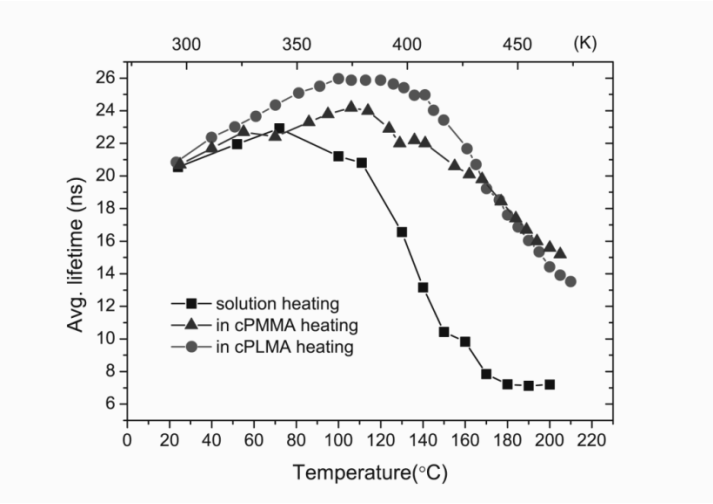

Figure A4.1. Temperature dependent average exciton lifetime for CdSe/CdS/ZnS core-shell-shell QDs in 1-Octadecene (ODE) solution (black squares), crosslinked PMMA (blue triangles) and crosslinked PLMA (red circles).

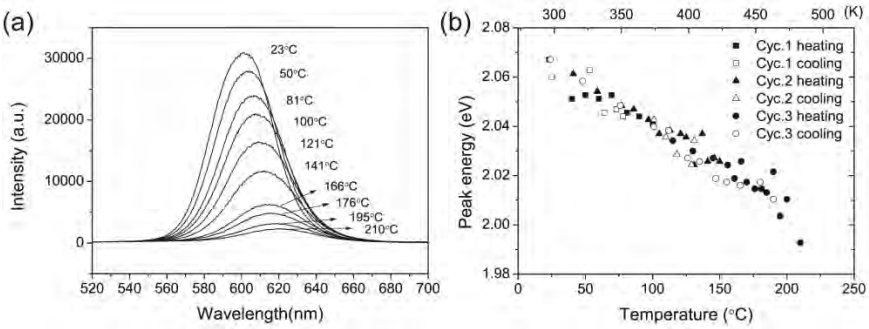

Figure A4.2. (a)Temperature dependent PL spectra of CdSe/CdS/ZnS core-shell-shell QDs in PLMA at the temperatures indicated. and (b)PL peak energy during heating cycles.

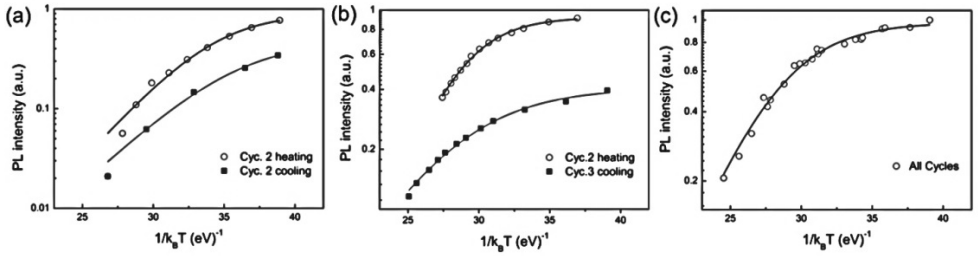

Figure A4.3. Integrated PL intensities of QDs with different structures are plotted as a function of $1/k_BT$. The solid lines are fitted curves for an Arrhenius dependence. (a) organically capped CdSe, (b)CdSe/CdS/ZnS QDs and (c) CdTe/CdSe QD.

Table A4.1. Activation energies extracted by fitting the temperature dependence of the integrated emission intensity to an Arrhenius dependence.

Sample name	E_a (eV)	Standard errors
CdSe QDs Cyc.2 heating	0.36	0.03
CdSe QDs Cyc.2 cooling	0.30	0.04
CdSe/CdS/ZnS QDs Cyc.2 heating	0.44	0.01
CdSe/CdS/ZnS QDs Cyc.3 cooling	0.26	0.02
CdTe/CdSe QDs	0.34	0.02

The thermal quenching of intensity is fitted to an Arrhenius behavior with a single activation energy, E_a which can be extracted by fitting the experimental data to the expression:

$$I \propto 1 \; / \; \left[1 + B\exp\left(- E_a \; / \; k_B T\right)\right]$$

where B is a constant, and k_B is the Boltzmann constant [Ref. 9, 10,12]. The fitted curves for organically capped CdSe, CdSe/CdS/ZnS QDs and CdTe/CdSe QDs are given in Figure A4.3.The activation energy E_a extracted from different heating

cycles are presented in Table A4.1. For the same dots, E_a changes after heating cycles due to the irreversible quenching. For CdSe/CdS nanorods determination of E_a is hampered by the strong irreversible quenching.

CHAPTER 5

Lipid Coating Dynamics of Quantum Dot Micelles via Förster Resonance Energy Transfer

Abstract

Lipid coated nanocrystal assemblies are among the most extensively investigated nanoparticle platforms for biomedical imaging and therapeutic purposes. However, very few efforts have been addressed to the lipid coating exchange dynamics in such systems, which is key to our understanding of the nanoparticles' coating stability and their interactions with the environment. Here, we apply the Förster resonance energy transfer (FRET) from quantum dot (QD) core to Cy5.5 dye labeled lipids at the surface to monitor the lipid exchange dynamics *in situ* and to study its dependence on concentration, temperature and solvent. A kinetic model was developed to describe the experimental data, allowing the rate constants and the activation energy for lipid exchange to be determined. The activation energy for lipid exchange on QD micelles is 155 kJ/mol in saline environment and 130 kJ/mol in pure water. The findings presented here provide basic knowledge on these self-assembled structures and contribute to understanding their performance and to further design of nanomedicine.

5.1 Introduction

Nanomedicine is a fast evolving field which utilizes the properties and physical characteristics of nanomaterials to treat diseases and diagnose at the molecular level.[1, 2] The rapid evolution of molecular imaging techniques has benefited from the developments and application of nanocrystals.[3] Such inorganic nanoparticles can have excellent optical, electrical or magnetic properties, and are rendered biocompatible and bio-applicable through the application of sophisticated organic coatings. The stability of the resulting materials and their coating properties significantly contribute to important nanoparticle parameters such as cytotoxicity, pharmacokinetics, degradation and long term toxicity.[4] Therefore, novel methodologies to study coating stability and dynamics in depth are imperatively needed

Self-assembled lipidic nanoparticles where lipids or other amphiphilic molecules function as coating molecules for solid nanoparticles, are among the most extensively investigated nanoparticle platforms for biomedical purposes.[3, 5-8] Dubertret and colleagues[8] were the first to apply this approach to quantum dots (QD) in 2002, which triggered investigators to follow this strategy with different nanocrystals, such as gold nanoparticles,[9] iron oxides,[6] silica nanoparticles[10, 11] and carbon nanotubes[12] for a variety of applications. These self-assembled nanocrystal core micelles are relatively easy to prepare and usually regular in size, morphology and structure.[13] Moreover, the ability to combine multiple different amphiphilic molecules with various functionalities in the nanoparticle corona brings further flexibility to this structure,[5, 14] making this platform suitable and popular for biomedical and molecular imaging purposes.[15]

Despite abounding reports on the development and application of above mentioned nanocrystal core micelle nanoparticles, very few efforts have been undertaken to investigate the lipid coating exchange dynamics of such systems. This process determines the coating stability and interaction between nanoparticles and their environment.[16-18] Earlier reports have studied lipid transfer between phospholipid self-assemblies, such as liposomes,[19] micelles,[20] and bilayered membranes[21] through introducing probing labels of isotopes, fluorescent dyes or electron spins. Among the detecting techniques used, time dependent florescence spectroscopy is a sensitive and fast method,[22] which has been applied to study lipid exchange with Förster resonance energy transfer (FRET) between two dye labeled lipids previously.[17, 23, 24] However, the multiple donor-acceptor transfer and varying transfer distance complicate the modeling and quantitative analysis in such systems.

In addition to the systems mentioned above, QD core micelles may also serve as a suitable platform for FRET-based applications.[25] To that aim we recently introduced dye labeled lipid quantum dot core micelles to investigate biological properties of lipoproteins.[7] In this platform, the FRET efficiency primarily relies on the number of absorbed dye molecules, since the distance between the QD and dye lipid in the corona is constant. Moreover, the dye/QD ratio can be easily tuned during synthesis and may alter as a result of lipid exchange with the environment. All these properties make this platform a sensitive and quantitative tool to investigate lipid exchange behavior of nanocrystal core micelles.

In the present study, we investigate the kinetics of lipid exchange between QD micelles and empty PEG micelles in different aqueous media, using time-dependent luminescence measurement of FRET from QDs to Cy5.5 labeled phospholipids incorporated in the nanoparticle's corona. In addition, we built a theoretical model that allowed us to estimate valuable kinetic data such as exchange rate and activation energy for lipid exchange, as well as the stability of nanocrystal core PEG micelles.

5.2 Experimental

Synthesis of QD micelles and PEG micelles. For synthesis of QD micelles, 20 µmol of DSPE-PEG2000, and 1 nmol CSS QDs were dispersed in 1ml chloroform. The dispersion was added drop wise to 2 ml of heated (over 80°C) deionized water under vigorous stirring. After all the organic solvent was evaporated, this water dispersion was centrifuged at 2000rpm for 10 min to remove uncoated QDs or large aggregates. Excess amount of lipids were removed through a modified Havel's ultracentrifugation separation method.[7] In brief, the QD micelle dispersion was gently placed on top of 30%wt KBr solution, which was centrifuged at 140,000x speed for 1.5h. The upper part contains free lipids or empty micelles was discarded. The middle part containing QD micelles was collected, and then desalted through a PD-10 column. Some of the sample was transfered to the HEPES buffer during desalting. PEG micelles with Cy5.5-lipid at various molar percentage of 0%, 0.5%, 1%, 1.5%, were synthesized trough the same hot dripping method described above without further purification.

Particle size analysis of QD micelle and PEG micelles. The size analysis of the QD micelle and PEG micelles was performed by a photo correlation spectroscopy, using a Malvern Zetasizer Nano which is equipped with a 634 nm laser and

measures at 12.8° and 173° scattering angle. The sample containing Cy5.5 lipid cannot be measured correctly, due to disturbance from the strong absorption of dye molecules at 634 nm and luminescence generated. All samples were filtered through 0.45 µm Millipore filters before measurement to remove impurities and aggregates.

Time-dependent photoluminescence measurement. To obtain time-dependent emission spectra, a 450W Xe lamp was used as light source and an excitation wavelength (400nm) was selected through a double grating 0.22m SPEX monochromator. A synchronized shutter was used to block the excitation light outside the acquisition time windows to avoid photobrightening of the QDs. The emission was collected through an optical fiber leading to a 0.25m monochromator (150 lines/mm, blazed at 650nm) and detected by a liquid nitrogen cooled Princeton Instruments CCD camera. The acquisition time for each measurement was 0.4 second. For all the dynamic experiment, 0.4 ml of a PEG-micelle solution was rapidly injected using a syringe into 0.8 ml QD-micelles dispersion in a quartz cuvette at a controlled temperature. Recording the emission spectra was started a few seconds before the injection, then with 1 s interval for 30 s to capture the initial fast process, and finally followed by measurement with 10 s intervals for 1 hour to cover the full time evolution. The emission spectra were recorded for sample solutions in a quartz cuvette, and the solution temperature was controlled and kept constant during the experiments by flowing fluid through the sample holder using a heater/chiller thermo-circulator. Since the Cy5.5 emission caused by direct excitation at 400 nm also contributed to the Cy5.5 peak intensity in the measured spectra, during data processing, we subtracted this part by a reference measurement of PEG-lipid solution with an identical Cy5.5 concentration. The excitation wavelength at 400 nm was chosen to minimize the contribution of direct excitation of Cy5.5.

Optical model. A microscopic optical model is derived to relate the observed emission intensity profile to the number n of adsorbed dye lipids per QD. Let I_{in} be the number of photons absorbed by the QDs. The energy of the QDs in the excited state after absorption can be emitted radiatively; can be transferred to an adsorbed dye molecule via FRET; or it can be lost via a non-radiative mechanism. The associated rates are P_R, P_{TR} and P_{NR}, respectively. The integrated intensity of QD and Cy5.5 can then be expressed as:

$$I_{QD} = \frac{P_R}{P_R + nP_{TR} + P_{NR}} I_{in} \tag{5.1}$$

$$I_{Cy5.5} = \frac{nP_{TR}D_{QY}}{P_R + nP_{TR} + P_{NR}} I_{in} \tag{5.2}$$

Where D_{QY} is the quantum yield of the Cy5.5 dye. The ratio of these intensities is proportional to n with proportionality constant γ defined by

$$\frac{I_{Cy5.5}}{I_{QD}} = \frac{D_{QY}P_{TR}}{P_R} n = \gamma n \tag{5.3}$$

The relation shows that the ratio $I_{cy5.5}/I_{QD}$ is proportional to the number n of absorbed Cy5.5 dye-lipids per QD. The value of γ can be estimated between 0.1 to 2.1 by using a Förster distance R_0 and assuming that the donor to acceptor distance r is between 5 to 9 nm (See Appendix for estimation of γ). The experimental γ value can be gained from the fitting results.

Lipid exchange model. To describe the exchange of lipid molecules between the QD surface and bulk solution, we adopt a kinetic model based on the exchange reaction.

$$PEG\text{-}lip^* + Dye\text{-}lip \underset{k^-}{\overset{k^+}{\rightleftharpoons}} PEG\text{-}lip + Dye\text{-}lip^* \tag{5.4}$$

where the star denotes the adsorbed state on QD micelles and k^+ and k^- are the forward and backward reaction constants.

Assuming first order behavior, we get the following set of differential equation for the time evolution of concentrations C of different lipids:

$$\frac{d}{dt}C_D^Q = k^+ C_D^F C_L^Q - k^- C_L^F C_D^Q \tag{5.5}$$

$$\frac{d}{dt}C_D^F = -k^+ C_D^F C_L^Q + k^- C_L^F C_D^Q \tag{5.6}$$

Subscripts D (dye) and L (lipid) denote Cy5.5 dye-lipid and PEG-lipid, respectively. Superscripts F and Q denote the free and the adsorbed on QD state, respectively. In addition, mass balance must be satisfied:

$$C_D^Q + C_D^F = C_D = const \tag{5.7}$$

$$C_L^Q + C_L^F = C_L = const \tag{5.8}$$

The initial conditions are chosen according to the experiment, assuming fast mixing of the initial QD dispersion with the added lipid solution. The initial total number of molecules adsorbed to QDs equals $N_{QD}C_{QD}$, where N_{QD} is the maximum number of lipids around the QD (the estimation of N_{QD} is 500 and is described in detail in the Appendix). The total number of adsorbed molecules does not change over time in (5.7) and (5.8), so that all QDs remain fully covered with lipids.

Fitting procedure for dynamic measurements. We combine the kinetic model based on (5.5)-(5.8) with the optical model (5.3) to obtain a relation between the (model) concentrations and the measured intensity ratio:

$$\frac{I_{Cy5.5}}{I_{QD}} = \gamma n = \gamma \frac{C_D^Q}{C_{QD}} \tag{5.9}$$

Fitting of the reaction constants to measured spectra is performed using a MATLAB script. Briefly, the initial concentration of QD-micelles and PEG and dye lipids serve as input. Assume that γ is known. For a given initial guess for the k^+ and k^-, the program reconstructs the intensity ratio as function of time according to (5.9). The resulting model curve is then compared to the measured one. This procedure is repeated until the agreement between the model and the measurement cannot be further improved. This fitting procedure can be applied either to a single measurement (individual fit) or to series of measurements with varying initial conditions (collective fit).

To determine γ, the fitting procedure is slightly modified to include γ as an additional fitting parameter and the equilibrium measurements as additional input. As the concentration of dye is low, the following approximation can be applied to the steady state:

$$\frac{I_{Dye}}{I_{QD}} = \frac{C_D^Q}{C_{QD}}\gamma \approx \left(\frac{k^+}{k^-}\frac{N_{QD}}{1 + N_{QD}C_{QD}/C_{L,added}}\gamma\right)\frac{C_D}{C_{L,added}} \tag{5.10}$$

where $C_{L,\,added}$ is the total number of PEG lipids, which is the sum of the original coating and the added amount. Note that this number is constant in the equilibrium series. The last approximation in (5.10) means that the fraction of dye lipids on the

QD surface equals total fraction of dye lipid times the equilibrium constant of reaction (5.4).

5.3 Results and discussion

Quantum dots micelle formation. Highly luminescent and air-stable core-shell-shell QDs (CSS-QD) of CdSe/CdS/ZnS were synthesized through a SILAR method.[26] Their sizes were 7.5 ±0.5 nm determined by TEM. These hydrophobic QDs (with octadecylamine and oleic acid as protecting ligands) were subsequently coated with a dense monolayer of PEGylated lipid molecules (DSPE-PEG2000), forming QD-micelles[5] (see also Figure 5.1 for a schematic representation).

For the present study it is important to characterize the QD-micelles and the empty DSPE-PEG2000 micelles (PEG-micelles). It has been reported that the self-assembling structure and dynamic properties of PEG-micelles strongly depend on properties of the aqueous media and lipid concentration.[27] We characterized the size of QD micelles and 1 mM PEG micelles dispersed in deionized water and in HEPES-buffered saline solutions through dynamic light scattering (DLS). The intensity-weighted analyses of correlation functions are shown in the Appendix Figure A5.1. In HEPES buffer, the measured average hydrodynamic diameter of PEG-micelles at 20º C is 13.5 nm, which is consistent with literature values (13.9-16.8nm),[27-29] while that of the QD-micelles is 20.3 nm. The difference in diameter between QD-micelles and PEG-lipid micelles is 6.8 nm, in agreement with the diameter of the CSS-QD, which is a clear evidence for the incorporation of a single QD per micelle. In pure water, however, no peak corresponding to PEG micelles was detected in our setup. Moreover, the hydrodynamic diameter of QD micelles in water is 17.3 nm, around 3 nm smaller than that in HEPES. Vukovic *et al.* reported that in pure water the size of DSPE-PEG2000 micelle is 4 nm, and the aggregation number (the number of molecules assembled) is below 8,[27] which is significantly smaller than ~90 in HEPES buffer.[29] In ionic solutions, sufficient counter ions provide better screening on the charged phosphate head groups of PEG-lipids, thus reducing the repulsion between them and allowing more aggregated lipids in each assembled structure. The same reasoning can be applied to the QD-micelles: a larger hydrodynamic diameter in HEPES was observed compared to that in pure water, possibly due to denser lipid coating on the QD surface and hence more extended PEG brushes. These observations also suggest that the lipid coating dynamics of QD micelles may be different in these two solvent systems and therefore it is worthwhile to investigate both of them separately.

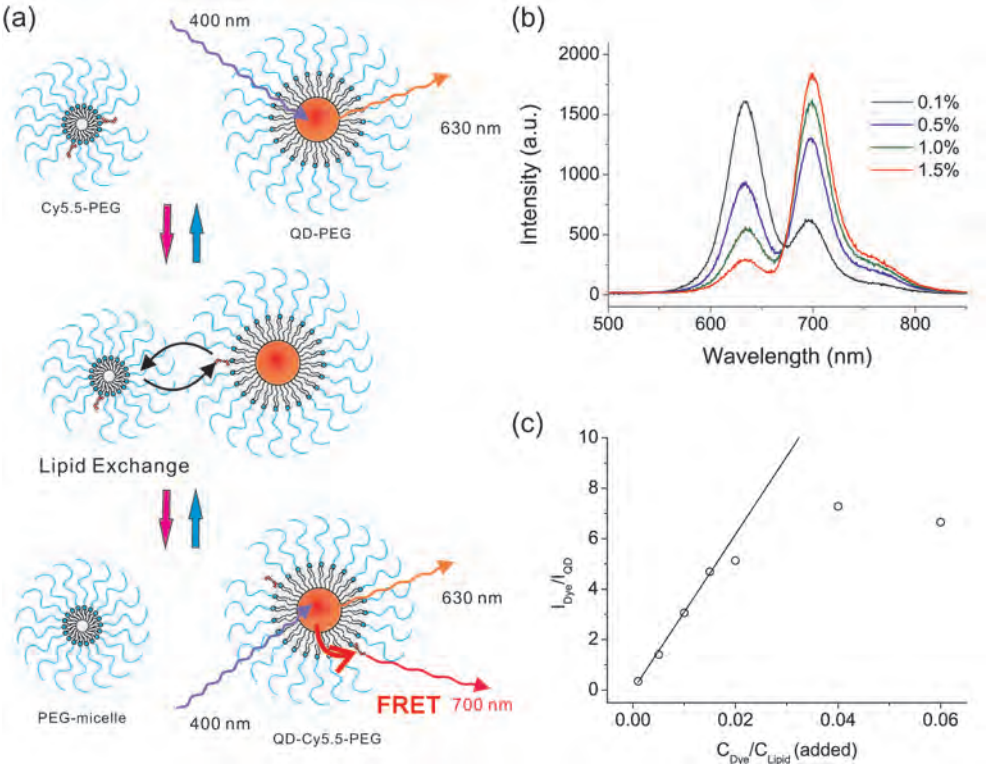

Figure 5.1. a. Schematic representation of lipid-exchange between Cy5.5 labeled PEG micelles and quantum dot (QD) micelles, and the Förster resonance energy transfer (FRET) from QD to Cy5.5 lipids. **b.** Equilibrium state measurement. QD micelles and PEG micelles containing indicated percentage of Cy5.5 lipid were mixed in pure water, and the emission spectra were recorded after equilibrated. **c.** The intensity ratios of Cy5.5 to QD emission, $I_{Cy5.5}/I_{QD}$ are plotted against the content of Cy5.5. A linear fit is applied to the data with lipid content value below 2%.

Optical model and equilibrium state measurement. The large spectral overlap between QD emission and Cy5.5 absorption (Appendix, Figure A5.2) and the close distance between the QD and Cy5.5 (estimated distance from QD center to Cy5.5 is about 7nm) provide the necessary conditions for energy transfer. A Förster distance for energy transfer R_0= 73.8 Å was calculated using the Förster

theory (See Appendix 5.1 and Figure A5.2b).[30] To investigate the energy transfer between QD and Cy5.5 dye we chose an excitation wavelength of 400 nm for all experiments in this work, since at this wavelength the QD absorbs efficiently while Cy5.5 has very low absorbance, giving a very small contribution to the Cy5.5 emission by direct excitation at 400 nm. In order to correlate the experimentally observed emission intensities to the average number of Cy5.5-lipids in a QD-PEG micelle, we introduce an optical model (equation 5.3). Within this model the intensity ratio of Cy5.5 to QD emission ($I_{Cy5.5}$ /I_{QD}) is proportional to the number of adsorbed Cy5.5 lipids per QD, *n*, with a proportionality constant that we denote by γ. To verify the optical model and to determine its range of applicability, we performed a series of equilibrium state measurements of prolonged lipid exchange. The experiments were carried out by mixing dispersions of 5 nM QD-micelles (all concentrations are given for solutions after mixing) and 3.3 µM PEG-lipids in water, varying only the content of Cy5.5-lipids in the PEG-lipid solution. The mixtures were kept in dark at room temperature over night before emission spectra were measured. The emission spectra are shown in Figure 5.1b. As the content of Cy5.5 lipids increases from 0.1% to 1.5%, the Cy5.5 peak at 690 nm increases while the QD peak at 630 nm decreases correspondingly, indicating a higher efficiency of energy transfer. In Figure 5.1c, the ratio of integrated intensities of QD and Cy5.5 emission $I_{cy5.5}$ /I_{QD} is plotted against the content of dye lipid. In agreement with the optical model, there is a linear relation between the dye concentration and the intensity ratio. However, this linear relation only holds at low dye concentrations; above 1.5%, the linear relation breaks down, and the intensity ratio becomes lower than expected. This deviation is ascribed to concentration quenching of the fluorescence for Cy5.5 lipids attached on the QD micelles.[23, 31] When the chromophores get too close to each other at a higher load, energy transfer between the chromophores becomes significant and leads to multi-step energy transfer to quenching sites. Therefore, the quantitative analysis of experiment using the optical model is limited to the linear region in Figure 5.1c in the present study. Note that saturation of Cy5.5-lipids cannot be the cause for this non-linear effect: there are 1-40 dye molecules per QD, which is significantly smaller than the maximum number N_{max} of total lipids adsorbed on a QD (estimated to be around 500; see Appendix 5.1 for an estimate of N_{max}).

Exchange Dynamics. The lipid exchange kinetics between the QD-micelles and the surrounding lipid sources, in this study: PEG-micelles, will strongly depend on the environmental conditions, mainly the PEG-lipids concentration, temperature and also the ionic strength of the solution. Investigating the exchange process under various conditions helps understanding the dynamics of lipid-coated nanocrystals and determining the corresponding exchange rates provides information

on the stability of these structures. Therefore, it is crucial to have a method for probing the exchange dynamics in real time. To this end, the high FRET sensitivity of our system and fast response time of photoluminescence spectroscopy enable us to monitor the exchange process with a time resolution below 1 s. A typical exchange experiment was carried out through fast mixing of a solution of QD-micelles without Cy5.5-lipid and a solution of PEG-micelles with 1% Cy5.5-lipid. The evolution of emission spectra was followed by continuously recording the emission spectra at regular time intervals. The result of a typical measurement is presented in Figure 5.2a, where the integrated intensities of Cy5.5 and QD emission ($I_{Cy5.5,}$ I_{QD}, respectively) are plotted against time after mixing. A decrease of I_{QD} and a simultaneous increase of $I_{Cy5.5}$ are observed. Both intensities show a rapid initial change; then the rate slows down, and eventually approach constant values. This can be attributed to the equilibrium between adsorption and desorption of dye molecules.

For a systematic study of the lipid exchange dynamics we carried out a series of experiments with a varying concentration of added PEG lipid (containing 1% of Cy5.5-lipid) in the range ~1 to 30 μM at room temperature, while the concentration of QD-micelles remained 0.015 μM. The time evolution of $I_{Cy5.5}/I_{QD}$ for the series of experiments in water is presented in Figure 5.2c, and for the experiments in HEPES in Figure 5.2d. For both conditions, the $I_{Cy5.5}/I_{QD}$ ratio increases faster and reaches a higher equilibrium value when the concentration of added PEG lipid with Cy5.5 dye is higher, as expected. The experiments show a rapid exchange during the first ~500 s. After ~1000 s the ratio $I_{Cy5.5}/I_{QD}$ reaches values close to equilibrium, giving an indication of the time scale at which lipid exchange occurs. Note that in experiments with high lipid concentrations there is a drop in the ratio $I_{Cy5.5}/I_{QD}$ after the maximum is reached, probably due to concentration quenching, as discussed above.

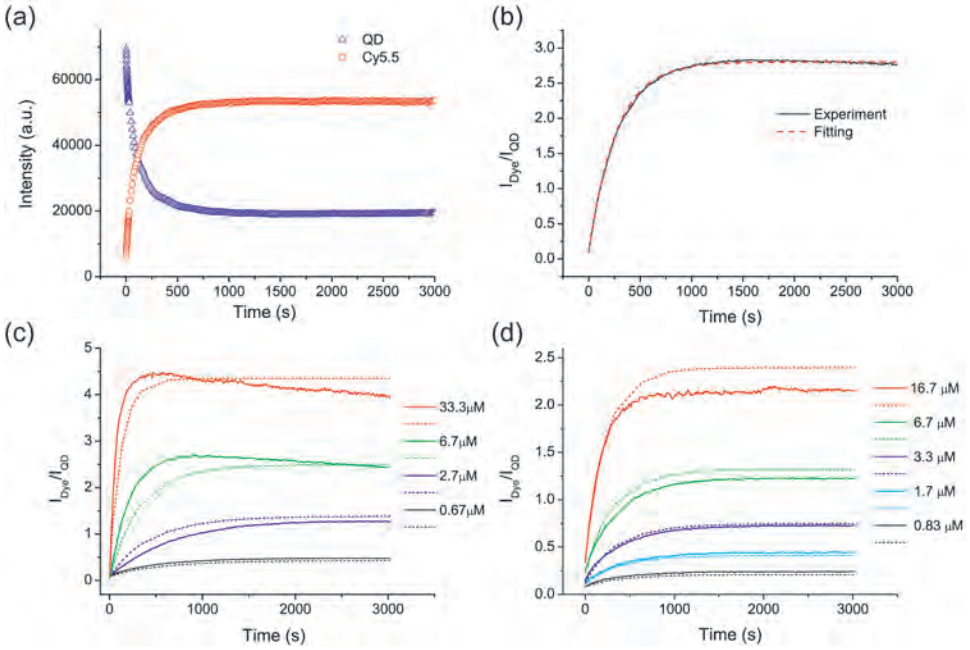

Figure 5.2. Results of time resolved measurement of a typical lipid exchange experiment. (a) Integrated of QD and Cy5.5 emission intensity plotted against time. (b) Individual fitting (dashed line) on the experimental results (solid line) for a typical lipid exchange experiment showing the time evolution of the ratio of the integrated Cy5.5 and QD emission intensities. (c and d) Series of experiments with indicated concentrations of added PEG lipids (containing 1% of Cy5.5-lipids) at room temperature (RT), while the concentration of QD micelles remained constant. The experiments were carried out at RT (c) in pure water and (d) in HEPES buffer. Solid lines are experimental results and dashed lines are collective fitting results.

Lipid exchange modeling. To obtain quantitative information from the kinetic measurements, we describe the exchange dynamics using a model reaction. The detachment of lipid (either PEG-lipid or Cy5.5-lipid) from the QD micelle is assumed to be the rate-limiting step in the exchange process. First order behavior in each component is assumed, leading to the following model reaction:

$$PEG\text{-}lip* + Dye\text{-}lip \underset{k^-}{\overset{k^+}{\rightleftharpoons}} PEG\text{-}lip + Dye\text{-}lip* \qquad (4)$$

The fitting result for a typical exchange experiment in water is shown in Figure 5.2b by the dashed line; the agreement is excellent. Fitting of individual experimental curves in the series shown in Figure 5.2c leads to excellent agreement and yields parameters k^+ and k^- varying within factor of two around 250 $(mol/l)^{-1}s^{-1}$, which is a typical accuracy of chemical kinetics measurements. The ratio between the two rate constants fluctuates around 1, suggesting that in pure water Cy5.5 lipids and PEG lipids bind approximately equally strongly to the QD. Fitting the full series of measurements simultaneously provides a more consistent strategy for model validation and analysis. The collective fitting results for experiments in pure water are shown by dashed lines in Figure 5.2c. The agreement with experimental data is good given that only two fitting parameters are adjusted to fit all four experimental curves. The obtained rate constants (Table 5.1) are k^+ = 246.0 $(mol/l)^{-1}s^{-1}$ and k^- = 238.2 $(mol/l)^{-1}s^{-1}$, in line with the results of the individual fits. The observation that these two rate constants are very close indicates that the energies for the dye lipid and PEG lipid detachment from the QD micelle in pure water are approximately equal. The optical constant γ = 1.05 is also obtained from the collective fit using a modified fitting procedure, and used throughout all subsequent fits. The donor (QD) to acceptor (Cy5.5) distance can be then calculated as 5.6 nm and Cy5.5 chromophore to QD surface distance is 1.85 nm (see Appendix 5.1 for the estimation of γ).

In the HEPES solution the PEG-lipids form larger and more stable micelles and one may expect stronger influence from the PEG micelles and more complicated dynamics than in pure water. However, the exchange happens on the same time scale and the intensity ratio curves have the same shape as for experiments in pure water (see Figures 5.2d). The same exchange kinetics model has been applied for the fitting of the measurements in HEPES. The agreement of the collective fit is as good as for the experiments in water. The resulting exchange rate constants, k^+ = 627.6 and k^- = 132.9 $(mol/l)^{-1}s^{-1}$, are in the same range as that for pure water, but k^+ is now over four times larger than k^- indicating that in HEPES the binding of dye lipids on the QD micelles is stronger than for PEG lipids. In Table 5.1 the fitting parameters for the exchange kinetics are collected.

Table 5.1. Fitting parameters for the lipid exchange of QD micelles in water and HEPES. The parameters k^+ and k^- give the room temperature exchange rates for the forward and backward reaction determined by the detachment of a PEG-lipid and dye-lipid, respectively. The activation energies for lipid detachment have been determined from temperature dependent kinetic measurements.

	k^+ $[(mol/l)^{-1}s^{-1}]$	k^- $[(mol/l)^{-1}s^{-1}]$	ΔE_{act} (kJ/mol) k^+	ΔE_{act} (kJ/mol) k^-
In water	246.0	238.2	132	132
In HEPES	627.6	132.9	153	158

A generally accepted assumption is that dissociation of amphiphiles from micelles into solution is the rate-limiting step in phospholipid exchange.[24, 29] In the presently investigated system there are two dissociation rates that need to be considered: one for QD micelles and one for empty PEG micelles. The kinetic model used in the present work does not consider the empty PEG micelles and assumes that lipids that are not attached to the QD micelle behave as free lipids in solution. This assumption holds if PEG lipids attach and detach to PEG micelles much faster than to QD micelles, making the latter the rate limiting step, and the influence of the former on the exchange dynamics negligible. Indeed, as will be discussed below, there are strong indications that the stability of the QD micelles is larger than that of empty micelles due to a stronger attachment of lipids to the QD core justifying a simple model based on lipid detachment from the QD micelles. More complicated kinetic models have been suggested,[19, 32] but since the presently used minimal model is sufficient to accurately describe results with only two fitting parameters, the introduction of additional parameters to the model will not provide a better insight in the rate limiting step in the lipid exchange dynamics.

Dye lipid detachment. To obtain further qualitative information on lipid exchange with QD micelles, we also performed the lipid exchange experiment in the reverse way. QD micelles were preloaded with 1% Cy5.5-lipids during the synthesis; and these QD-Cy5.5 micelles were mixed with PEG-micelles solutions with varying lipid concentrations. A decrease of the Cy5.5 emission intensity is observed over time, and concurrently the increase of QD emission intensity, resulting in decrease of $I_{Cy5.5}/I_{QD}$ in time (Figure 5.3). The observations are explained by dye molecules leaving the QD micelles due to lipid exchange with PEG micelles. As

the dye-lipids are exchanged by PEG-lipids the number of dye-lipids at the QD surface decreases and the energy transfer from QD to dye decreases in time.

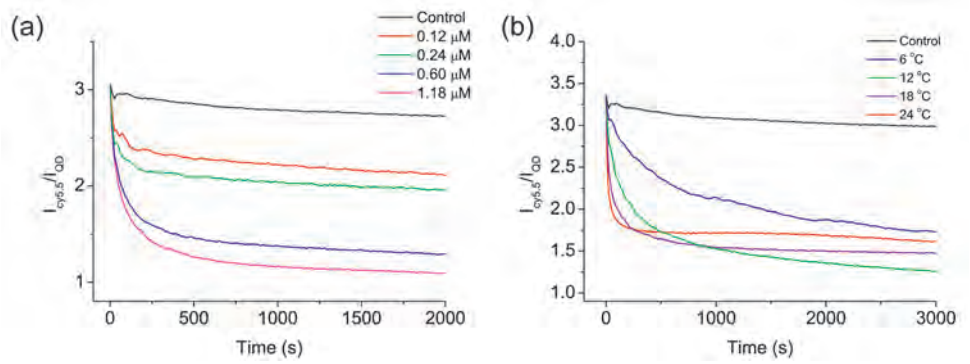

Figure 5.3. Measured intensity ratio of the Cy5.5 dye and QD emission $I_{Cy5.5}/I_{QD}$ plotted against time for the dye-lipid detaching experiments, where Cy5.5-lipids initially adsorbed in the QD corona are exchanged by PEG-lipids. **(a)** The experiment was carried out at 16°C. A 0.0167 μM QD micelles solution containing 1% Cy5.5 lipids was mixed with indicated concentrations of PEG lipids **(b)** 0.0167 μM QD micelles containing 1% Cy5.5 lipids were mixed with 1.18 μM PEG-lipids solution at indicated temperatures. In the control measurement, pure solvent was injected.

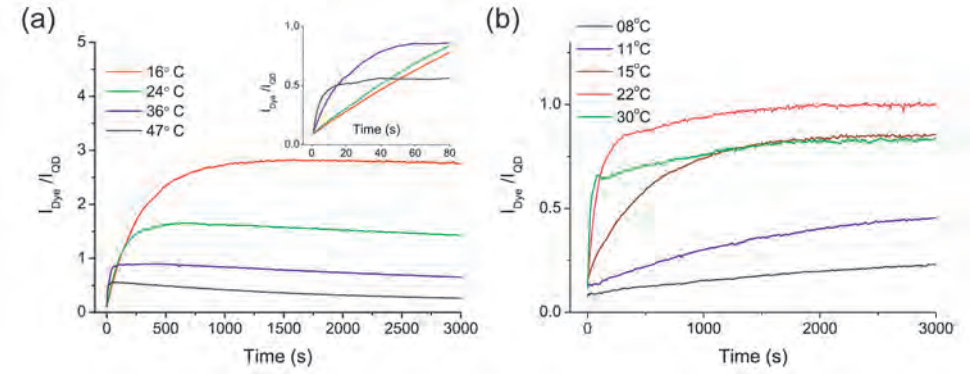

Figure 5.4. Results of temperature dependent lipid exchange experiments. QD micelles and PEG micelles solution (containing 1% Cy5.5-lipid) were mixed with fixed concentrations at different temperatures. The time-dependent PL spectra

were recorded after mixing at indicated temperatures (a) in pure water, and (b) in HEPES buffer. The inset shows the initial stage after mixing.

As a result, the QD emission intensity increases at the expense of the dye emission intensity. The time scale is similar to that observed in the reverse experiment. After a fast initial decrease of I_{Dye}/I_{QD} during the first 500 s the system slowly develops towards equilibrium after ~1000 s. The exchange kinetics is clearly concentration dependent and a faster exchange is observed for increasing concentrations of added lipids, and leads to a lower final number of dye molecules in QD micelles

Temperature dependence. The lipid exchange is expected to become faster at elevated temperatures. For *in vivo* studies the dynamics and stability of QD micelles at higher temperatures is important. Previous studies on PEG micelles reported a strong temperature-dependent lipid exchange[24] and desorption rates.[29] Since the lipid exchange is a thermally activated process, the activation energy can be obtained through determining the exchange rate at different temperatures, and the coating stability of nanocrystal micelles under bio-conditions can also be estimated. Temperature-dependent lipid exchange experiments were performed both in pure water and in HEPES, through mixing 0.015 μM QD-micelles and a 33.3 μM PEG-micelles solution (containing 1% Cy5.5-lipid). The time-dependent PL spectra were recorded after mixing at different temperatures from 8ºC up to 47ºC. The results are shown in Figure 5.4. As expected, at a higher temperature, a faster initial increase of the intensity ratio $I_{Cy5.5}/I_{QD}$ is observed, indicating a faster exchange rate. After a fast initial increase a maximum ratio is reached and, at elevated temperatures, a decrease of the $I_{Cy5.5}/I_{QD}$ ratio is observed on longer time scales. The effect is more pronounced at higher temperatures and also more pronounced in pure water than in HEPES. The concentration quenching probably causes the decrease. At higher temperatures with increased mobility of the dye-lipids in the micelle, concentration quenching becomes more prominent.

For the evaluation of the temperature dependence of the lipid exchange the initial change of the $I_{Cy5.5}/I_{QD}$ ratio is important and this part of the data was analyzed for each curve individually. The same fitting procedure as discussed above was applied to determine the kinetic constants k^+ and k^- at each temperature. A strong variation is observed from about 20 $(mol/l)^{-1}s^{-1}$ at 8ºC to 60 000 $(mol/l)^{-1}s^{-1}$ at 47ºC. The Arrhenius equation can be used to calculate the activation energy E_{act} for lipid detachment:

$$k = k_0 e^{-\frac{E_{act}}{RT}} \tag{11}$$

where R is the universal gas constant and T is the temperature.

In Figure 5.5, the logarithms of rate constants $ln(k)$ are plotted against inverse temperature $1/T$ (in K^{-1}). The observed linear relationship between $ln(k)$ and $1/T$ shows that the exchange dynamics is a thermally activated process. A linear fit was applied for each group of data and the slope obtained from the fit is equal to $-E_{act}/RT$. A common intercept for k^+ and k^- was imposed for fitting, since for a reversible reaction (as in our case), all states become equally likely ($\ln k_0^+ = \ln k_0^-$) at infinite temperature ($1/T \rightarrow 0$).

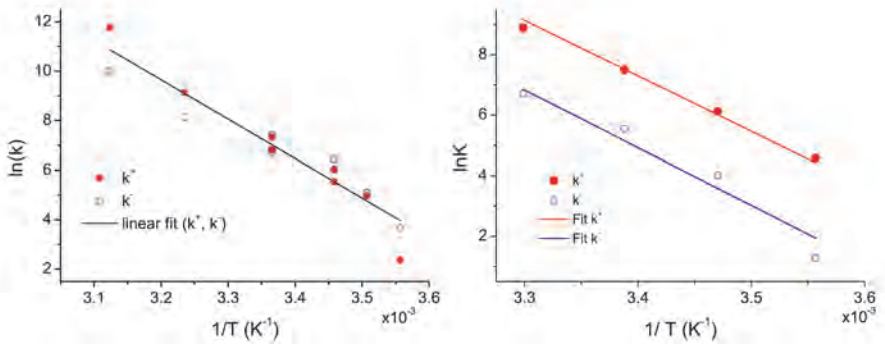

Figure 5.5. Arrhenius plot showing the logarithms of lipid exchange rate constants $ln(k)$ as a function of inverse temperature $1/T$ (in K^{-1}) for lipid exchange experiments carried out (a) in pure water, and (b) in HEPES buffer. Solid lines represent linear fits to the data of k^+ and k^-, respectively.

In Figure 5.5a, for experiments in pure water, the two fitted lines are on top of each other: they have the same intercept (not shown in the figure) and their slopes differ only in the fifth significant digit. This is consistent with the previous results of the concentration series (Figure 5.2), where equal values for k^+ and k^- were found indicating equal binding strengths for PEG lipids and Cy5.5-lipids on QD-micelles. The resulting activation energy for lipid detachment obtained from the Arrhenius plot in Figure 5.5 is 132 kJ/mol, which is the activation energy for PEG lipids or Cy5.5-lipids detaching from the QD micelles.

The same fitting procedure was applied to the temperature dependent measurements for QD-micelles in HEPES. The result is plotted in Figure 5.5b; the two data series for k^+ and k^- show strong linear correlation. The two fitted straight lines have, as imposed, the same intercept; but they have different slopes. The calculated activation energies are 153 kJ/mol and 158 k/mol for k^+ and k^-, respectively. Note that these values are about 20 kJ/mol larger than those in pure water. It implies that the PEG-lipid self-assembled structure is generally more stable in saline solutions for both QD micelles and PEG micelles. This extra stability, corresponding with larger micelles sizes discussed previously, is explained by screening of the charged PO_4^- groups on the lipids in ionic solutions, which reduces the repulsion force between lipid molecules, hence allowing a denser and more stable coating on the QD micelles resulting in a higher activation energy for lipid detachment. The difference in activation energy determined for k^+ and k^- in HEPES implies that in a QD-micelle the binding energy for a Cy5.5 lipid is 5 kJ/mol higher than for a PEG-lipid. This result is consistent with the collective fitting results of Figure 5.2d, where the forward exchange rate k^+ is larger than the backward rate k^-. The change of Gibbs free energy ΔG upon exchange of PEG lipid by the dye can be calculated from ratio of k^+ and k^-, yielding $\Delta G = RT\ln\left(\frac{k^+}{k^-}\right) = 3.8\ \mathrm{kJ/mol}$. This value is in good agreement with the difference in activation energy 5 kJ/ mol obtained from the Arrhenius plots in Figure 5.5

Through lipid exchange dynamics experiments, we have obtained important information on the dynamics and stability of lipid coating on QD micelles. The activation energies determined above for lipid detachment from QD micelles is much larger than the activation energy of lipid exchange in other self-assembled lipid structures. For examples, the activation energy for exchange of dimyristoylphosphatidylcholine (DMPC) lipids between large unilamellar vesicles is 80-90 kJ/mol; [19, 33] while the activation energy for DSPE-PEG2000 lipids desorption from PEG micelles is about 79 kJ/mol for a core in the fluid phase (>15º C), and about 156kJ/mol for a core in the glassy phase (<15º C).[29] The higher activation energies indicate that the QD-micelle structure is much more stable than other lipid bilayer structures and empty PEG micelles. The high stability is not surprising and can be understood from the structure of QD micelles where in the inner layer the hydrophobic ligands are immobilized on the nanocrystal surface through chemical bonding. This solid core provides extra stability compared to the inner layer for lipids in self-assembled vesicles which allows diffusing and flip-flopping between the inner and outer layer. Furthermore, compared to the hydrophobic core of PEG-micelle, the QD surface provides a more flattened geometry where those attached hydrophobic head groups of lipids may have more ordered alignment, and hence

stronger the van der Waals interactions, contributing to a more stable QD micelle structure.

In addition to the role of the QD core it is important to point out that the stability of lipid coated micelle and their dynamic behavior is also related with the characteristics of the lipids, such as the length of hydrophobic chain, the shape of the lipids and the solubility of the hydrophilic part. Here QD micelles with DSPE-PEG2000 lipid have been investigated. The same method can be applied to investigate other lipid or amphiphilic molecules coated nanocrystal structures to obtain information on the stability and lipid exchange dynamics.

The results of this work should be taken into consideration during design and *in vivo* application of lipid coated nanocrystals. The lipid exchange process between nanoparticles and their surroundings occurs on the time scale of seconds to minutes at body temperature, which may cause loss of the native coating and affect the integrity and functionality of nanoparticles. This also encourages application of these FRET nanoparticles further for *in vivo* studies to investigate the stability and dynamics of lipid coated nanocrystals in living organisms.

5.4 Conclusions

In summary, we have shown that QD micelles coated with PEG-lipids and Cy5.5 labeled lipids are an effective FRET system to investigate lipid exchange kinetics. After mixing lipid coated QD-micelles and a PEG-lipid dispersion containing Cy5.5 labeled lipids, the dynamics of lipid exchange can be monitored *in situ.* The increase of the ratio of the dye to quantum dot emission intensity is followed in time and reflects the change of FRET efficiency due to exchange of optically inactive lipids with dye-labeled lipids to which energy transfer occurs. The concentration and temperature dependence of lipid exchange were studied in both water and HEPES and analyzed with a relatively simple kinetic model which, nevertheless, describes well the full series of concentration dependent measurements with only two rate constants. Temperature dependent measurements and the resulting rate constants allow the determination of the activation energy for the lipid exchange, which is around 130 kJ/mol for the QD-micelles in water and 155 kJ/mol in a HEPES buffer. The method presented provides a sensitive probe to investigate lipid exchange of nanocrystal core micelles and yields important information on their stability which is important for biomedical imaging or pharmaceutical studies where nanocrystal based micelles are gaining importance.

References

1. Peer, D.; Karp, J. M.; Hong, S.; Farokhzad, O. C.; Margalit, R.; Langer, R., Nanocarriers as an emerging platform for cancer therapy. *Nat. Nanotechnol.* **2007**, 2, 751-60.
2. Lobatto, M. E.; Fuster, V.; Fayad, Z. A.; Mulder, W. J., Perspectives and opportunities for nanomedicine in the management of atherosclerosis. *Nat. Rev. Drug Discov.* **2011**, 10, 835-52.
3. Mulder, W. J. M.; Strijkers, G. J.; van Tilborg, G. A. F.; Cormode, D. P.; Fayad, Z. A.; Nicolay, K., Nanoparticulate Assemblies of Amphiphiles and Diagnostically Active Materials for Multimodality Imaging. *Acc. Chem. Res.* **2009**, 42, 904-914.
4. Sanhai, W. R.; Sakamoto, J. H.; Canady, R.; Ferrari, M., Seven challenges for nanomedicine. *Nat. Nanotechnol.* **2008**, 3, 242-4.
5. Mulder, W. J. M.; Koole, R.; Brandwijk, R. J.; Storm, G.; Chin, P. T. K.; Strijkers, G. J.; Donega, C. D.; Nicolay, K.; Griffioen, A. W., Quantum dots with a paramagnetic coating as a bimodal molecular imaging probe. *Nano Lett.* **2006**, 6, 1-6.
6. Cormode, D. P.; Skajaa, T.; van Schooneveld, M. M.; Koole, R.; Jarzyna, P.; Lobatto, M. E.; Calcagno, C.; Barazza, A.; Gordon, R. E.; Zanzonico, P.; Fisher, E. A.; Fayad, Z. A.; Mulder, W. J., Nanocrystal core high-density lipoproteins: a multimodality contrast agent platform. *Nano Lett.* **2008**, 8, 3715-23.
7. Skajaa, T.; Zhao, Y.; van den Heuvel, D. J.; Gerritsen, H. C.; Cormode, D. P.; Koole, R.; van Schooneveld, M. M.; Post, J. A.; Fisher, E. A.; Fayad, Z. A.; de Mello Donega, C.; Meijerink, A.; Mulder, W. J., Quantum Dot and Cy5.5 Labeled Nanoparticles to Investigate Lipoprotein Biointeractions via Forster Resonance Energy Transfer. *Nano Lett.* **2010**.
8. Dubertret, B.; Skourides, P.; Norris, D. J.; Noireaux, V.; Brivanlou, A. H.; Libchaber, A., In Vivo Imaging of Quantum Dots Encapsulated in Phospholipid Micelles. *Science* **2002**, 298, 1759-1762.
9. Cormode, D. P.; Roessl, E.; Thran, A.; Skajaa, T.; Gordon, R. E.; Schlomka, J. P.; Fuster, V.; Fisher, E. A.; Mulder, W. J.; Proksa, R.; Fayad, Z. A., Atherosclerotic plaque composition: analysis with multicolor CT and targeted gold nanoparticles. *Radiology* **2010**, 256, 774-82.
10. Koole, R.; van Schooneveld, M. M.; Hilhorst, J.; Castermans, K.; Cormode, D. P.; Strijkers, G. J.; de Mello Donegá, C.; Vanmaekelbergh, D.; Griffioen, A. W.; Nicolay, K.; Fayad, Z. A.; Meijerink, A.; Mulder, W. J. M., Paramagnetic Lipid-Coated Silica Nanoparticles with a Fluorescent Quantum Dot Core: A New Contrast Agent Platform for Multimodality Imaging. *Bioconjugate Chem.* **2008**, 19, 2471-2479.
11. van Schooneveld, M. M.; Vucic, E.; Koole, R.; Zhou, Y.; Stocks, J.; Cormode, D. P.; Tang, C. Y.; Gordon, R. E.; Nicolay, K.; Meijerink, A.; Fayad, Z. A.; Mulder, W. J. M., Improved biocompatibility and pharmacokinetics of silica nanoparticles by means of a lipid coating: A multimodality investigation. *Nano Lett.* **2008**, 8, 2517-2525.
12. Welsher, K.; Liu, Z.; Sherlock, S. P.; Robinson, J. T.; Chen, Z.; Daranciang, D.; Dai, H., A route to brightly fluorescent carbon nanotubes for near-infrared imaging in mice. *Nat. Nanotechnol.* **2009**, 4, 773-80.
13. Michalet, X.; Pinaud, F. F.; Bentolila, L. A.; Tsay, J. M.; Doose, S.; Li, J. J.; Sundaresan, G.; Wu, A. M.; Gambhir, S. S.; Weiss, S., Quantum Dots for Live Cells, in Vivo Imaging, and Diagnostics. *Science* **2005**, 307, 538-544.
14. Mulder, W. J.; Cormode, D. P.; Hak, S.; Lobatto, M. E.; Silvera, S.; Fayad, Z. A., Multimodality nanotracers for cardiovascular applications. *Nat. Clin. Pract. Cardiovasc. Med.* **2008**, 5 Suppl 2, S103-11.

15. Peer, D.; Karp, J. M.; Hong, S.; Farokhzad, O. C.; Margalit, R.; Langer, R., Nanocarriers as an emerging platform for cancer therapy. *Nat Nano* **2007**, 2, 751-760.
16. Aggarwal, P.; Hall, J. B.; McLeland, C. B.; Dobrovolskaia, M. A.; McNeil, S. E., Nanoparticle interaction with plasma proteins as it relates to particle biodistribution, biocompatibility and therapeutic efficacy. *Adv Drug Deliv Rev* **2009**, 61, 428-37.
17. Nel, A. E.; Madler, L.; Velegol, D.; Xia, T.; Hoek, E. M.; Somasundaran, P.; Klaessig, F.; Castranova, V.; Thompson, M., Understanding biophysicochemical interactions at the nano-bio interface. *Nat. Mater.* **2009**, 8, 543-57.
18. Li, Y.; Budamagunta, M. S.; Luo, J.; Xiao, W.; Voss, J. C.; Lam, K. S., Probing of the assembly structure and dynamics within nanoparticles during interaction with blood proteins. *ACS Nano* **2012**, 6, 9485-95.
19. Wimley, W. C.; Thompson, T. E., Exchange and flip-flop of dimyristoylphosphatidylcholine in liquid-crystalline, gel, and two-component, two-phase large unilamellar vesicles. *Biochemistry* **1990**, 29, 1296-303.
20. Fullington, D. A.; Nichols, J. W., Kinetic analysis of phospholipid exchange between phosphatidylcholine/taurocholate mixed micelles: effect of the acyl chain moiety of the micellar phosphatidylcholine. *Biochemistry* **1993**, 32, 12678-84.
21. Liu, J.; Conboy, J. C., 1,2-diacyl-phosphatidylcholine flip-flop measured directly by sum-frequency vibrational spectroscopy. *Biophys. J.* **2005**, 89, 2522-32.
22. Koole, R.; Schapotschnikow, P.; Donega, C. D.; Vlugt, T. J. H.; Meijerink, A., Time-dependent photoluminescence spectroscopy as a tool to measure the ligand exchange kinetics on a quantum dot surface. *ACS Nano* **2008**, 2, 1703-1714.
23. Bai, J.; Pagano, R. E., Measurement of spontaneous transfer and transbilayer movement of BODIPY-labeled lipids in lipid vesicles. *Biochemistry* **1997**, 36, 8840-8.
24. Reulen, S. W.; Merkx, M., Exchange kinetics of protein-functionalized micelles and liposomes studied by Forster resonance energy transfer. *Bioconjug. Chem.* **2010**, 21, 860-6.
25. Medintz, I. L.; Clapp, A. R.; Mattoussi, H.; Goldman, E. R.; Fisher, B.; Mauro, J. M., Self-assembled nanoscale biosensors based on quantum dot FRET donors. *Nat. Mater.* **2003**, 2, 630-638.
26. Xie, R.; Kolb, U.; Li, J.; Basche, T.; Mews, A., Synthesis and Characterization of Highly Luminescent CdSe - Core CdS/Zn0.5Cd0.5S/ZnS Multishell Nanocrystals. *J. Am. Chem. Soc.* **2005**, 127, 7480-7488.
27. Vuković, L.; Khatib, F. A.; Drake, S. P.; Madriaga, A.; Brandenburg, K. S.; Král, P.; Onyuksel, H., Structure and Dynamics of Highly PEG-ylated Sterically Stabilized Micelles in Aqueous Media. *J. Am. Chem. Soc.* **2011**, 133, 13481-13488.
28. Ashok, B.; Arleth, L.; Hjelm, R. P.; Rubinstein, I.; Onyuksel, H., In vitro characterization of PEGylated phospholipid micelles for improved drug solubilization: effects of PEG chain length and PC incorporation. *J. Pharm. Sci.* **2004**, 93, 2476-87.
29. Kastantin, M.; Ananthanarayanan, B.; Karmali, P.; Ruoslahti, E.; Tirrell, M., Effect of the lipid chain melting transition on the stability of DSPE-PEG(2000) micelles. *Langmuir* **2009**, 25, 7279-86.
30. Clapp, A. R.; Medintz, I. L.; Mauro, J. M.; Fisher, B. R.; Bawendi, M. G.; Mattoussi, H., Fluorescence Resonance Energy Transfer Between Quantum Dot Donors and Dye-Labeled Protein Acceptors. *J. Am. Chem. Soc.* **2004**, 126, 301-310.
31. Thomas, M. J.; Pang, K.; Chen, Q.; Lyles, D.; Hantgan, R.; Waite, M., Lipid exchange between mixed micelles of phospholipid and triton X-100. *Biochimica et Biophysica Acta (BBA) - Biomembranes* **1999**, 1417, 144-156.

32. Storch, J.; Kleinfeld, A. M., Transfer of long-chain fluorescent free fatty acids between unilamellar vesicles. *Biochemistry* **1986**, 25, 1717-26.
33. Nakano, M.; Fukuda, M.; Kudo, T.; Endo, H.; Handa, T., Determination of Interbilayer and Transbilayer Lipid Transfers by Time-Resolved Small-Angle Neutron Scattering. *Phys. Rev. Lett.* **2007**, 98, 238101.
34. Lakowicz, J. R., *Principles of Fluorescence Spectroscopy*. Springer London, Limited: 2009

Appendix 5.1Supporting figures and methods

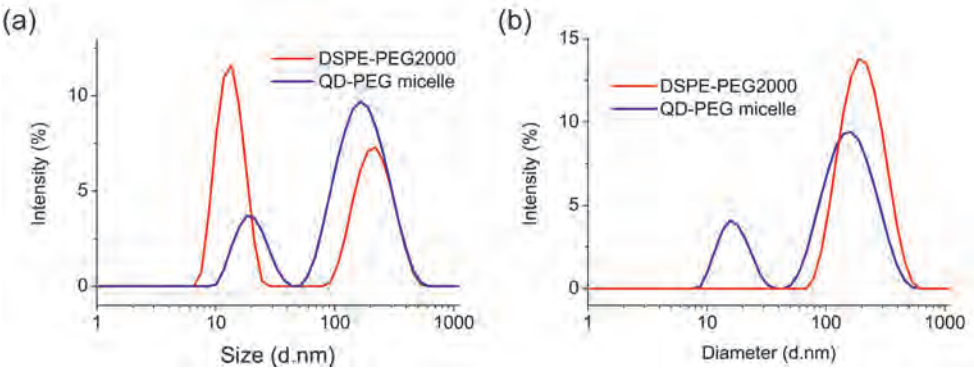

Figure A5.1. Size distribution of PEG and QD micelles (a) in HEPES buffer and (b) in pure water. The second board peak >100 nm are loose aggregates of individual micelles in the system. These lose aggregates show a high peak in the intensity weighted plot due to the stronger light scattering by larger objects.

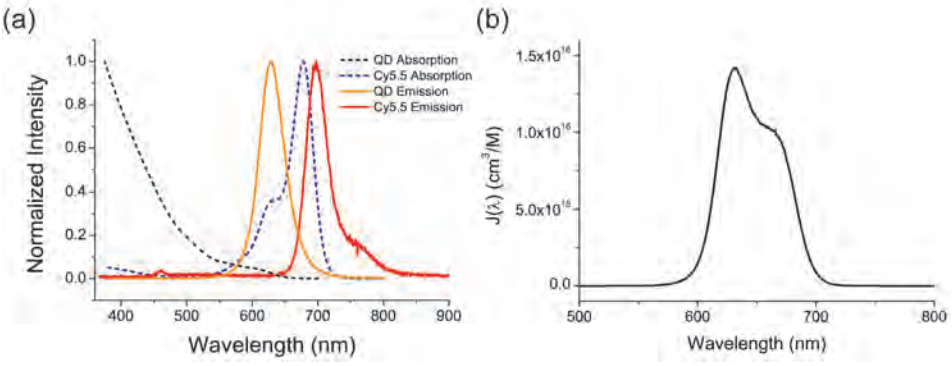

Figure A5.2.(a) Absorption and emission spectra of QDs and Cy5.5 lipids. In order to calculate the Förster distance for energy transfer between QD and Cy5.5, the overlap function J(λ) between QD emission and Cy5.5 lipid absorption is calculated. $J(\lambda)=F_D(\lambda)\,\varepsilon_A(\lambda)\lambda^4$, where $F_D(\lambda)$ is dimensionless normalized donor emission spectrum, and $\varepsilon_A(\lambda)$ is extinction coefficient of acceptor.[30] The results of J(λ) is presented in (b).

Estimation of Förster distance.[30, 34] The Förster distance R_0 is the critical distance where the energy transfer rate equals the radiative decay rate of the donor. It can be calculated as

$$R_0 = \left(\frac{9000(\ln 10)\kappa_p{}^2 Q_D}{N_A 128\pi^5 n_D{}^4} I \right)^{1/6} \tag{5.12}$$

where N_A is the Avogadro constant; $\kappa_p{}^2$ is the orientation factor and is usually assumed to be 2/3 for a random distribution; Q_D is the quantum yield of the QD donor which is 0.55; n_D is the reflex index of the medium; I is the spectra overlap(see Figure A5.2b).

Estimation of the maximum coverage of lipid molecules on a single QD. For the modelling it is essential to know or at least to estimate the number N_{QD} of lipid molecules on the surface of a QD. We are not aware of any experimental evidence for this number. The core-shell-shell QDs have an average core diameter of 7.5 nm. The cores are capped by linear hydrophobic ligands with a C18 tail (2.5 nm length). This capping layer is dense only very close to the surface. Due to surface curvature of the QD, the capping density on the outside of the capping layer is less than 40% of the capping density at the QD surface. Hence, the hydrophobic double-tails of lipid molecules can easily penetrate into the capping layer. The depth of interpenetration determines the maximum number of lipids around the QD. The interpenetration depth is not known but can be estimated based on general considerations.

The upper bound for N_{QD} is reached in the situation when the hydrophobic lipid tails adsorb at the surface of the capping layer, forming a loose vesicle around the QD. The maximum coverage is reached when all lipid tails are oriented perpendicular to the QD surface (point away from the QD). Then N_{QD} is the total surface area (i.e. the area of a sphere) divided by the “lipid footprint”. The latter can be estimated as the footprint of two alkyl tails, which is approximately 0.45 nm^2. The upper bound for N_{QD} is then

$$N_{QD} < \frac{\pi\ (7.5\ nm\ +\ 2\ \times\ 2.5\ nm)^2}{0.45 nm^2} \approx 1100 \tag{5.13}$$

Now we consider the situation when lipid tails do penetrate into the capping layer. If we assume that the lipid tails do interpenetrate 20% into the capping layer,

then we have to subtract the area occupied by HDA ligand tails from the surface area of the sphere. In this case, the upper bound decreases to

$$N_{QD} < \frac{\pi\ (7.5\ nm\ +\ 2\ \times\ 0.8\ \times 2.5\ nm)^2 - \pi\left(7.5\ nm\right)^2}{0.45 nm^2} \approx 530 \qquad (5.14)$$

If the lipid tails penetrate halfway into the capping layer, then N_{QD}= 300. For the modelling in the rest of the report, an intermediate value of N_{QD}= 500 is taken. We verified that the results of the modelling do not change significantly when using a value of 300 or 900 instead. Only one parameter is sensitive to the exact value of N_{QD}: the optical constant.

Estimation of optical constant. The optical constant γ can be calculated by its definition:

$$\gamma = \frac{D_{QY} P_{TR}}{P_R} = D_{QY} \left(\frac{R_0}{r} \right)^6 \qquad (5.15)$$

where D_{QY} is the quantum yield of dye (D_{QY} = 0.2 for Cy5.5) and r is the donor to acceptor distance, which is a unknown value. According to the QD micelles structure, if r is estimated to be between 5 to 7 nm, the value of γ is between 0.28 and 2.1. On the other hand, if γ can be determined from the experiment, r can also be calculated with equation (4).

CHAPTER 6

Quantum Dot And Cy5.5 Labeled Nanoparticles to Investigate Lipoprotein Bio-interactions via Förster Resonance Energy Transfer

Abstract

The study of lipoproteins, natural nanoparticles comprised of lipids and apolipoproteins that transport fats throughout the body, is of key importance to better understand, treat and prevent cardiovascular disease. In the current study we have developed a lipoprotein-based nanoparticle that consists of a quantum dot (QD) core and Cy5.5 labeled lipidic coating. The methodology allows judicious tuning of the QD/Cy5.5 ratio, which enabled us to optimize Förster resonance energy transfer (FRET) between the QD core and the Cy5.5 labeled coating. This phenomenon allowed us to study lipoprotein-lipoprotein interactions, lipid exchange dynamics and the influence of apolipoproteins on these processes. Moreover, we were able to study HDL-cell interactions and exploit FRET to visualize HDL association with live macrophage cells.

6.1 Introduction

The development of hybrid nanostructures based on nanocrystals that are stabilized and functionalized by a biocompatible coating has seen rapid progress over the past decade.[1-7] Among the different coatings, amphiphilic polymer and lipid coatings have shown unprecedented possibilities since these can be applied in a facile fashion, allow combinations with reactive and/or functionalized amphiphilic molecules, or may be comprised of naturally occurring molecules such as phospholipids and apolipoproteins to create lipoprotein-like nanoparticles.[2] In previous studies we developed lipid-coated quantum dot technology to create targeted nanoparticles for multimodal molecular imaging in animal models of cancer and cardiovascular disease.[2,4,8] These nanoparticles are comprised of quantum dots that are stabilized by hydrophobic ligands, which are subsequently coated by a monolayer of phospholipids. Other nanocrystals that have been exploited as contrast agents for various imaging techniques using a similar lipidic coating strategy include gold,[9] iron oxide,[10] or manganese ferrite.[11] Subsequent functionalization of such lipid coated nanoparticles can be achieved by the conjugation of targeting ligands,[5,12] such as peptides,[4] or, as we have recently demonstrated, by the adsorption of apolipoproteins, such as apolipoprotein A-I (apoA-I).[2] In the latter case the general nanoparticle morphology closely resembles that of high-density lipoprotein (HDL)[13] and we have shown it to also exhibit important biological HDL functions, such as macrophage targeting[14] and the ability to induce cholesterol efflux.[2,15]

HDL, popularly known as “good cholesterol”, has a protective role in the development of cardiovascular disease,[16,17] a pathology that may ultimately result in clinical events such as myocardial infarction and stroke.[18] The study of lipoprotein biology in general, and HDL’s biology in particular, therefore is of key importance to better understand, treat and prevent cardiovascular disease and help reduce mortality and morbidity caused by this pathology.

Both the increasing interest in lipid-coated nanocrystals and the need to better understand HDL biology in detail inspired us to develop a hybrid nanoarchitecture that resembles HDL. The dynamics of lipid exchange and interactions with cells can be studied with Förster resonance energy transfer (FRET) between the quantum dot core and dye-labeled lipids in the coating. In recent reports FRET between quantum dots and organic fluorophores has been exploited to study fundamental and biological processes,[19-22] but this phenomenon has also been applied to create biosensors[23] and imaging probes.[24] In the majority of these studies the organic fluorophores were adsorbed at the surface of QDs via proteins,[25] pep-

tides[26] or polymers.[27,28] We sought to develop nanotechnology based on lipid-coated nanocrystals that allows an easier and more precise tuning of the QD/dye ratio to optimize FRET and enables a detailed investigation of the lipid exchange dynamics of HDL nanoparticles with their surroundings as well as their biological interaction with cells.

6.2 Experimental

Materials Myristoyl hydroxy phosphatidylcholine (MHPC) distearoyl phosphoethano- lamine-N-[methoxy(polyethylene glycol)-2000] ammonium salt (PEG-DSPE), dim yristoyl phosphoethanolamine (DMPE) and dimyristoyl phosphoethanolamine-N-(lissamine rhodamine B sulfonyl) ammonium salt (Rhod-DMPE) were all purchased from Avanti Polar Lipids and used as received. The Cy5.5 NHS ester was purchased from Amersham Biosciences (Piscataway, NJ). Cell culture supplies were purchased from Invitrogen (Carlsbad, CA).

Synthesis and optical characterization of dual labeled QD core HDL nanoparticles. Oleic acid capped core−shell−shell (CSS) QDs were synthesized as we described previously.[29] 10 mg of MHPC lipids were dissolved in a 1 ml 20:1 chloroform: methanol solvent mixture. Cy5.5 labeled lipid was added to this mixture at various mass percentages of 0%, 0.125%, 0.25 %, 0.5 %, 1 % and 2 %. 1 nmol of QDs were suspended in chloroform and mixed with the lipid solution. The resulting mixture was slowly added dropwise to 1.5 ml of heated (80 °C) deionized water under constant stirring. Subsequently, the crude product was centrifuged for 8 min at 3000 rpm, to remove aggregates and unsuspended nanoparticles. Apo-A1 lipoprotein was added at a 1:2.5 ratio by mass to the total lipid and the solution was incubated overnight to allow incorporation of the protein into the lipid corona, to create HDL-like nanoparticles. To purify the solution and remove any ‘empty’ HDL formed, i.e. HDL without QD cores, the sample was centrifuged in 30% potassium bromide according to the Havel et al. lipoprotein separation method.[30] Lastly, the deionized water was exchanged for phosphate buffered saline (PBS). A more extensive description of the synthesis of nanocrystal-HDL was reported previously.[31]

Synthesis of Cy5.5-DMPE. Cy5.5-labeled DMPE was synthesized by in a modification of a recently reported method4. Typically, 9 mg of DMPE was dissolved in 2 ml of a 4:1 chloroform:methanol solvent mixture to form solution A. 5 mg Cy5.5 mono NHS ester was dissolved in 1 ml of a 1:4 DMSO:chloroform solvent mixture,

to make solution B. 10 µl of triethylamine was mixed with 90 µl of the 1:4 DMSO:chloroform solvent mixture to make solution C. Solution A, B and 10 µl of solution C were mixed to form solution D, which was stirred overnight at 4 °C under nitrogen atmosphere. 7mg of stearoyl-hydroxy phosphatidylcholine was dissolved in 4:1 chloroform:methanol and added to solution D. The solvents were removed from this mixture to form a lipid film, which was hydrated with 5 ml of deionized water. 50 kDa Vivaspin molecular weight cut-off tubes were used to separate unconjugated Cy5.5 mono NHS ester from Cy5.5 conjugated lipid micelles, by washing 5 times with water until the filtrate was completely colorless. The Cy5.5 micelles were subsequently freeze dried for 3 days to remove all water, after which they were dissolved in a 4:1 chloroform:methanol mixture such that the concentration of Cy5.5 was 1 µmol/ml.

Lifetime measurements. Photoluminescence lifetime measurement were obtained by time-correlated single-photon counting. The setup consisted of a pulsed PicoQuant laser (2.5MHz, wavelength 406 nm), in combination with a monochromator (1350 lines/mm blazed at 630nm), a Hamamatsu photo-multiplier tube (H5738P-01), and a Time Harp 200 computer card.

Acquisition of emission spectra QDs and Cy5.5. Emission spectra were recorded using a 450W Xe lamp as excitation source and a double grating 0.22 m SPEX monochromator (of a SPEX Fluorolog) to select the excitation wavelength of 406 nm. Emission was collected through an optical fiber leading to a 0.3 m monochromator (150 lines/mm, blazed at 550 nm) and detected by a liquid nitrogen cooled Princeton Instruments CCD camera (1024 × 256 pixels). Absorption spectra were measured on a Perkin-ELMER Lambda 16 UV/VIS spectrometer.

Fluorescence imaging of HDL nanoparticle samples. Fluorescence imaging of black 96 wells plate that contained 100 µl volumes of each of several differently labeled diluted HDL samples was performed using the IVIS Imaging System 200 (Xenogen, Alameda, CA). In the first QD setup the samples were imaged using an excitation passband of 445 – 490 nm, while applying an emission passband of 610 – 630 nm. In the Cy5.5 setup a dedicated filter set was applied to directly visualize Cy5.5, i.e. an excitation bandpass filter of 615 – 665 nm and an emission bandpass filter of 695 – 770 nm. The FRET setup had the QD excitation bandpass filter of 445 – 490 nm and the Cy5.5 emission bandpass filter of 695 – 770 nm.

Lipid-exchange measurements. For time-dependent photoluminescence measurements, a 450 W Xe lamp was used as light source and a double grating 0.22 m SPEX monochromator was used to select the excitation wavelength (400 nm).

Emission was collected by an optical fiber leading to a 0.25 m monochromator (150 lines/mm, blazed at 650 nm) and detected by a liquid nitrogen cooled Princeton Instruments CCD camera. The acquisition time for each measurement was 0.4 s. For the first 30 s after injection, emission spectra were recorded at a rate of 1 spectrum/s, which was followed by a 30 min measurement with a 10 s interval. To avoid photobrightening of QDs a synchronized shutter was used to block the excitation light outside the acquisition time windows. Measurements were performed using a quartz cuvette, and the temperature was controlled by flowing fluid through the sample holder using a thermo-circulator.

Cell culturing. THP-1 cells were obtained from ATCC (Catalog no. TIB-202TM ; Manassas, VA, USA) and cultured in a 5% CO2 environment according product information using RPMI1640, supplemented with 10% FCS (Gibco,InVitrogen, Paisley, UK). J774A.1 cells were obtained from ATCC (Catalog no. TIB-67TM; Manassas, VA, USA) and cultured in a 5% CO2 environment according product information using DMEM, supplemented with 10% FCS (Gibco,InVitrogen, Paisley, UK).

Fluorescence microscopy of live macrophage cells. J774A.1 macrophage cells were cultured in glass-bottom dishes and imaged using an inverted microscope (Diaphot500, Nikon) equipped with a CCD-camera (Cascade680, RoperScientific) operating at an frame integration time of 100 ms. A 60x/1.2NA water immersion objective (Nikon) was used in all imaging experiments. This resulted in images of 80x60µm (0.13µm/pixel). A standard mercury arc-lamp was used as an excitation source. For imaging the QD fluorescence a 380-420nm bandpass excitation filter and a 590-650nm bandpass emission filter were used; Cy5.5 fluorescence was imaged using a 645-665 bandpass excitation and a 670-750 emission filter. The FRET experiments were carried out using a 380-420 nm bandpass excitation filter and a 700 nm longpass emission filter. During the measurements the cells were kept at 37 °C in a stage-top incubator (Tokai Hit) at a 5% CO_2 atmosphere.

6.3 Results and discussion

In the present study we have developed FRET nanoprobes, based on the above-mentioned lipid-coated QD nanoparticle technology, which closely mimics HDL. This nanoparticle has a FRET donor QD in its core and the near infrared fluorescent dye Cy5.5 FRET acceptor in its lipid corona. The incorporation of the dye in the nanoparticle's lipid corona was facilitated by its conjugation to DMPE, a phospholipid that has an amine group available. Exceptionally stable CdSe-CdS-ZnS core−shell−shell (CSS) QDs[29] were synthesized and coated with an appropriate mixture of Cy5.5 labeled and unlabeled phospholipids using methods we have described previously.[2,4,29] The resulting nanoparticles consist of one QD core per HDL particle and are highly stable in PBS and serum. The emission spectrum of these CSS QDs and the absorption spectrum of the Cy5.5-lipids significantly overlap, which is a prerequisite for FRET. We further exploited the broad and narrow absorption bands of the QD and Cy5.5 dye, which allowed us to selectively excite the donor QDs. The amount of Cy5.5 in the coating could be easily adjusted by adding more labeled lipid to the mixture. Subsequently, apolipoprotein A-I (apoA-I) was added and left to incubate overnight, after which the product was purified to obtain single QD core and Cy5.5 labeled HDL-like nanoparticles (QD-HDL-Cy5.5), schematically depicted in Figure 6.1a.

To investigate the occurrence of FRET we acquired emission spectra of QD-HDL nanoparticles that contained varying amounts of Cy5.5 in their lipid coating. The emission spectra (Figure 6.1b), recorded for an excitation wavelength of 400 nm where the QDs absorb efficiently and the Cy5.5 dye has little or no absorbance, revealed a dramatic decrease in the QD emission intensity with an increasing amount of Cy5.5. This decrease was accompanied by an increase in the intensity of the Cy5.5 emission peak. For QD-HDL particles that contained 1% Cy5.5 labeled lipid in their coating, which corresponds on average to 3 Cy5.5 dye molecules per particle, the QD emission was almost completely quenched. These observations clearly demonstrate the occurrence of FRET from the QDs to the Cy5.5 dye molecules. To further verify that the decrease of the QD emission intensity and increase of Cy5.5 intensity was due to FRET we measured the fluorescence lifetimes of the QD emission for different samples. In Figure 6.1c the fluorescence decay curves portray a significant reduction in the QD excited state lifetime with increasing amounts of Cy5.5. The increased decay rate of the QD fluorescence observed within the first 10 ns after excitation is ascribed to energy transfer from a QD donor to a Cy5.5 dye molecule acceptor.

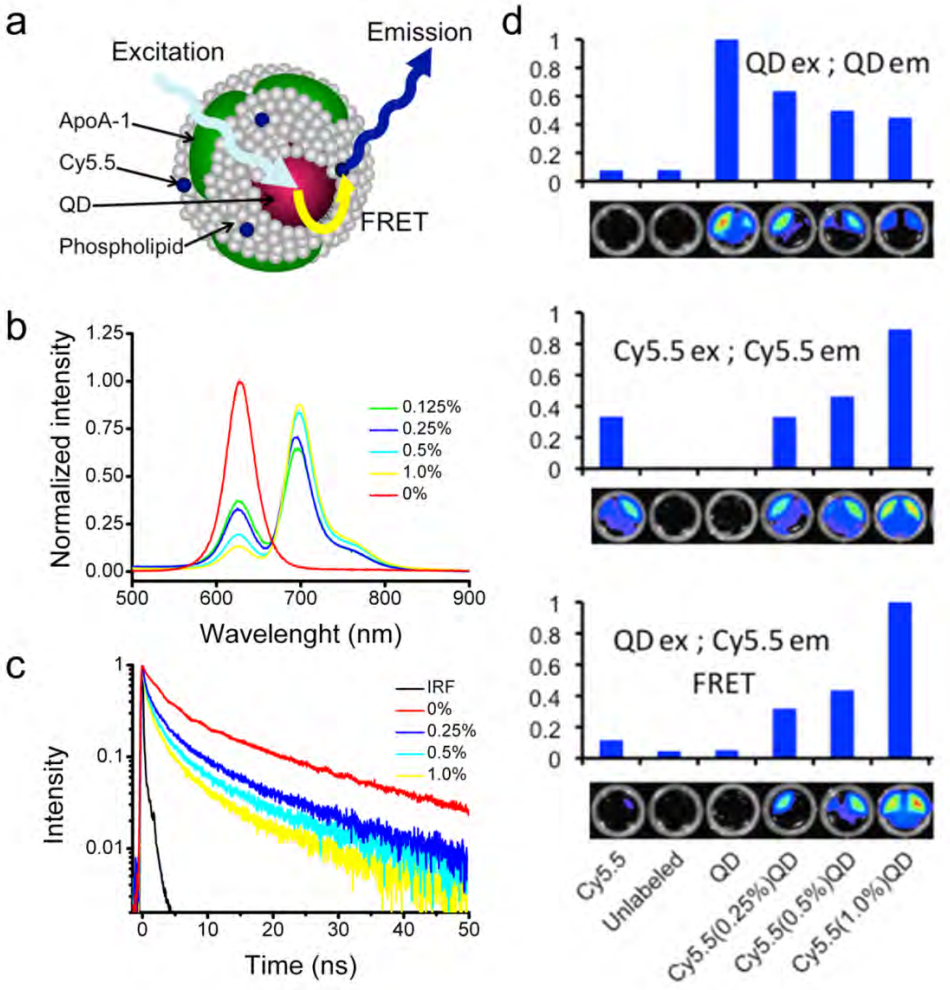

Figure 6.1. Förster resonance energy transfer (FRET) in quantum dot (QD) core high-density lipoprotein labeled with lipid-conjugated fluorophore. (a) Schematic representation of a quantum dot core and Cy5.5-lipid dual labeled high-density lipoprotein (QD-HDL-Cy5.5) nanoparticle. (b) Emission spectra of QD-HDL with varying amounts of Cy5.5-lipid for excitation at 406 nm. (c) Fluorescence decay curves of the QD emission (620 nm, excitation at 406 nm) for QD-HDL with varying amounts of Cy5.5-lipid. The contribution of the instrument response function (IRF) is neglectable. (d) Fluorescence images of different HDL preparations acquired with a QD excitation and emission passband (top), a Cy5.5 excitation and emission passband (middle) and a QD excitation and Cy5.5 emission passband (FRET setup).

Near infrared fluorescence (NIRF) imaging is a semi quantitative imaging modality [32] that is applied to visualize NIRF probes in cells and small laboratory animals, primarily mice. This imaging method is fast, sensitive and allows multiplex imaging, i.e. the visualization of multiple species.[33,34] In addition to studying particle-particle and particle-cell interactions, the Cy5.5 coated QD HDL nanoparticle may also be exploited as a NIRF probe that can be excited by a broad wavelength range via the QD, but exhibits the typical Cy5.5 NIRF emission. We tested the ability of fluorescence imaging to observe FRET in samples that contained QD core HDL with varying amounts of Cy5.5 labeled lipids. To that end we applied three different filter set combinations on a black wells plate that contained 100 µl of differently labeled diluted (~1 µMol lipid) HDL samples and measured the photon counts. These were normalized to the maximum value for a certain filter set. In the first QD setup we aimed to visualize the QD excitation and emission by exciting the samples with an excitation passband of 445 – 490 nm, while applying an emission passband of 610 – 630 nm. In the second Cy5.5 setup a dedicated filter set was applied to directly visualize Cy5.5, i.e. an excitation passband of 615 – 665 and an emission passband of 695 – 770 nm. The third setup, which we will refer to as the FRET setup, had the QD excitation passband and the Cy5.5 emission passband. In the QD setup we observed signal from all the HDL samples that contained a QD core, but quenching from the HDL samples that were also labeled with Cy5.5 was clearly observed (Figure 6.1d, top). The Cy5.5 setup noticeably showed an increasing photon count for samples that contained a higher Cy5.5 content. In the FRET setup energy transfer occurred for all the dual labeled samples, with the highest photon count for the sample that contained 1% Cy5.5. Altogether, the experiments presented in Figure 6.1 convincingly demonstrate the occurrence of FRET in our dual labeled HDL nanoparticle. Below we will demonstrate how changes in the FRET can be used to probe lipid exchange between nanoparticles and to study the association of the lipoprotein nanoparticles with cells.

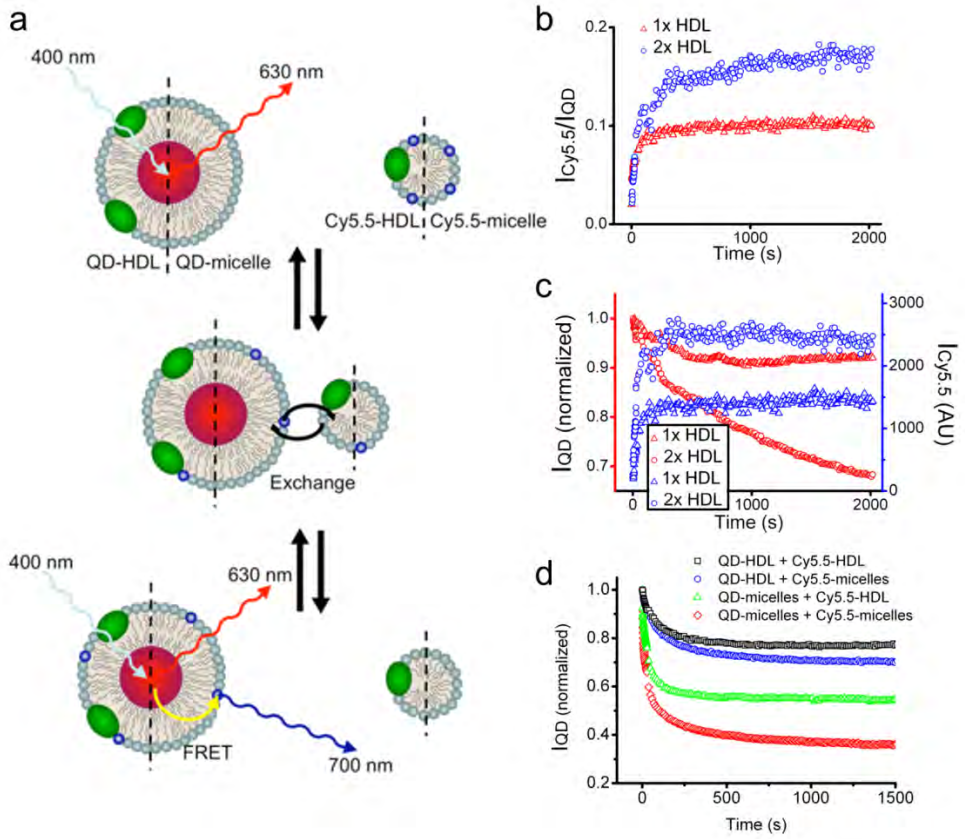

Figure 6.2. Lipid-exchange between different types of lipidic nanoparticles monitored by optical techniques. (a) QD-HDL (or QD-micelle) mixing with HDL-Cy5.5 (or Cy5.5-micelle) results in the occurrence of FRET after Cy5.5-lipids exchange. (b) Intensities of the Cy5.5 emission divided by the intensity of the QD emission ($I_{Cy5.5}/I_{QD}$) for QD-HDL samples that were mixed with Cy5.5 labeled HDL at two different concentrations. (c) The individual intensities $I_{Cy5.5}$ and I_{QD} of the data presented in (b). (d) Temporal course of I_{QD} after mixing QD-HDL and Cy5.5-HDL, QD-HDL and Cy5.5-micelles, QD-micelles and Cy5.5-HDL and QD-micelles and Cy5.5-micelles.

HDL, which measures 7-13 nm in diameter, is comprised of a fatty core of triglycerides and cholesteryl esters that is coated and stabilized by phospholipids and apolipoproteins.[35] Besides HDL, many other lipoprotein classes[36] exist and several studies have shown that they can take up cholesterol[37] and vividly exchange components, including the phospholipids.[38] Our FRET QD-HDL-Cy5.5 nanoparticle is very well suited to study lipid-exchange, since the area under the emission

peaks in the spectrum of the sample depends on the amount of Cy5.5-lipid present in the particle's corona, and changes in the emission spectra can be studied with a high temporal resolution of less than 0.4 s. This implies that when a lipid-coated QD sample, which does not contain Cy5.5-lipids, is mixed with lipid nanoparticles that do contain Cy5.5-lipids, and lipid-exchange occurs, the areas under the emission spectra of the QD and Cy5.5 change. In Figure 6.2a different exchange processes are schematically depicted. In Figure 6.2b the time evolution of the integrated intensity of the Cy5.5 emission divided by the integrated intensity of the QD emission ($I_{Cy5.5}/I_{QD}$) is plotted for QD-HDL samples that were mixed with Cy5.5 labeled HDL, or with Cy5.5 labeled micelles, at the same concentrations of Cy5.5. This ratio was observed to gradually increase after mixing, eventually reaching an equilibrium value. In addition, we found the equilibrium $I_{Cy5.5}/I_{QD}$ ratio to be higher when the mixing was done at a higher Cy5.5-HDL concentration. This implies that in the latter case more Cy5.5 labeled lipid is transferred to the QD core HDL nanoparticles. In Figure 6.2c the intensities of Cy5.5 and QD are individually depicted, showing that the trends observed in Figure 6.2b result from a simultaneous decrease in the QD emission intensity and increase in the Cy5.5 emission intensity.

Besides the targeting function,[39,40] apoA-I is known to provide stability to the HDL lipid nanoparticle.[41] Studying exchange rates of lipids between HDL particles (and other lipidic aggregates) using the abovementioned methodology may therefore shed light on the stabilizing properties of apoA-I. To that end, we tested 4 different situations (Figure 6.2d) where 0.025 nmol/ml QD core lipid nanoparticles, either with or without apoA-I included in their lipid coating, were mixed with equimolar amounts of either HDL or micellar nanoparticles that contained Cy5.5 labeled lipids. For reasons of clarity we solely present the intensity of the QD emission for the exchange data in Figure 6.2d. Mixing HDL-like nanoparticles that are both functionalized with apoA-I resulted in the slowest exchange rates while mixing apoA-I functionalized with unfunctionalized nanoparticles showed intermediate exchange rates. The fastest exchange rates were observed when lipid-coated QDs were mixed with Cy5.5-micelles. In addition, we observed that the exchange rates were temperature dependent. A strong increase in exchange rate is observed between 6 and 37 °C (Appendix Figure A6.1). The experiments confirm that apoA-I has stabilizing properties,[42-44] since lipid-exchange was significantly decreased for the lipid nanoparticles that were functionalized with apoA-I, i.e. HDL nanoparticles, as compared to the lipid nanoparticles without this apolipoprotein.

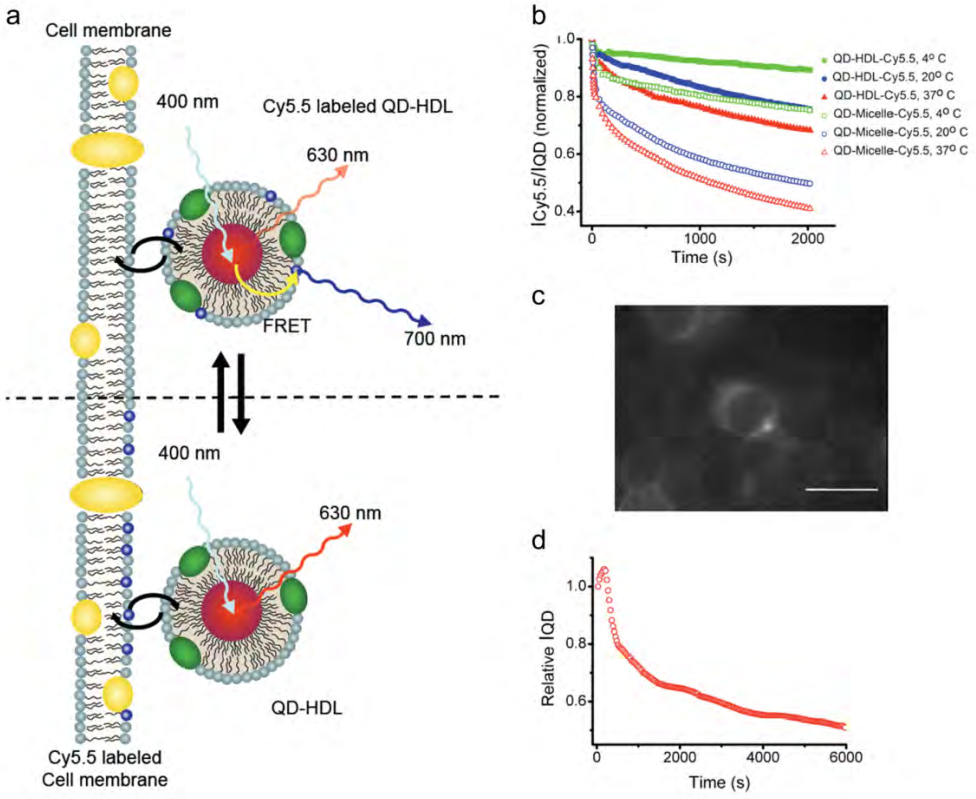

Figure 6.3. Lipid-exchange between lipid nanoparticles and cell membrane. (a) Schematic representation of the QD-HDL-Cy5.5 exchanging Cy5.5-lipids with the cell membrane and the effect on FRET. (b) $I_{Cy5.5}/I_{QD}$ of QD-HDL and QD-micelle samples that were mixed with THP-1 macrophage cells at different temperatures. (c) Fluorescence microscopy image of THP-1 cells that were incubated with QD-HDL-Cy5.5 showing the incorporation of Cy5.5-lipids in the cell membrane. (d) I_{QD} of QD-HDL that were mixed with THP-1 cells that were pre-labeled with Cy5.5-lipids.

The most important mechanism through which HDL exerts its protective role against cardiovascular disease is the removal of excess cholesterol from peripheral cells, especially from lipid-laden macrophages, and its transport to the liver, a process referred to as reverse cholesterol transport.[14,45] FRET measurements can also be applied to investigate interactions between HDL and cells, as schematically illustrated in Figure 6.3a. To that aim we incubated THP-1 macrophages, a cell line

that grows in suspension and does not adhere, with QD-HDL-Cy5.5. A decrease in $I_{Cy5.5}/I_{QD}$ was observed (Figure 6.3b) for dual labeled lipid nanoparticles, indicative of Cy5.5-lipids exchanging with the cell membrane. A noticeable difference was observed between the apoA-I stabilized HDL particles and the lipid particles that were not functionalized with apoA-I. The much slower exchange observed for the apoA-I particles confirms its stabilizing function. Fluorescence microscopy images of THP-1 macrophages that were incubated with QD-HDL-Cy5.5 and Cy5.5 labeled micelles are presented in Figure 6.3c and Appendix Figure A6.2, respectively. These data corroborated our hypothesis that the Cy5.5 labeled lipids transferred to the cell membrane, but we cannot rule out the occurrence of other associative processes such as uptake. Alternatively, we pre-labeled THP-1 macrophages with Cy5.5-lipid micelles overnight and subsequently incubated with QD core HDL that was not labeled by Cy5.5-lpids. After mixing, we observed a temporal decrease of I_{QD}, indicative for lipid-exchange from the cells to the nanoparticle (Figure 6.3d). These results confirm the vivid exchange of lipoprotein components with cells.

Lastly, we performed a proof-of-principle study where we aimed to visualize FRET of QD-HDL-Cy5.5 nanoparticles in living adhered J774A.1 macrophages via fluorescence microscopy. Such experiments can provide information about the mechanism of uptake and the intactness of the lipid nanoparticle after uptake by the cell.

First, we performed experiments where we incubated macrophages with QD-HDL-Cy5.5 and control nanoparticles for 5 min. These were subsequently washed to remove the aforementioned nanoparticles from the medium. Fluorescence microscopy images were recorded with different filter sets to directly visualize QDs and Cy5.5-lipids, as well as to visualize the occurrence of FRET, 10 min after washing the cells. Figure 6.4a presents bright field images of untreated and cells that were incubated with HDL-Cy5.5, QD-HDL and QD-HDL-Cy5.5, respectively. Cy5.5 fluorescence (Figure 6.4b) was observed in the cell membrane of cells incubated with HDL-Cy5.5 and QD-HDL-Cy5.5, confirming exchange of lipids with the cell membrane, in line with the data presented in Figure 6.3, but also inside the cell, indicative for particle uptake. QD fluorescence was observed inside cells that were incubated with QD-HDL or QD-HDL-Cy5.5 (Figure 6.4c). The QDs were most likely present in vesicular structures, i.e. endosomes. In the FRET microscopy setting we observed pronounced Cy5.5 fluorescence in cells that were incubated with QD-HDL-Cy5.5 (Figure 6.4d), confirming the occurrence of particle uptake and applicability of our FRET technology in cell fluorescence microscopy experiments. We ascribe the marginal fluorescence observed in cells incubated with HDL-Cy5.5 to direct excitation of Cy5.5, which was also observed when we directly imaged this

sample (Figure 6.1d). Additional live microscopy images of cells incubated with QD-HDL-Cy5.5 nanoparticles HDL-Cy5.5 can be found in Appendix Figure A6.3.

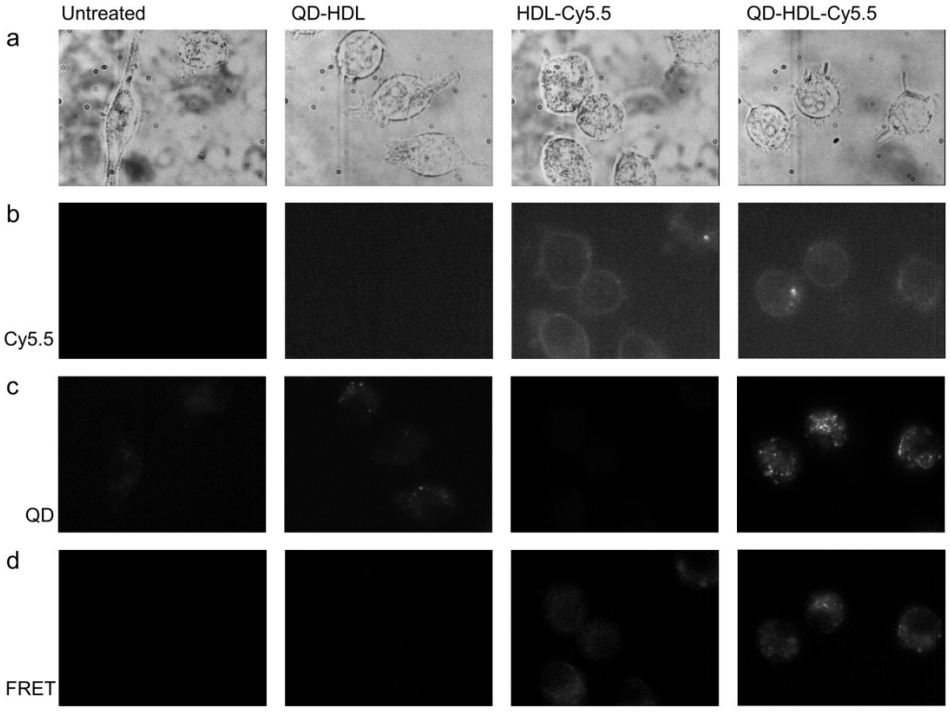

Figure 6.4. Live cell fluorescence microscopy of macrophages. (a) Brightfield images of J774A.1 macrophages that were left untreated or incubated with differently labeled HDL nanoparticles. (b) Cy5.5 fluorescence was observed in cells that were incubated with HDL-Cy5.5 or QD-HDL-Cy5.5. (c) QD fluorescence was observed in cells that were incubated with QD-HDL or QD-HDL-Cy5.5, while (d) FRET was only observed in cells that were incubated with QD-HDL-Cy5.5.

To establish the temporal evolution of QD-HDL-Cy5.5 particles we acquired fluorescence microscopy images at different time points after washing, using the different filter settings. The Cy5.5 setting allowed us to visualize the Cy5.5-labeled lipids, while the QD setting showed the location of the oleic acid coated QD cores. The FRET microscopy setting was applied to investigate the possible temporal dissociation of the nanoparticle, since the different components, i.e. fatty core and lipid/apolipoprotein corona, of HDL are known to behave differently with cells. In

general the consensus is that HDL does not enter the cell as an intact entity, but adheres at the cell surface and can exchange its fatty core. The hydrophobic cholesteryl ester core is transferred from the HDL particle to the cell via scavenger receptor BI.[46,47] In Figure 6.5a the Cy5.5 fluorescence can be observed to be primarily localized in the cell membrane, especially at early time points, becomes more diffuse in time, but remains visible. At early time points, the QD fluorescence is found primarily in the cytoplasm and becomes more homogenously distributed at later time points (Figure 6.5b). Figure 6.5a and 6.5b also show that the HDL labels do not enter the nuclei of the cells. Most interestingly, we found the Cy5.5 fluorescence to decrease over time for the FRET filter set combination, which implies that the Cy5.5 and QD label dissociate in time due to the disassembly of our QD-HDL-Cy5.5 nanoparticle once it is associated with the macrophages.

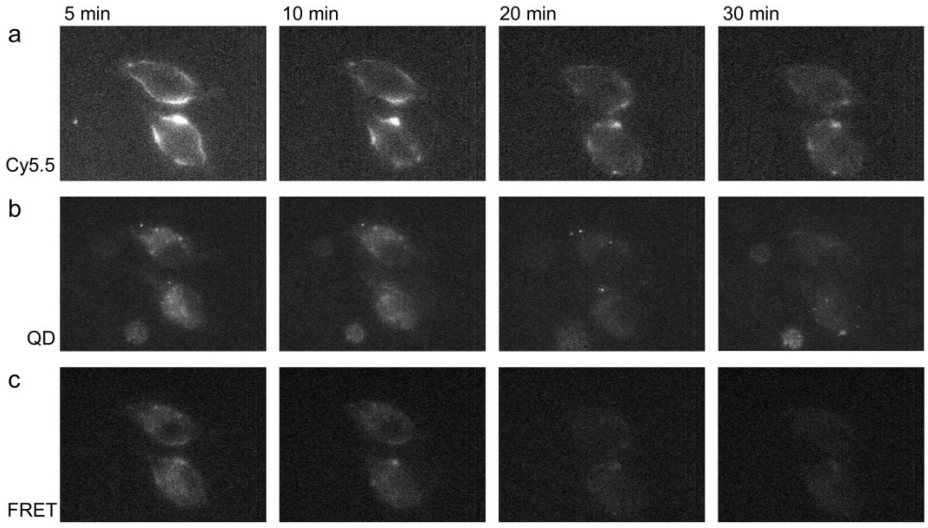

Figure 6.5. Temporal course of the fluorescence signal of macrophages incubated with QD-HDL-Cy5.5. (a) Cy5.5 fluorescence images and (b) QD fluorescence images revealed the presence of Cy5.5 and QDs at all the time points, albeit the signal intensity decreased and became more diffuse in time. (c) FRET was observed to disappear after 10 min, indicative for the dissociation of the QD and Cy5.5-lipid label.

The data presented in Figure 6.5 reveal that our nanoparticle both exchanges lipids with the cell membrane and deposits the QD core, but was also taken up by cells as an, at least partially, intact entity that disassembled in time. Additional live microscopy images of cells incubated with the control nanoparticles HDL-Cy5.5 or QD-HDL can be found in Appendix Figure A6.4. Further studies will be performed to clarify the exact mechanism of uptake, but the value of our dual labeled lipid nanoparticle FRET technology to investigate cell lipoprotein interactions was convincingly demonstrated in these live cell fluorescence microscopy experiments.

6.3 Conclusions

In the present study, we have shown QD core and Cy5.5 dual labeled HDL nanoparticles to be of great value to study lipid exchange dynamics for lipoprotein nanoparticles via FRET. We have demonstrated a methodology to follow lipid-exchange between HDL and other lipidic nanoparticles and confirmed the stabilizing features of the apoA-I.[41] In a setup where non-adherent macrophage cells were incubated with QD-HDL-Cy5.5, or Cy5.5-lipid labeled macrophages with QD-HDL, we were able to measure interactions between the cells and HDL. Lastly, we have shown the value of dual labeled HDL to visualize, using FRET fluorescence microscopy, the temporal fate of lipoproteins once associated with macrophages. It was observed that the lipids from the HDL nanoparticle exchange with the cell membrane and, once taken up by the cell, in time dissociate from the QD core. Besides labeling the lipids of QD core HDL we anticipate this FRET effect to occur if apoA-I is labeled with an organic fluorophore, thereby allowing the investigation of its dynamics and cellular fate.

Generally this technology can be applied to investigate the (exchange) behavior of a variety of lipid-coated QDs, such as PEG-lipid coated QDs that are extensively used in the field of target-specific imaging and drug delivery.[2,4,8,12,48] In addition, this technology may be applied to other lipidic nanoparticles such as nanoemulsions[49] or liposomes,[50] as well as to nanoparticles composed of block copolymers.[51] Importantly, lipid-coated and dye labeled QDs offer unique possibilities to study fundamental principles of FRET between QDs and organic fluorophores, since the nanotechnology allows facile variation of the number (or type) of dye molecules per QD as well as the manipulation of the QD-dye distance, key for efficient energy transfer, using e.g. lipids with different acyl chain lengths. Lastly, our approach may be applied to create (bio)sensors[23] using lipid-coated

QDs that are equipped with lipid-dye molecules of which the dye is cleaved, e.g. by the presence of enzymes, ions, or at certain pH.

In conclusion, lipid-coated and dye labeled QDs represent a versatile probe to study FRET as well as fundamental and biological processes via FRET, such as lipid-exchange between nanoparticles and nanoparticle uptake by cells.

References

1. Cormode, D.P., Skajaa, T., Fayad, Z.A. & Mulder, W.J. Nanotechnology in medical imaging: probe design and applications. *Arterioscler Thromb Vasc Biol* **29**, 992-1000 (2009).
2. Cormode, D.P. et al. Nanocrystal core high-density lipoproteins: A multimodal molecular imaging contrast agent platform. *Nano Lett.* **8**, 3715-3723 (2008).
3. Dubertret, B. et al. In vivo imaging of quantum dots encapsulated in phospholipid micelles. *Science* **298**, 1759-1762 (2002).
4. Mulder, W.J. et al. Quantum dots with a paramagnetic coating as a bimodal molecular imaging probe. *Nano Lett* **6**, 1-6 (2006).
5. Mulder, W.J., Strijkers, G.J., van Tilborg, G.A., Griffioen, A.W. & Nicolay, K. Lipid-based nanoparticles for contrast-enhanced MRI and molecular imaging. *NMR Biomed* **19**, 142-164 (2006).
6. Medintz, I.L., Mattoussi, H. & Clapp, A.R. Potential clinical applications of quantum dots. *Int J Nanomedicine* **3**, 151-167 (2008).
7. Bruns, O.T. et al. Real-time magnetic resonance imaging and quantification of lipoprotein metabolism in vivo using nanocrystals. *Nat Nano* **advanced online publication** (2009).
9. Prabaharan, M., Grailer, J.J., Pilla, S., Steeber, D.A. & Gong, S. Gold nanoparticles with a monolayer of doxorubicin-conjugated amphiphilic block copolymer for tumor-targeted drug delivery. *Biomaterials* **30**, 6065-6075 (2009).
10. Nitin, N., LaConte, L.E., Zurkiya, O., Hu, X. & Bao, G. Functionalization and peptide-based delivery of magnetic nanoparticles as an intracellular MRI contrast agent. *J Biol Inorg Chem* **9**, 706-712 (2004).
11. Lu, J. et al. Manganese ferrite nanoparticle micellar nanocomposites as MRI contrast agent for liver imaging. *Biomaterials* **30**, 2919-2928 (2009).
12. Mulder, W.J. et al. Nanoparticulate assemblies of amphiphiles and diagnostically active materials for multimodality imaging. *Acc Chem Res* **42**, 904-914 (2009).
13. Nichols, A.V., Krauss, R.M. & Musliner, T.A. Nondenaturing polyacrylamide gradient gel electrophoresis. *Method Enzymol.* **128**, 417-431 (1986).
14. Tall, A.R. Cholesterol efflux pathways and other potential mechanisms involved in the athero-protective effect of high density lipoproteins. *J Intern Med* **263**, 256-273 (2008).
15. Davidson, W.S. et al. The influence of apolipoprotein structure on the efflux of cellular free cholesterol to high density lipoprotein. *J. Biol. Chem.* **269**, 22975-22982 (1994).

16. Gordon, D.J. & Rifkind, B.M. High-density lipoprotein - the clinical implications of recent studies. *New Eng. J Med.* **321**, 1311-1316 (1989).
17. Stampfer, M.J., Sacks, F.M., Salvini, S., Willett, W.C. & Hennekens, C.H. A propective study of cholesterol, apolipoproteins, and the risk of myocardial infarction. *N. Engl. J. Med.* **325**, 373-381 (1991).
18. Lusis, A.J. Atherosclerosis. *Nature* **407**, 233-241 (2000).
19. Gill, R. et al. Probing biocatalytic transformations with CdSe-ZnS QDs. *J Am Chem Soc* **128**, 15376-15377 (2006).
20. Gill, R., Willner, I., Shweky, I. & Banin, U. Fluorescence resonance energy transfer in CdSe/ZnS-DNA conjugates: probing hybridization and DNA cleavage. *J Phys Chem B* **109**, 23715-23719 (2005).
21. Liu, W. et al. Compact biocompatible quantum dots functionalized for cellular imaging. *J Am Chem Soc* **130**, 1274-1284 (2008).
22. Clapp, A.R. et al. Fluorescence resonance energy transfer between quantum dot donors and dye-labeled protein acceptors. *J Am Chem Soc* **126**, 301-310 (2004).
23. Gill, R., Zayats, M. & Willner, I. Semiconductor quantum dots for bioanalysis. *Angew Chem Int Ed Engl* **47**, 7602-7625 (2008).
24. Koole, R. et al. Magnetic quantum dots for multimodal imaging. *Wiley Interdiscip Rev Nanomed Nanobiotechnol* **1**, 475-491 (2009).
25. Medintz, I.L. et al. Self-assembled nanoscale biosensors based on quantum dot FRET donors. *Nat Mater* **2**, 630-638 (2003).
26. Medintz, I.L. et al. Proteolytic activity monitored by fluorescence resonance energy transfer through quantum-dot-peptide conjugates. *Nat Mater* **5**, 581-589 (2006).
27. Jiang, G. et al. Cascaded FRET in conjugated polymer/quantum dot/dye-labeled DNA complexes for DNA hybridization detection. *ACS Nano* **3**, 4127-4131 (2009).
28. Fernandez-Arguelles, M.T. et al. Synthesis and characterization of polymer-coated quantum dots with integrated acceptor dyes as FRET-based nanoprobes. *Nano Lett* **7**, 2613-2617 (2007).
29. Koole, R.; et al. On the incorporation mechanism of hydrophobic quantum dots in silica spheres by a reverse microemulsion method. *Chem. Mater.* 2008, 20, 2503–2512
30. Havel, R. J.; Eder, H. A.; Bragdon, J. H. The distribution and chemical composition of ultracentrifugally separated lipoproteins in human serum. J. Clin. Invest. 1955, 34, 1345–1353.
31. Cormode, D. P.; et al. Nanocrystal core high-density lipoproteins: A multimodal molecular imaging contrast agent platform. *Nano Lett.* 2008, 8, 3715–3723.
32. Ntziachristos, V., Ripoll, J., Wang, L.V. & Weissleder, R. Looking and listening to light: the evolution of whole-body photonic imaging. *Nat Biotechnol* **23**, 313-320 (2005).
33. Choi, H.S. et al. Renal clearance of quantum dots. *Nat Biotechnol* **25**, 1165-1170 (2007).
34. Choi, H.S. et al. Design considerations for tumour-targeted nanoparticles. *Nat Nanotechnol* **5**, 42-47.
35. Wang, M. & Briggs, M.R. HDL: The Metabolism, Function, and Therapeutic Importance. *Chem. Rev.* **104**, 119-127 (2004).
36. Mahley, R.W., Innerarity, T.L., Rall, S.C., Jr. & Weisgraber, K.H. Plasma lipoproteins: apolipoprotein structure and function. *J Lipid Res* **25**, 1277-1294 (1984).
37. Rothblat, G.H. et al. Cell cholesterol efflux: integration of old and new observations provides new insights. *Journal of Lipid Research* **40**, 781-796 (1999).

38. Jonas, A. Interaction of bovine serum high density lipoprotein with mixed vesicles of phosphatidylcholine and cholesterol. *J Lipid Res* **20**, 817-824 (1979).
39. Vedhachalam, C. et al. ABCA1-induced cell surface binding sites for apoA-I. *Arterioscler. Thromb. Vasc. Biol.* **27**, 1603-1609 (2007).
40. Lu, R., Arakawa, R., Ito-Osumi, C., Iwamoto, N. & Yokoyama, S. ApoA-I facilitates ABCA1 recycle/accumulation to cell surface by inhibiting its intracellular degradation and increases HDL generation. *Arteriosclerosis Thrombosis and Vascular Biology* **28**, 1820-1824 (2008).
41. Frank, P.G. & Marcel, Y.L. Apolipoprotein A-I: structure–function relationships. *J. Lipid Res.* **41**, 853-872 (2000).
42. Tall, A.R., Small, D.M., Deckelbaum, R.J. & Shipley, G.G. Structure and thermodynamic properties of high density lipoprotein recombinants. *J Biol Chem* **252**, 4701-4711 (1977).
43. Pownall, H.J., Massey, J.B., Kusserow, S.K. & Gotto, A.M., Jr. Kinetics of lipid--protein interactions: interaction of apolipoprotein A-I from human plasma high density lipoproteins with phosphatidylcholines. *Biochemistry* **17**, 1183-1188 (1978).
44. Frank, P.G. & Marcel, Y.L. Apolipoprotein A-I: structure-function relationships. *J Lipid Res* **41**, 853-872 (2000).
45. Rye, K.-A. & Barter, P.J. Antiinflammatory actions of HDL: a new insight. *Arterioscler. Thromb. Vasc. Biol.* **28**, 1890-1891 (2008).
46. Acton, S. et al. Identification of scavenger receptor SR-BI as a high density lipoprotein receptor. *Science* **271**, 518-520 (1996).
47. Rodrigueza, W.V. et al. Mechanism of scavenger receptor class B type I-mediated selective uptake of cholesteryl esters from high density lipoprotein to adrenal cells. *J Biol Chem* **274**, 20344-20350 (1999).
48. van Tilborg, G.A. et al. Annexin A5-conjugated quantum dots with a paramagnetic lipidic coating for the multimodal detection of apoptotic cells. *Bioconjug Chem* **17**, 865-868 (2006).
49. Lanza, G.M. et al. Nanomedicine opportunities for cardiovascular disease with perfluorocarbon nanoparticles. *Nanomedicine (Lond)* **1**, 321-329 (2006).
50. Torchilin, V.P. Recent advances with liposomes as pharmaceutical carriers. *Nat Rev Drug Discov* **4**, 145-160 (2005).
51. O'Reilly, R.K., Hawker, C.J. & Wooley, K.L. Cross-linked block copolymer micelles: functional nanostructures of great potential and versatility. *Chem Soc Rev* **35**, 1068-1083 (2006).

Appendix 6.1 Supporting Figures

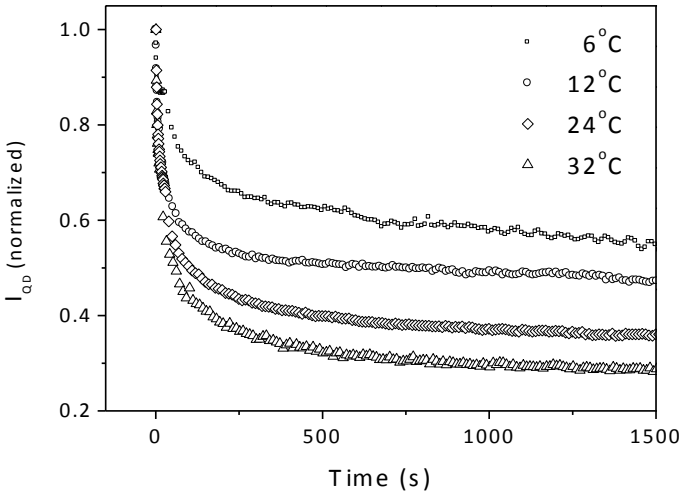

Figure A6.1. Temporal course of I_{QD} after mixing QD-micelles and Cy5.5-micelles at different temperatures.

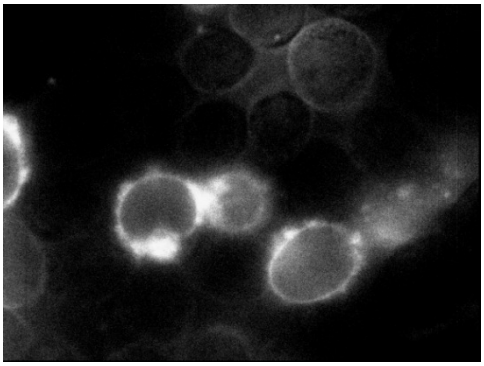

Figure A6.2. Fluorescence microscopy of non-adherent cells incubated with Cy5.5-micelles.

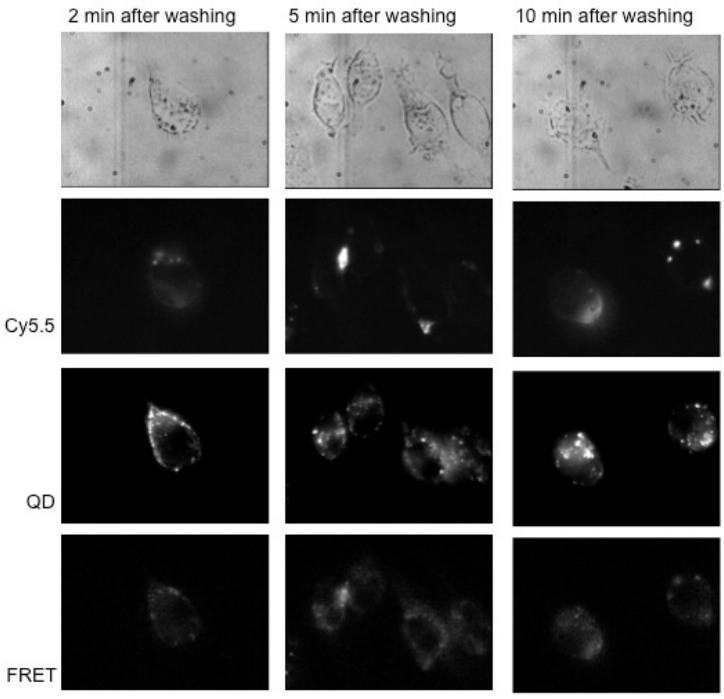

Figure A6.3. Additional live fluorescence microscopy images recorded using different filter sets of adhered macrophage cells incubated with QD-HDL-Cy5.5.

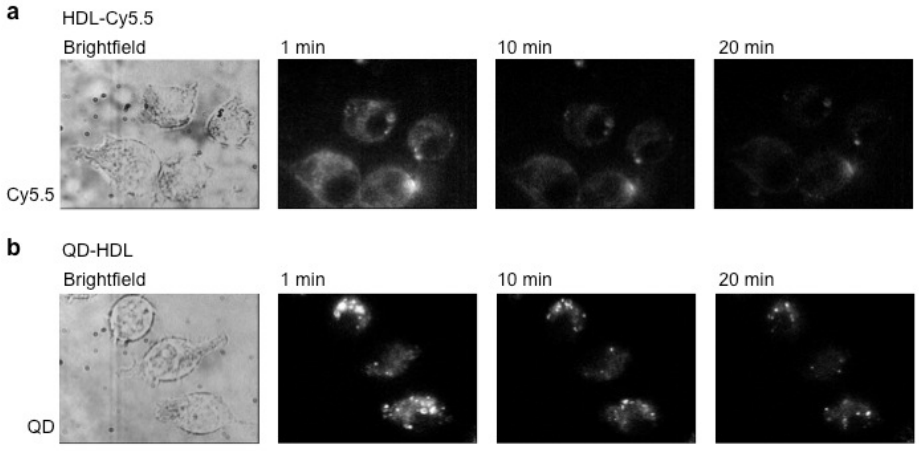

Figure A6.4. Live fluorescence microscopy images of adhered macrophage cells incubated with Cy5.5-HDL or QD-HDL using appropriate filter sets at different time points.

CHAPTER 7

In Vivo Near-infrared FRET Imaging of Nanoparticle Accumulation and Dissociation Kinetics in Tumour-bearing Mice

7.1 Introduction

In the last two decades self-assembled lipidic nanoparticles (SALNPs) have been shown to be broadly applicable as intravenously injectable agents for biomedical purposes.[1-5] SALNPs can serve as delivery vehicles for a wide variety of drugs, ranging from cytostatic agents to small interfering RNAs (siRNA) and proteins, and as molecular imaging probes. Here, we show the dissociation and tumour accumulation dynamics of dual labeled near infrared (NIR) quantum dot core SALNPs in a mouse model upon intravenous administration. Using advanced *in vivo* fluorescence energy transfer imaging techniques, we observed swift exchange with plasma protein components in the blood and progressive SALNP dissociation and subsequent trafficking of individual SALNP components following tumour accumulation. Our results suggest that upon intravenous administration SALNPs quickly transform, which may affect their functionality. The presented technology provides a modular *in vivo* tool to visualize SALNP behavior in real time and may contribute to improving the therapeutic outcome or molecular imaging signature of SALNPs.

Since their introduction by Dubertret and colleagues,[6] hybrid SALNPs that consist of a nanocrystal core covered by a self-assembled lipid-coating have been widely explored as imaging agents as many nanocrystals exhibit unique diagnostic features.[1,7] These hybrid SALNPs possess unprecedented possibilities with respect to their multifunctionality, potential for derivatization and biocompatibility, as well as to serve as drug targeting vehicles.[5, 8]

The flexibility and versatility of SALNPs derive from their self-assembled nature, which allows facile inclusion and exchange of functional components as well as fine-tuning of composition. Despite their widespread application in *in vivo* studies, primarily for preclinical cancer diagnosis and therapy,[5, 9] studies that address the dissociation kinetics of self-assembled nanoparticles, including SALNPs, after intravenous administration are scarce.[10] However, in order to maintain their functionality and fulfill their targeting purpose, the integrity of the assembled nanoparticle structure is crucial. Upon intravenous administration (Figure 7.1, I), SALNPs are initially exposed to plasma proteins, lipoproteins and circulating cells (Figure 7.1, II).[10-12] In addition, they are exposed to the mononuclear phagocyte system (MPS), i.e. splenic phagocytic cells and the Kupffer cells of the liver (Figure 7.1, III).[13] After extravasation from the vasculature into e.g. the tumour interstitium (Figure 7.1, IV), facilitated by the highly permeable tumour vasculature, nanoparticles may interact with components of the extracellular matrix, tumour associated macrophages and/or tumour cells.[14] Finally, upon their dissociation and draining into the lymphatic system, nanoparticles or nanoparticle components may be retained by lymphocytes (Figure 7.1, V).[15, 16]

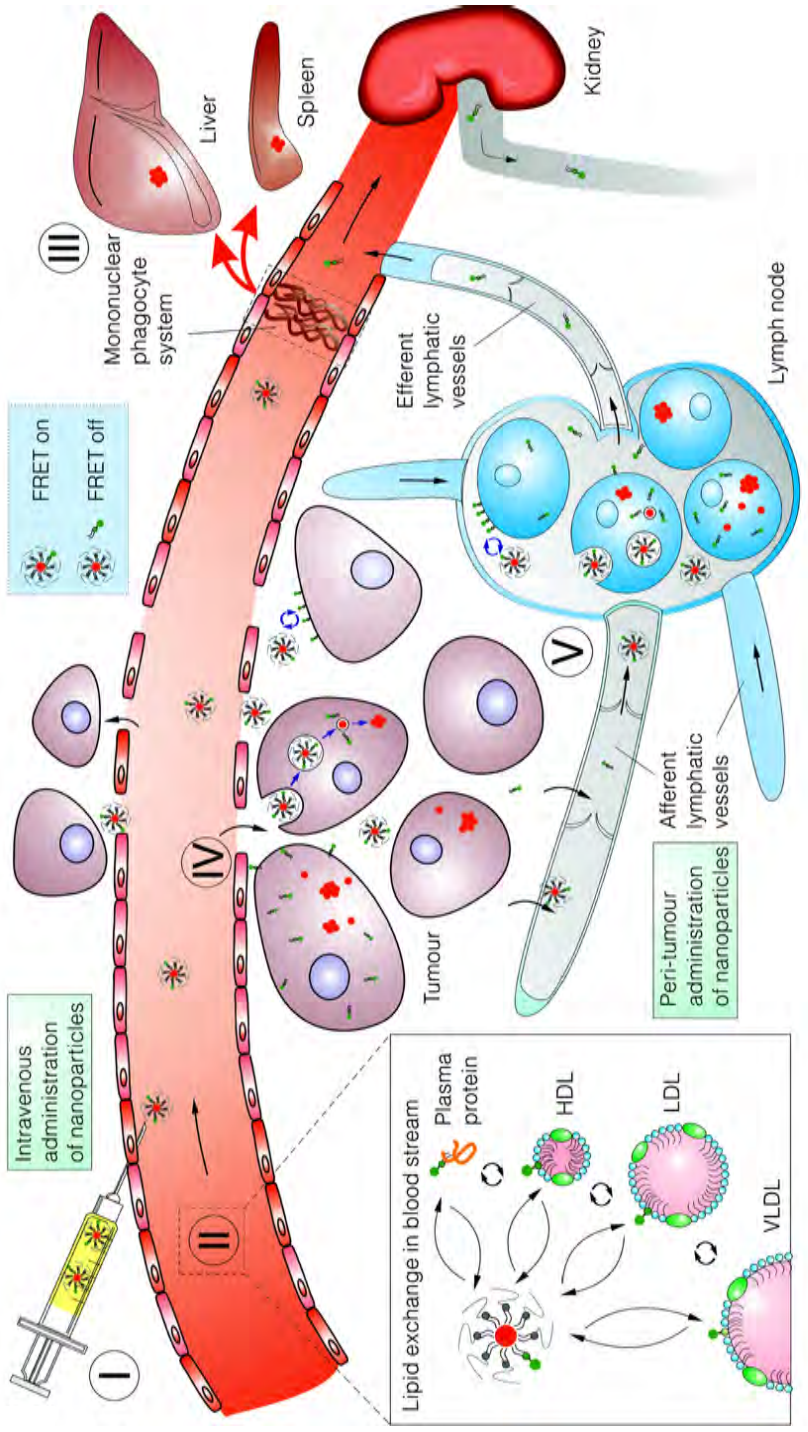

Figure 7.1. Schematic illustration of the blood circulation, dissociation dynamics, tumour accumulation, and trafficking of self-assembled nanoparticles upon intravenous administration(I) in a tumour-bearing mouse. Several distinct compartments include the blood (II), the tumour (IV, interstitium), lymphatics and lymph nodes (V), and clearance organs of the mononuclear phagocyte system (III).

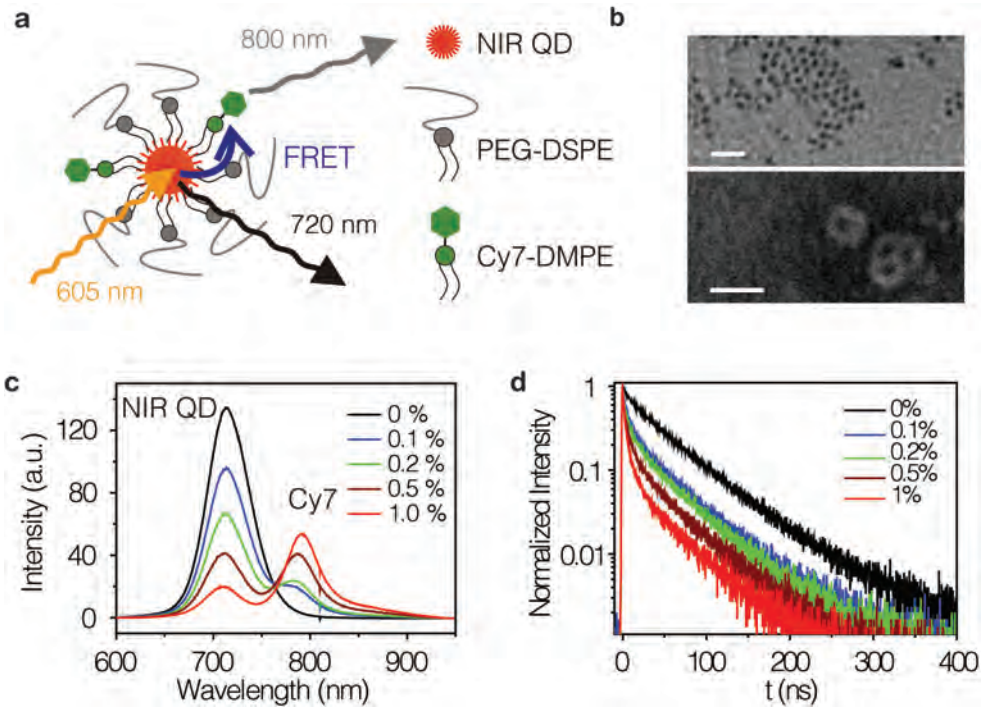

Figure 7.2 Design and characterization of FRET nanoparticles. **a.** Schematic structure of a self-assembled lipid-nanoparticle that consists of a near infrared quantum dot core covered by a self-assembled lipid-coating that is composed of Cy7-labeled and PEGylated lipids (QD710-Cy7-PEG). **b**, TEM images of QD710-Cy7-PEG with (lower) and without negative staining (upper). Both scale bars are 20 nm. **c**, Emission spectra of QD710-Cy7-PEG nanoparticles in PBS with different percentages of Cy7-lipids in the lipid corona. $\lambda_{Exc} = 500$ nm. At increasing content of Cy7-lipids, the QD emission decreased dramatically, while Cy7 emission increased correspondingly, confirming the occurrence of FRET from the QD cores to the Cy7 dyes in the corona. **d**, Corresponding QD emission decay curve.

7.2 Results and discussion

In a previous study, we have successfully studied the dynamics of lipoprotein interactions *in vitro* using quantum dot (QD) and Cy5.5 dual labeled nanoparticles using Förster resonance energy transfer (FRET) principles.[17] In the current study we further developed this technology to monitor these processes in real time by *in vivo* fluorescence imaging techniques. To that end we advanced the design of our dual labeled nanoparticle by tuning its optical features to the near infrared (NIR). Highly efficient and air-stable CdTe/CdSe/CdS/ZnS core/multi-shell QDs were synthesized to serve as a FRET donor. Their emission band was tuned to centre at 710 nm (Experimental section). These QDs were coated by a PEGylated self-assembled lipid monolayer,[6] and the dye-lipids incorporated in this nanoparticle corona functioned as 800 nm emitting FRET acceptors. The resulting nanoparticle (QD710-Cy7-PEG) is schematically presented in Figure 7.2a. Negative staining transmission electron microscopy (TEM) images confirmed a lipid corona covering a single QD nanocrystal (Figure. 7.2b). The occurrence of FRET was confirmed by measuring emission spectra of a series of these particles containing varying amounts of Cy7-lipids. As plotted in Figure 7.2c, with increasing Cy7-lipid, the QD emission at 710 nm decreased, while the dye emission at 800 nm increased correspondingly. We further measured the QD emission lifetime of these samples and observed a decrease in lifetime, which corroborated that the above intensity changes were due to FRET (Figure 7.2d).[18, 19]

The large spectral separation between the QD and Cy7-lipid enables us to trace the individual nanoparticle components simultaneously, while FRET between the QD core and the Cy7-lipid allows sensitive and semi-quantitative monitoring of the dissociation of the lipid corona from the QD core. To test the possibility of studying this FRET principle in an *in vivo* pilot experiment, QD710-Cy7-PEG was subcutaneously injected into the dorsal side of nude mice. Similar to *in vitro* conditions,[17] dissociation of Cy7-lipids could be directly detected as an increase in QD intensity and simultaneous decrease of FRET intensity (Appendix Figure A7.1).

Subsequently, nude mice bearing HCT116 colon carcinoma on their flank were intravenously administered with either FRET QD710-Cy7-PEG or control QD710-PEG, and subjected to NIR fluorescence imaging. FRET QD710-Cy7-PEG accumulation in the tumour was observed as early as 30 minutes post administration (Figure 7.3a). Region of interest (ROI) analyses of the tumours revealed different dynamics for the different components (Figure 7.3b). For control QDs (QD710-PEG), the signal kept increasing for about 2 h, and then slowly declined over 48 h. However, for the dual labelled FRET QD710-Cy7-PEG, the QD signal increased

much faster in the initial 2 h and kept rising even past 24 h. This initial faster increase was indicative of the disassociation of Cy7-lipids from the nanoparticle, which caused dequenching of QD emission. The subsequent gradual elevation of QD emission from the tumour by far exceeded the blood presence of the nanoparticles, which we established to have about a one-hour circulation half-life. Conversely, after an initial increase, the Cy7 signal started to decrease after 2 h and gradually vanished over 48 h. A similar pattern was observed for the FRET intensity (Figure 7.3a,b), which confirmed the Cy7-lipid dissociation from the nanoparticles after tumour accumulation.

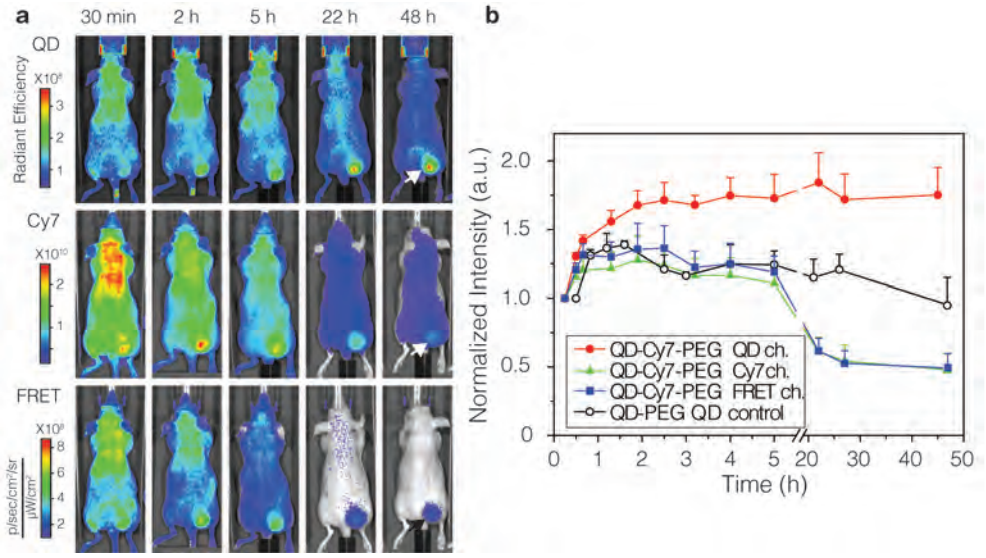

Figure 7.3. a, Representative *in vivo* NIR fluorescence images of a tumour bearing mouse injected with 100 pmol/g FRET particles QD710-Cy7-PEG at 30 min, and 2, 5, 22, and 45 h post-injection. Tumour mice injected with 100 pmol/g QD710-PEG nanoparticles containing no Cy7-lipids were used as QD control. Fluorescent signal was collected using three optical filters settings: QD (λ_{Exc} = 605 ± 18 nm, λ_{Em} = 720 ± 10 nm), Cy7 (λ_{Exc} =745± 18 nm, λ_{Em} = 800 ± 10 nm) and FRET (λ_{Exc}= 605± 18 nm, λ_{Em}= 800 ± 10 nm). **b**. The mean intensities (n=5 mice per group) from the tumour area (indicatad with arrows in **a**) plotted against post-injection time. QD, Cy7 and FRET intensities were from mice injected with QD710-Cy7-PEG, and QD control were from mice injected with QD710-PEG. Mice were sacrificed at 8 h (n = 3) and 48 h (n = 5) after injection and major organs were subjected to *ex vivo* fluorescence imaging.

Ex vivo NIR fluorescence imaging of organs revealed FRET QD710-Cy7-PEG to be accumulated in the tumour and major organs (liver, spleen, and kidneys). QD intensities were higher at 48 h than 8 h (Figure 7.4a-b), suggesting that the dequenching effect due to the dissociation of Cy7-lipid also occurred in these organs. As opposed to the QD intensities, Cy7 intensities in all the organs decreased from 8 h to 48 h (Figure 7.4c-d), which indicated that the Cy7-lipid had a clearly different bio-distribution compared to QDs. The presence of Cy7-lipids in the kidneys suggests trafficking of this component to the kidneys and subsequent renal clearance. Fluorescence microscopy (FM) of tumour and liver tissues revealed the QDs to be mainly present as clusters, while the Cy7-lipids were found diffusely throughout the cytoplasm (Figure 7.4e and Appendix Figure A7.2). TEM images confirmed the presence of dense QD aggregates, and additionally demonstrated that the QDs had entered cells and were mainly localized inside vesicles of tumour and liver cells (Figure 7.4f). Altogether, the *ex vivo* microscopy data corroborated the dissociation of the coating lipids from the QDs.

Tumours grown in dorsal window chambers (Appendix Figure A7.3) allowed us to study the dissociation and nanoparticle kinetics in the tumour blood vessels and in the tumour interstitium with intravital confocal laser scanning microscopy (CLSM).[14, 20] To that end 610 nm emitting QD610 and Cy5.5-lipids labelled nanoparticles (QD610-Cy5.5-PEG) were employed (see emission spectra in Figure 5.2a). Extravasation of QDs and Cy5.5-lipids from the vasculature into the tumour interstitium was clearly observed within 2 h post administration (Figure 7.5). ROI analyses of the vascular and extravascular space revealed different dynamics for the QDs and Cy5.5-lipids in both these compartments (Figure 7.6a-d). In blood vessels the Cy5.5 and FRET signal decreased more rapidly than the QD signal, indicative of nanoparticle dissociation in circulation (Figure 7.6a-b). Conversely, extravascularly the QD signal kept increasing in the first 2 hours, while the Cy5.5 and FRET intensities started to decrease after 1h. This behaviour is similar to what we observed with whole body NIR imaging (Figure 7.3b). In Figure 7.6d, an overall decrease of FRET/QD ratio confirmed the dissociation of Cy5.5-lipids from the lipid-coated QDs within the first 2 h after administration, in both the vascular and(to page140)

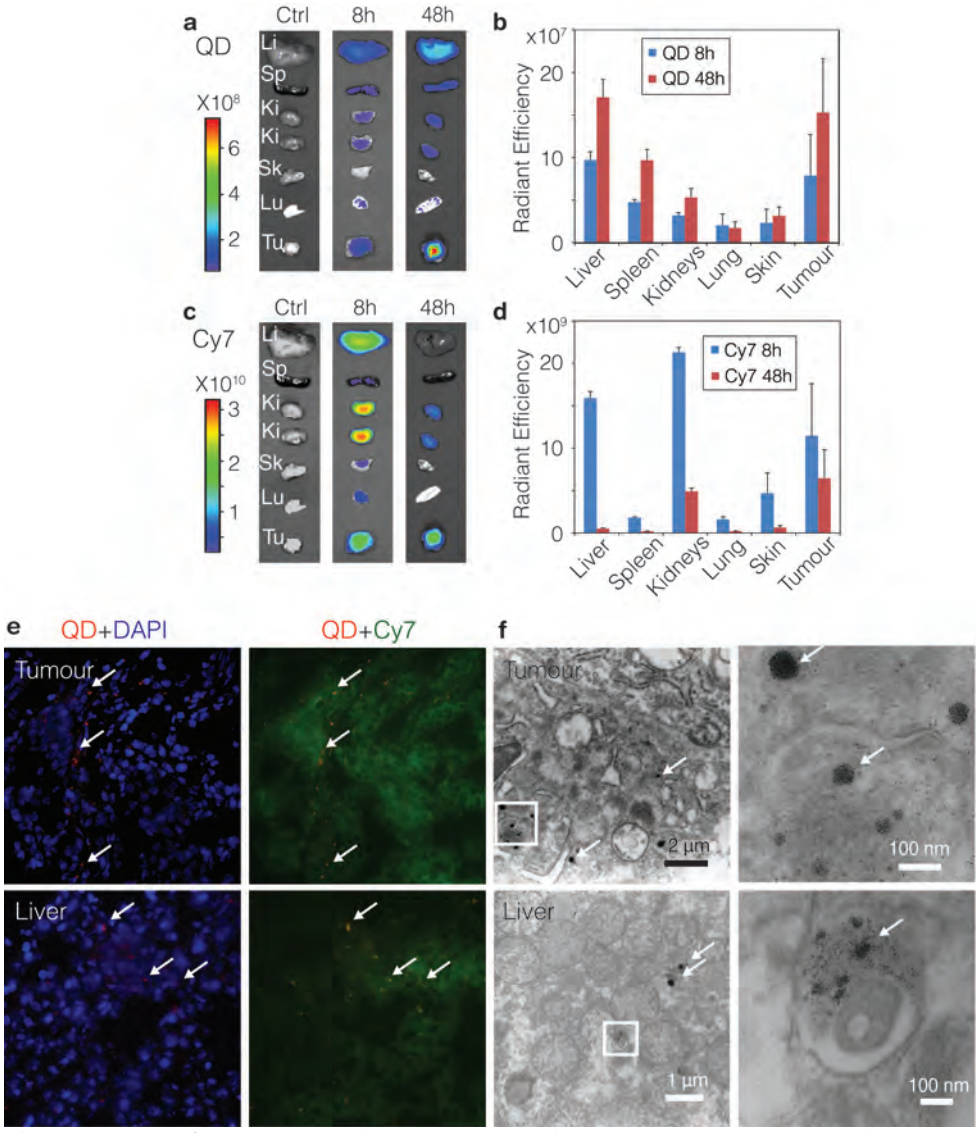

Figure 7.4. *Ex vivo* organ NIR fluorescence imaging of tumour mouse after intravenous injection. Representative images and mean intensities from the organs are presented in **a** and **b** for the QD channel and in **c** and **d** for the Cy7 channel. Li, liver; Sp, spleen; Ki, kidney; Sk, skin; Lu, lung; Tu, tumour. **e**, Fluorescence microscopy images of frozen sections of tumour (upper row) and liver (lower row) tissue sections at 48 h post-injection. Signal from QD (λ_{Exc} = 620 ± 30 nm, λ_{Em}= 700 ± 35 nm) is red, DAPI for nucleus staining (λ_{Exc} = 350 ± 30 nm, λ_{Em}= 460 ± 22 nm) is blue and Cy7 (λ_{Exc} =710 ± 35 nm, λ_{Em}= 810 ± 40 nm) is green. Aggregates of QD cores are indicated by arrows. **f,** Stained transmission electron microscopy (TEM) images of tumour (upper row) and liver (lower row) tissues at 48 h after injection. Insets are magnified on the right. Aggregates of QD cores are indicated by arrows.

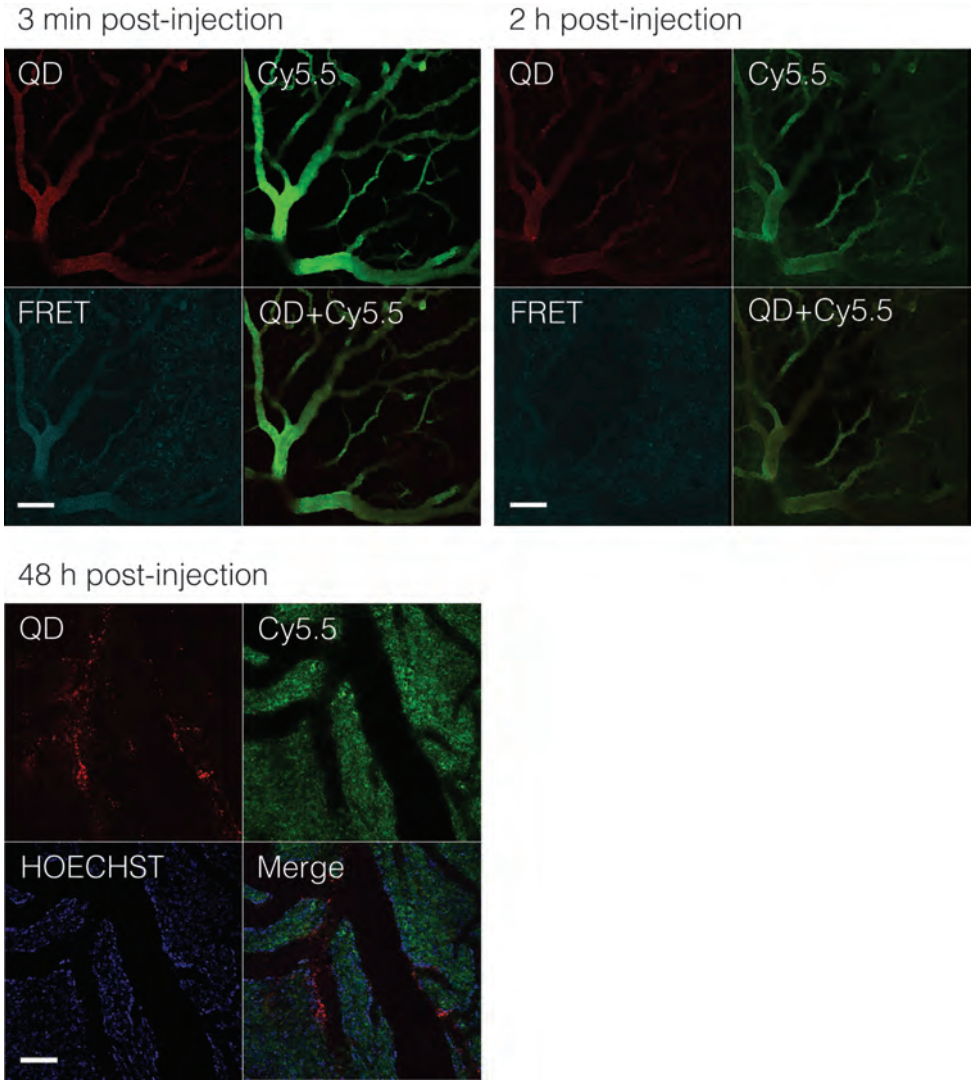

Figure 7.5. Intravital microscopy of tumours grown in a window chamber. Mice with tumour were injected with 130 pmol/g QD610-Cy5.5-PEG and continuously observed for 2 h, and discretely observed until 48 h post administration. Representative fluorescence images at 30 min, 2 h and 48 h are shown. The scale bar represents 100 µm. Four optical channels were used: QD (λ_{Exc} = 488 nm, λ_{Em}= 612-655 nm) is shown in red, Cy5.5 (λ_{Exc} = 633 nm, λ_{Em}= 698-719 nm) is shown in green, FRET (λ_{Exc} = 488 nm, λ_{Em}= 698-719 nm) in cyan and HOECHST for nucleus staining (λ_{Exc} = 780 nm, λ_{Em}= 435-485 nm) in blue.

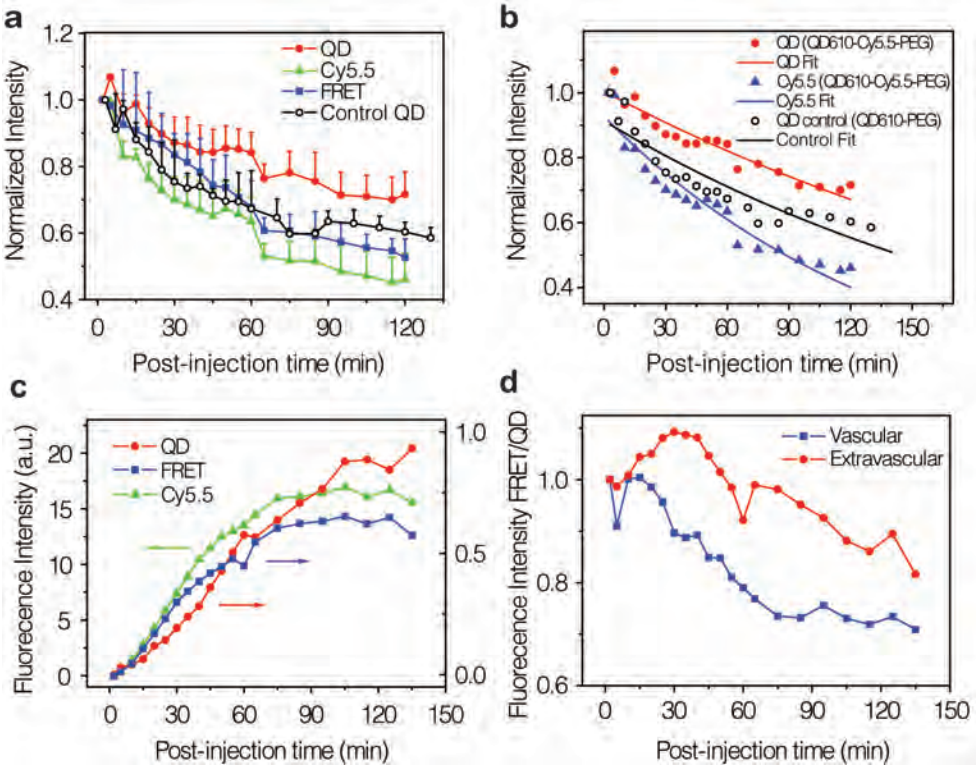

Figure 7.6. The normalized fluorescence intensities in three channels (QD in filled circles, Cy5.5 in filled triangles and FRET in filled square) are plotted against post-injection time for the vascular in **a** (circulation half-life fiting in b), and for extravascular space in **c**. QD610-PEG nanoparticles containing non Cy5.5-lipids were used as QD control (empty circles). **d,** The FRET/QD intensity ratios derived from the graphs in **a, c** represent the relative extent of FRET per QD and are plotted against time.

extravascular space. The lipid dissociation constant was derived from fitting the vascular FRET/QD ratio with a monoexponential decay function.[21] We found this constant to be 2.7×10^{-4} s^{-1} and the dissociation half-life to be around 42 min, indicating that the majority of the Cy5.5-lipids were dissociated from the QD after the first 2 hours. At 48 h a distinct dissociation of QD cores and Cy5.5-lipids was observed in the tumour interstitium (Figure 7.5 and Appendix Figure 7.4).

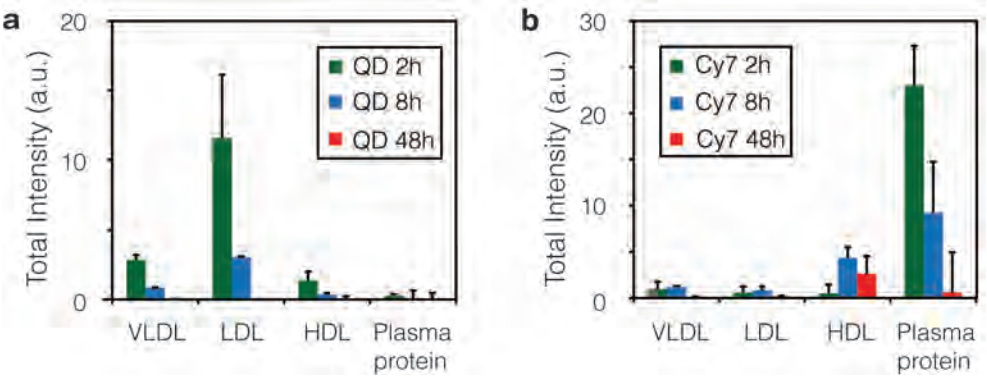

Figure 7.7. Plasma collected from mice at 2 h, 8 h and 48 h after injected with 100 pm/g QD-Cy5.5-PEG (n=3 animals for each time point) separated in different fractions using fast protein liquid chromatography (FPLC). The total fluorescent intensities from four different protein fractions: VLDL (25-90 nm), LDL (18-25 nm), HDL (5-15 nm) and small plasma proteins (< 5 nm) are summarized in **a**, for QD signal (λ_{Exc} = 430 ± 18 nm, λ_{Em}= 620 ± 10 nm), and in **b**, for Cy5.5 signal (λ_{Exc} = 640 ± 18 nm, λ_{Em}= 700 ± 10 nm).

The interaction between nanoparticles and serum proteins has recently been investigated by us and others.[10,11,17, 22] The afore-presented results indicated that the lipid-coated nanocrystals also vividly exchange coating lipids with blood proteins. Fast protein liquid chromatography (FPLC) [23] was employed to study different plasma fractions collected at 2, 8 and 48 h after intravenously administration of QD610-Cy5.5-PEG. At 2 h post-injection, the dominant QDs and Cy5.5-lipid intensities were found in different fractions (Figure 7.7a,b), indicating that the nanoparticle remained in blood had already dissociated with their lipid coating through lipid exchange while in circulation, which consists with the dissociation rate determined above. Although at early time points the majority of Cy5.5-lipids were found associated with small plasma proteins (<5 nm), at 48 h the main Cy5.5 intensity was observed in the HDL fraction (5-10 nm). This observation was in agreement with the clearance data for the Cy7/Cy5.5-labeled lipids where Cy5.5-lipids associated with small plasma proteins could be cleared renally, while labelled lipids that were associated with HDL could be retained as a result of the renal clearance threshold of around 5.5 nm.[24, 25] The latter caused Cy5.5-lipids to be mainly present in the HDL fractions at later time points.

To better understand lymphatic drainage dynamics of the nanoparticles in the sentinel lymph node (SLN) we isolated this process by injecting QD710-Cy7-PEG in the periphery of solid tumours in nude mice.[15,16] A representative NIR fluorescence image of this process is presented in Figure 7.8a. We observed the nanoparticles drained from the tumour and migrated to the inguinal lymph nodes (as SLN) within minutes. ROI analyses on the SLN revealed different dynamics for QDs and Cy7-lipids (Figure 7.8b). *Ex vivo* fluorescence imaging of SLN and organs was performed at 5 h and 45 h post administration to mimic a situation where nanoparticles are first allowed to accumulate in the tumour for 3 h after intravenous administration. Here, we also observed a difference in biodistribution between QDs and Cy7-lipids. The QDs were mostly retained in SLN and their intensity increased from 5 h to 45 h, due to dissociation of Cy7-lipids (Figure 7.8 c, d). Conversely, the intensity of the Cy7-lipid in SLN decreased over time, and its presence in the liver and kidneys was observed (Figure 7.8 e, f), implying trafficking of this component to these organs and subsequent renal clearance (Figure 7.1). FM (Figure 7.8g) and TEM images (Figure 7.8h) of excised SLN revealed the QD to be aggregated inside phagocytes and not to be co-localized with the Cy7-lipids.

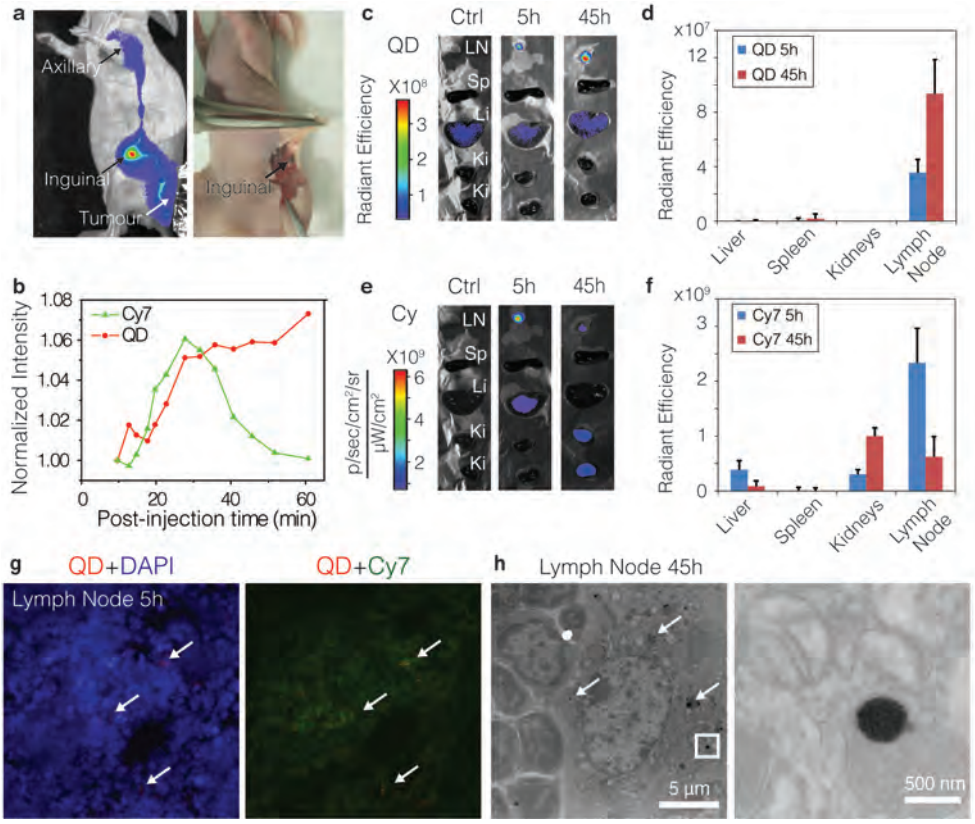

Figure 7.8. Peri-tumoural administration of lipid-coated nanocrystals. a, NIR fluorescence image (left, laid over brightfield image) show (presented in Cy7 channel) that the QD710-Cy7-PEG migrated through lymphatic draining from the periphery of the tumour to the inguinal node (as sentinel lymph node (SLN)) and further to the axillary node. After re-injection with 1% Evans blue and exposure the , QD710-Cy7-PEG and Evans blue were found co-localized in the same lymph node, as indicated by the arrows (**a,** right, color image). **b**, Normalized total fluorescent intensities of QD710 (squares) and Cy7 (triangles) from the SLN are plotted against post-injection time, showing their different dynamic behaviours. Mice were sacrificed at 5 h and 45 h post-injection time (n=3 for each time point). Subsequently, the inguinal node and major organs were subject to *ex vivo* fluorescence imaging. Representative images and mean intensities are depicted in **c** and **d** for the QD channel and in **e** and **f** for the Cy7 channel. LN, lymph node. **g**, Fluorescence microscopy images of SLN tissue at 5 h post-injection. Merged images are shown with signal from QD (red), Cy7 (green) and DAPI (blue). Spots of QD accumulates are indicated with arrows. **h**, TEM images of SLN tissues at 45h after injection. Aggregates of QD cores inside the lymphocytes are indicated by arrows. Insets are enhanced on the right.

7.3 Conclusion

In summary, SALNPs are dynamic structures that progressively disintegrate due to a lipid exchange process after intravenous administration (Figure 7.1, I). Upon vascular extravasation and accumulation in the tumour interstitium this process continues (Figure 7.1, IV). In case of the QD core SALNPs used in the current study, cellular internalization causes the QD cores to sequester in the tumour, lymph nodes and MPS organs (Figure 7.1 III, V), while their coating lipids partially follow different clearance kinetics in the circulatory system and can also be cleared renally.

Although the *in vivo* dissociation behaviour and the nanoparticle stability found in the current study is valid only for the particular type of SALNPs studied, [1, 6] the multi-faceted strategy we developed to assess the *in vivo* stability by FRET is flexible and applicable to a wide variety of SALNPs, including lipid-polymer hybrid nanoparticles[26] and lipoprotein-derived nanoparticles,[27] Moreover, it can be used to evaluate differently formulated SALNPs and screen for compositions with improved stability.[17]

The in vivo dissociation behaviour of SALNPs may influence their drug delivery efficiency, and may also have implications for other types of self-assembled nanoparticles, such as nanoparticles comprised of block copolymers.[28, 29] Our study also provides a framework to improve the specificity of self-assembled diagnostic nanoparticles since the in vivo integrity of such systems can now be carefully monitored. At the same time the exchange phenomenon may be exploited to transfer amphiphilic agents, such as cholesterol derivitized siRNAs[30] or diagnostically active amphiphiles,[1] from SALNPs to lipoproteins in the body.

To conclude, our approach represents a modular *in vivo* optical imaging tool to visualize the behaviour of self-assembled nanoparticles in real time and may contribute to enhancing the therapeutic outcome or improving the molecular imaging signature of this widely used class of nanoparticles.

7.4 Experimental

Synthesis of near-infrared (NIR) emitting CdTe/CdSe/CdS/ZnS core-shell-shell (CSS)QDs. CdTe/CdSe/CdS/ZnS core-shell-shell QDs were synthesized through a modified SILAR method.[31] Briefly, CdTe seed particles emitting at 576 nm were synthesized according to Wuister *et al*.[32] For multi-shell growth, washed CdTe cores were dispersed in 4 ml octadecene and 1.5 ml oleylamine. 20 mg tetradecylphosphonic acid was added as a stronger bonding ligand to maintain the spherical shape of the nanocrystal and to prevent Ostwald ripening. CdSe shell was grown by alternately adding 0.1 M cadmium oleate (made by dissolving CdO in oleic acid), and 0.1M Se in trioctylphosphine (TOP) as precursor solutions, and 0.1M S in TOP was used instead for subsquent CdS shell growth. The first layer of CdSe shell was grown at 200 °C, and temperature was then increased to 230 °C for later shell growth. The final ZnS shell was grown through adding 0.1M zinc diethyldithiocarbamate in TOP as single source precursor at 120 °C and by subsequently heating to 220 °C for shell growth. The emission wavelength was monitored through taking aliquots and measuring the sample emission spectra immediately after dispersion in toluene. The final emission wavelength was adjusted by stopping the precursor addition when desired wavelength was reached. The final product was washed in chloroform and acetone, and redispersed in chloroform.

Synthesis of Cy7-DMPE-labeled PEG-DSPE-coated NIR quantum dot micelles (QD710-Cy7-PEG). For synthesis of QD710-Cy7-PEG, a typical process is described below. 20 µmol of DSPE-PEG2000, and 1 nmol NIR-QDs were dispersed in 0.5 ml chloroform. Cy7 labeled lipid was added to this mixture at various mass percentages of 0%, 0.1%, 0.2 %, 0.5 % and 1 %. The dispersion was dripped into 2 ml heated (over 80°C) deionized water under vigorous stirring. After all the organic solvent was evaporated, this water dispersion was centrifuged at 2000 rpm for 10 min to remove uncoated QDs and large aggregates. The QD micelle dispersion was then purified by centrifuging 200 µL on top of 1 ml of 30% w/w KBr solution at 14,500 rpm for 2 h using a microcentrifuge tube. Centrifugation transferred the QD micelles into the KBr layer, and the top 250 µL containing empty micelles and free lipids was taken off and discarded. The remaining solution was collected (precipitation on the bottom of tube was discarded), and washed/desalted three times with PBS using a Vivaspin 30,000 MWCO tube. The nanoparticle solution was finally enriched to desired concentration by Vivaspin centrifugation.

Synthesis of Cy5.5-DMPE-labeled PEG-DSPE-coated quantum dot micelles (QD610-Cy5.5-PEG). The 610 nm emitting CdSe/CdS/ZnS CSS quantum dots were synthesized according to literature.[33] The emission wavelength was 610 nm and the size was around 7.5 nm determined by TEM. The QD610-Cy5.5-PEG micelles were synthesized using the same method as described above.

Optical characterization of nanoparticles. The emission spectra were recorded using a 450W Xe lamp as excitation source and a double grating 0.22 m SPEX monochromator of a SPEX Fluorolog to select the excitation wavelength of 500 nm. Emission was collected through an optical fiber leading to a 0.3 m monochromator (150 lines/mm, blazed at 550 nm) and detected by a liquid nitrogen cooled Princeton Instruments CCD camera (1024 × 256 pixels). Photoluminescence lifetime measurements were obtained by time-correlated single-photon counting. The setup consisted of a pulsed PicoQuant laser (2.5MHz, wavelength 406 nm), in combination with a monochromator (1350 lines/mm blazed at 630nm), a Hamamatsu photomultiplier tube (H5738P-01), and a Time Harp 200 computer card.

Negative stain transmission electron microscopy (TEM). The buffer of QD-Cy7-PEG solution was replaced by TEM buffer (0.125 M $CH_3CO_2NH_4$, 2.6 mM $(NH_4)_2CO_3$ 0.26 mM tetrasodium EDTA at pH 7.4) through washing twice in Vivaspin MWCO 30,000 centrifugation tubes. Samples were diluted to appropriate concentrations with TEM buffer and mixed with equal volumes of 2 % phosphotungstic acid (2PTA). The mixed solution was dropped and left to dry on a 100 mesh Formvar-coated nickel grid (Electron Microscopy Sciences). Sample grids were examined using a Hitachi 7650 TEM coupled to a Scientific Instruments and Applications (SIA) digital camera controlled by Maxim CCD software at 80 kV.

Cell culture and tumour model. HCT-116 cells were obtained from the Tumour Cell Biorepository of the Department of Oncological Sciences at the Icahn School of Medicine at Mount Sinai, and were cultured at 37°C under 5% CO_2 in DMEM culture medium, supplemented with 10% FBS. Six week old female Swiss nude mice were obtained from Taconic (Albany, NY) and were supplied with water and a standard rodent chow ad libitum. Five days before NIR fluorescent imaging, diet was changed to AIN-93M maintenance purified diet (TestDiet, Richmond, IN) in order to reduce the autofluorescent background. All animal handling was approved

by the Icahn School of Medicine at Mount Sinai Institutional Animal Care and Use Committee. The tumour model was established by inoculation of 2.5 million HCT-116 cells, suspended in 50 µl serum-free DMEM, on the right side flank of the mice. Tumours were grown for 2 weeks to an average volume of 400 mm^3, as measured with a digital caliper and by applying the formula $V = 0.52 \times a^2 \times b$, where *a* is the smallest measured diameter and *b* is the largest measured diameter.

In vivo fluorescence imaging. Tumour-bearing mice were injected intravenously by tail vein injection with QD710-Cy7-PEG or QD710-PEG at a dose of 100 pmol/g (n=5). For each experimental group, NIR fluorescence images of the mice were recorded at various time points after injection (t=0.25, 0.5, 0.66, 1.3, 1.9, 2.5, 3.2, 4, 5, 22, 27, 45h) using a Xenogen IVIS Spectrum imaging system (Alemeda, CA). Mice were anesthetized using vaporized isoflurane, with a 4% induction dose, and 5 mice at a time were positioned in the IVIS with isoflurane administered at 1.5% via a nose cone. Three optical channels were recorded with selected excitation and emission band pass filters: QD (λ_{Exc} = 605 ± 18 nm, λ_{Em} = 720 ± 10 nm), Cy7 (λ_{Exc} =745± 18 nm, λ_{Em} = 800 ± 10 nm) and FRET (λ_{Exc}= 605 ± 18 nm, λ_{Em}= 800 ± 10 nm). Overall acquisition time was 20s and all settings were kept the same for each time point, enabling comparison of intensity values. Results were processed and analyzed using Living Image software by drawing a region of interest (ROI) in the tumour area.

Ex vivo organ fluorescent imaging.The mice that were administered QD710-Cy7-PEG nanoparticles intravenously were sacrificed after 8h (n = 3) or 48h (n = 5) post-injection, and were perfused through the heart with 40ml PBS. Tumours and major organs were harvested and subject to fluorescent imaging immediately in the three optical channels described above. Organs from uninjected mice were used as blank control.

Peri-tumour injection of nanoparticles and lymph node imaging. Two groups of tumour mice (n = 3 animals for each group) were injected with two different nanoparticle solutions: (1) 10 µL of 20 nmol/ml QD710-Cy7-PEG; (2) 10 µL of 20 nmol/ml QD710 –PEG as the QD control. The solutions were injected intradermally in the peri-tumour region while the mice were under anesthesia. Immediately after injection, migration of the nanoparticles and dynamics of the lymphatic drainage

were followed by fluorescence imaging in the three channels at 5 minute intervals for 1h. The injection spot was masked while imaging to prevent saturation of the signal due to the much greater brightness of the injection site compared to the lymphatic vessels and lymph nodes. In all cases, the nanoparticles drained to the left inguinal lymph node within minutes, and in some cases continued to migrate to the left axillary node. To confirm the nanoparticles' drainage to the sentinel lymph nodes, 1% Evans blue was also injected in the peri-tumour region. Mice were sacrificed at 5 h (n=3) or 45 h (n=3) after injection. The left side inguinal nodes and other major organs were harvested and subjected to fluorescence imaging immediately in the three optical channels.

TEM of tumour, lymph node and other tissues. The tumour, lymph node, liver, spleen, and kidney from the above mentioned sacrificed mice were cut into small pieces and fixed in 2.5% glutaraldehyde. The tissue samples were processed by a standard procedure with osmium tetraoxide, and embedded in epoxy resin blocks. The resin blocks were cut into 60 nm sections with a microtome and placed on TEM grids. The sample grids were post stained with 4 % uranyl acetate and lead citrate before imaging. The TEM imaging used the same electron microscopy and conditions as previously described for nanoparticles characterization.

Fluorescence microscopy. Tissue samples of tumour, lymph node, liver, spleen, and kidney from the above mentioned sacrificed mice were embedded in OCT embedding matrix and frozen at -20°C. Five µm sections were cut on a cryostat and transferred to glass microscope slides. Upon use, sections were thawed for 20 minutes and mounted in Vectashield mounting medium with DAPI (Vector Laboratories, Burlingame, CA). Sections were imaged using a Zeiss Axioplan 2 Widefield Microscope (Zeiss, Jena, Germany) equipped with Cy5 and Cy7 filters (Chroma 49000 series, Chroma Technology Corp, Bellows Falls, VT) for imaging of QD710 and Cy7 dye, respectively. Cy5 exposure times were 100, 500, and 1500 milliseconds for liver, lymph node and tumour, respectively. Cy7 exposure times were 2000 milliseconds for liver, and 4000 milliseconds for lymph node and tumour tissues. Cy5 and Cy7 exposure times were kept constant per tissue for QD710-Cy7 and QD710 samples,.Magnification was 40 times in all fluorescence microscopy images.

Intravital microscopy. For intravital confocal laser scanning microscopy (CLSM, Zeiss LSM 510 META), tumours grown in dorsal window chambers in mice were used. The mice were anesthetized with a subcutaneous injection of 12 mg/kg midazolam/fentanyl/ haloperidol/water (3/3/2/4) and the window chambers (made of polyoxymethylene, build in house) were implanted as previously described in male athymic Balb/c Nu/nu mice of 22 to 24 gram.[34] 24 h after implanting the chambers, 2-3x10^6 HCT-116 cells were injected in the center of each chamber. The surgical procedures were performed under sterile conditions. The animals were kept under pathogen-free conditions at a temperature of 19 to 22 °C, 50 to 60% humidity, and 65 air changes per hour, and animals were allowed food and water (which contained 2% sucrose and 67.5 mg/L Baytril (enrofloxacin)) *ad libitum*. 16-18 days after implantation when the tumours were 0.2 to 0.3 cm thick and filled 30-60% of the window area, the mice were used for experiments. The mice were anesthetized by subcutaneous injections of 12 mg/kg midazolam/fentanyl/ Haldol/water (3/3/2/4), got a catheter (BD Venflon) placed in the tail veins and were placed on a custom build temperature controlled CLSM imaging stage.

The tumours were imaged using a long working distance Plan-Neofluor 20x/0.5 objective. DIC contrast was used to focus on tumour vasculature before injection and subsequently either QD610-PEG (n=2) (but only 1 intravascular curve from only one mouse) or QD610-Cy5.5-PEG (n=2) (But extravascular curve from only one) was injected at a dose of 130 pmol/g. To study nanoparticle and lipid dissociation dynamics, the same tumour region was imaged repeatedly at 3, 5, 10, 15, 20, 25, 30, 35, 40, 45, 50, 55, 60, 70, 80, 90, 100, 110, 120 min post injection. Subsequently, images were obtained throughout the tumour at several time points up to 48 hours post injection. HOECHST 33342 (Sigma) was injected 24 hours post injection of the nanoparticles to visualize cell nuclei facilitating the assessment of nanoparticle integrity and localization. QDs were excited at 488 nm and detected with the META system at 612-655 nm and Cy5.5 was excited at 633 nm and detected with the META system at 698-719 nm. FRET was detected using 488 nm excitation and recording with the META system at 698-719 nm. HOECHST 33342 was excited at 780 nm and detected with a bandpass filter at 435-485 nm.

Images were analyzed with ImageJ software. The images obtained in the first 2 hours post injection were aligned and combined into one dynamic series. ROIs were drawn manually in the vasculature and extravascular space from which the fluorescence intensity vs. time curves were obtained. Fluorescence intensities were normalized to the fluorescence intensity observed 3 minutes post injection. The FRET/QD ratio was obtained by dividing the normalized fluorescence intensities.

Fast protein liquid chromatography (FPLC). Tumour bearing nude mice (n=9) were anesthetized using isoflurane, and for each mice 100 pmol/g QD610-Cy5.5-PEG was administrated intravenously by tail vein injection. At 2h, 8h and 48h post-injection, 3 mice per time point were sacrificed and 500 µl of blood was drawn from the left ventricle of the heart. Serum was obtained through centrifugation at 10k rpm for 2x 10min. Two Superose-6 FPLC columns in series (Shimazu LC solution) were pre-equilibrated with degased filtrated buffer (0.15 M NaCl, 1 mM EDTA). Mouse serum samples were filtrated with a 0.22-micron pore size membrane, and 200µl for each sample were injected to the columns. Samples were then eluted with equilibration buffer while the absorbance of eluted solution was monitored at 280 nm. The eluent was collected and divided into four effective fractions according to predetermined retention time which corresponded to the size of proteins: VLDL (25-90 nm), LDL (18-25 nm), HDL (5-15 nm) and small plasma proteins (< 5 nm).[23] The fluorescence intensities of sample fractions were determined and analyzed by IVIS imaging system. The QD signal in the different fractions was measured with λ_{Exc} = 430 ± 18 nm, λ_{Em}= 620 ± 10 nm and the Cy5.5 signal was measured with λ_{Exc} = 640 ± 18 nm and λ_{Em}= 700 ± 10 nm.

Determination of circulation half-life of QD micelles in mice. A group of 3 mice were injected intravenously with 100 pmol/g QD610-PEG. Blood samples were taken at 5, 10, 20, 30min, 1, 2, 4, and 8h after injection, through puncturing the saphenous vein while mice were under anesthesia. At least 3 mg of blood was taken per sample and each sample was carefully weighed then diluted with 100 µL PBS. QD luminescence intensity was measured using IVIS imaging system.

References

1. Mulder, W. J. M.; Strijkers, G. J.; van Tilborg, G. A. F.; Cormode, D. P.; Fayad, Z. A.; Nicolay, K., Nanoparticulate Assemblies of Amphiphiles and Diagnostically Active Materials for Multimodality Imaging. *Acc. Chem. Res.* **2009**, 42, 904-914.
2. Shi, J.; Xiao, Z.; Kamaly, N.; Farokhzad, O. C., Self-assembled targeted nanoparticles: evolution of technologies and bench to bedside translation. *Acc. Chem. Res.* **2011**, 44, 1123-34.
3. Yoo, J. W.; Irvine, D. J.; Discher, D. E.; Mitragotri, S., Bio-inspired, bioengineered and biomimetic drug delivery carriers. *Nat. Rev. Drug Discov.* **2011**, 10, 521-35.
4. Whitehead, K. A.; Langer, R.; Anderson, D. G., Knocking down barriers: advances in siRNA delivery. *Nat. Rev. Drug Discov.* **2009**, 8, 129-38.
5. Peer, D.; Karp, J. M.; Hong, S.; Farokhzad, O. C.; Margalit, R.; Langer, R., Nanocarriers as an emerging platform for cancer therapy. *Nat. Nanotechnol.* **2007**, 2, 751-60.
6. Dubertret, B.; Skourides, P.; Norris, D. J.; Noireaux, V.; Brivanlou, A. H.; Libchaber, A., In Vivo Imaging of Quantum Dots Encapsulated in Phospholipid Micelles. *Science* **2002**, 298, 1759-1762.
7. Cormode, D. P.; Sanchez-Gaytan, B. L.; Mieszawska, A. J.; Fayad, Z. A.; Mulder, W. J. M., Inorganic nanocrystals as contrast agents in MRI: synthesis, coating and introduction of multifunctionality. *NMR Biomed.* **2013**, n/a-n/a.
8. Lobatto, M. E.; Fuster, V.; Fayad, Z. A.; Mulder, W. J., Perspectives and opportunities for nanomedicine in the management of atherosclerosis. *Nat. Rev. Drug Discov.* **2011**, 10, 835-52.
9. Jain, R. K.; Stylianopoulos, T., Delivering nanomedicine to solid tumors. *Nat. Rev. Clin. Oncol.* **2010**, 7, 653-64.
10. Li, Y.; Budamagunta, M. S.; Luo, J.; Xiao, W.; Voss, J. C.; Lam, K. S., Probing of the assembly structure and dynamics within nanoparticles during interaction with blood proteins. *ACS Nano* **2012**, 6, 9485-95.
11. Nel, A. E.*, et al.*, Understanding biophysicochemical interactions at the nano-bio interface. *Nat. Mater.* **2009**, 8, 543-57.
12. Owens, D. E., 3rd; Peppas, N. A., Opsonization, biodistribution, and pharmacokinetics of polymeric nanoparticles. *Int. J. Pharm.* **2006**, 307, 93-102.
13. Cormode, D. P.*, et al.*, A Versatile and Tunable Coating Strategy Allows Control of Nanocrystal Delivery to Cell Types in the Liver. *Bioconjugate Chem.* **2011**, 22, 353-361.
14. Hak, S.*, et al.*, The Effect of Nanoparticle Polyethylene Glycol Surface Density on Ligand-Directed Tumor Targeting Studied in Vivo by Dual Modality Imaging. *ACS Nano* **2012**, 6, 5648-5658.
15. Ballou, B.; Ernst, L. A.; Andreko, S.; Harper, T.; Fitzpatrick, J. A.; Waggoner, A. S.; Bruchez, M. P., Sentinel lymph node imaging using quantum dots in mouse tumor models. *Bioconjug. Chem.* **2007**, 18, 389-96.
16. Kim, S.*, et al.*, Near-infrared fluorescent type II quantum dots for sentinel lymph node mapping. *Nat. Biotechnol.* **2004**, 22, 93-7.
17. Skajaa, T.*, et al.*, Quantum Dot and Cy5.5 Labeled Nanoparticles to Investigate Lipoprotein Biointeractions via Forster Resonance Energy Transfer. *Nano Lett.* **2010**, 10, 5131–5138.
18. Medintz, I. L.; Clapp, A. R.; Mattoussi, H.; Goldman, E. R.; Fisher, B.; Mauro, J. M., Self-assembled nanoscale biosensors based on quantum dot FRET donors. *Nat. Mater.* **2003**, 2, 630-638.

19. Medintz, I. L.; Mattoussi, H., Quantum dot-based resonance energy transfer and its growing application in biology. *Phys. Chem. Chem. Phys.* **2009**, 11, 17-45.
20. Hak, S.; Reitan, N. K.; Haraldseth, O.; de Lange Davies, C., Intravital microscopy in window chambers: a unique tool to study tumor angiogenesis and delivery of nanoparticles. *Angiogenesis* **2010**, 13, 113-30.
21. Reulen, S. W.; Merkx, M., Exchange kinetics of protein-functionalized micelles and liposomes studied by Forster resonance energy transfer. *Bioconjug. Chem.* **2010**, 21, 860-6.
22. Salvati, A.*, et al.*, Transferrin-functionalized nanoparticles lose their targeting capabilities when a biomolecule corona adsorbs on the surface. *Nat. Nanotechnol.* **2013**.
23. Frias, J. C.; Ma, Y.; Williams, K. J.; Fayad, Z. A.; Fisher, E. A., Properties of a Versatile Nanoparticle Platform Contrast Agent To Image and Characterize Atherosclerotic Plaques by Magnetic Resonance Imaging. *Nano Lett.* **2006**, 6, 2220-2224.
24. Choi, H. S.*, et al.*, Renal clearance of quantum dots. *Nat. Biotechnol.* **2007**, 25, 1165-70.
25. Choi, H. S.; Liu, W.; Liu, F.; Nasr, K.; Misra, P.; Bawendi, M. G.; Frangioni, J. V., Design considerations for tumour-targeted nanoparticles. *Nat. Nanotechnol.* **2010**, 5, 42-7.
26. Valencia, P. M.; Basto, P. A.; Zhang, L.; Rhee, M.; Langer, R.; Farokhzad, O. C.; Karnik, R., Single-Step Assembly of Homogenous Lipid−Polymeric and Lipid−Quantum Dot Nanoparticles Enabled by Microfluidic Rapid Mixing. *ACS Nano* **2010**, 4, 1671-1679.
27. Bruns, O. T.*, et al.*, Real-time magnetic resonance imaging and quantification of lipoprotein metabolism in vivo using nanocrystals. *Nat. Nanotechnol.* **2009**, 4, 193-201.
28. Euliss, L. E.; Grancharov, S. G.; O'Brien, S.; Deming, T. J.; Stucky, G. D.; Murray, C. B.; Held, G. A., Cooperative Assembly of Magnetic Nanoparticles and Block Copolypeptides in Aqueous Media. *Nano Lett.* **2003**, 3, 1489-1493.
29. Berret, J.-F.; Schonbeck, N.; Gazeau, F.; El Kharrat, D.; Sandre, O.; Vacher, A.; Airiau, M., Controlled Clustering of Superparamagnetic Nanoparticles Using Block Copolymers: Design of New Contrast Agents for Magnetic Resonance Imaging. *J. Am. Chem. Soc.* **2006**, 128, 1755-1761.
30. Schroeder, A.; Levins, C. G.; Cortez, C.; Langer, R.; Anderson, D. G., Lipid-based nanotherapeutics for siRNA delivery. *J. Intern. Med.* **2010**, 267, 9-21.
31. Zhang, W.; Chen, G.; Wang, J.; Ye, B. C.; Zhong, X., Design and synthesis of highly luminescent near-infrared-emitting water-soluble CdTe/CdSe/ZnS core/shell/shell quantum dots. *Inorg. Chem.* **2009**, 48, 9723-31.
32. Wuister, S. F.; de Mello Donega, C.; Meijerink, A., Luminescence temperature antiquenching of water-soluble CdTe quantum dots: role of the solvent. *J. Am. Chem. Soc.* **2004**, 126, 10397-402.
33. Lim, J.; Jun, S.; Jang, E.; Baik, H.; Kim, H.; Cho, J., Preparation of highly luminescent nanocrystals and their application to light-emitting diodes. *Adv. Mater.* **2007**, 19, 1927-+.
34. Erikson, A.; Tufto, I.; Bjonnum, A. B.; Bruland, O. S.; Davies Cde, L., The impact of enzymatic degradation on the uptake of differently sized therapeutic molecules. *Anticancer Res.* **2008**, 28, 3557-66.

Appendix 7.1: Supporting Figures

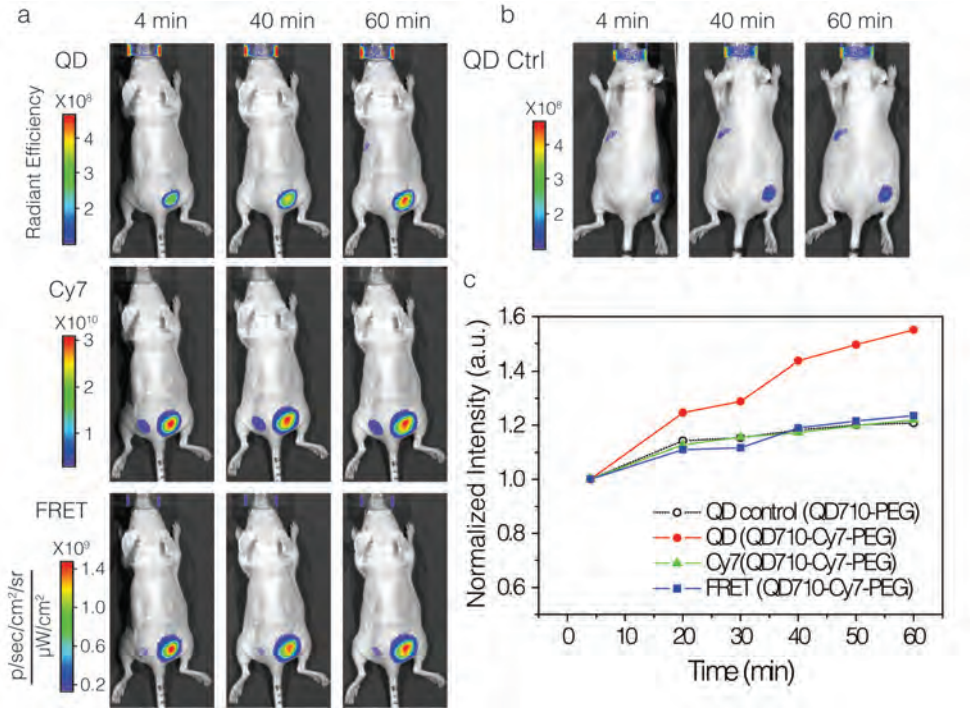

Figure A7.1. Test of FRET principle *in vivo*. a, NIR florescence image of nude mice at 4, 40, and 60min post-injection. The right side flank of the mice was subcutaneously injected with 5 pmol/g QD710-Cy7-PEG. Fluorescent signal was collected through three optical channels: QD (λ_{Exc} = 605 ± 18 nm, λ_{Em} = 720 ± 10 nm), Cy7 (λ_{Exc} =745± 18 nm, λ_{Em} = 800 ± 10 nm) and FRET (λ_{Exc}= 605± 18 nm, λ_{Em}= 800 ± 10 nm). b, Control mice subcutaneously injected with 2 pmol/g QD710-PEG in the right side flank c. The integrated luminescent intensities from the injected areas plotted against post-injection time. There is a gradual increase of intensity of about 20% within 1 h in all channels, due to diffusion of the nanoparticles from the injection site. However, the QD intensity from the FRET dots increased over 50% after 1 h. This enhancement of QD intensity is due to dissociation of Cy7-lipids which dequenches the QD emission.

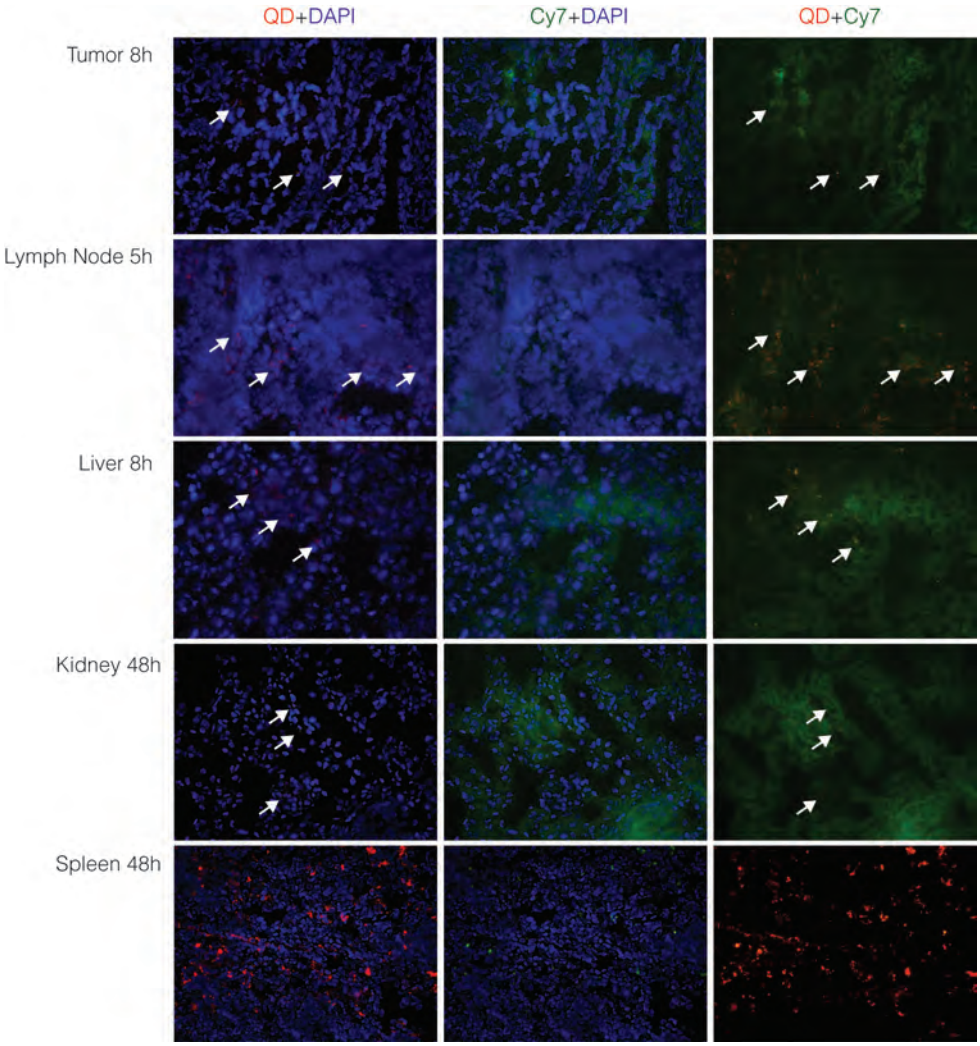

Figure A7.2. Fluorescence microscopy images of frozen sections of tumour, lymph node, liver, kidney and spleen tissues after intravenous injection. Signal from QD (λ_{Exc} = 620 ± 30 nm, λ_{Em}= 700 ± 35 nm) is presented in red, DAPI (λ_{Exc} = 350 ± 30 nm, λ_{Em}= 460 ± 22 nm) in blue and Cy7 (λ_{Exc} =710 ± 35 nm, λ_{Em}= 810 ± 40 nm) in green. Accumulated QDs are indicated by arrows.

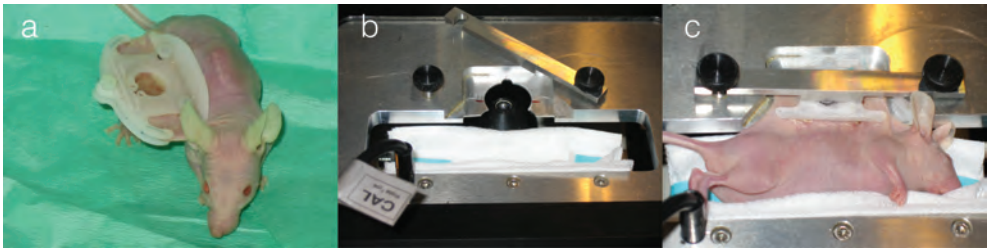

Figure A7.3. a, Tumour grown in dorsal window chambers in a nude mouse for intravital confocal laser scanning microscopy (CLSM). b, A custom build temperature-controlled CLSM imaging stage. c, Mouse with window chamber is loaded on the CLSM imaging stage.

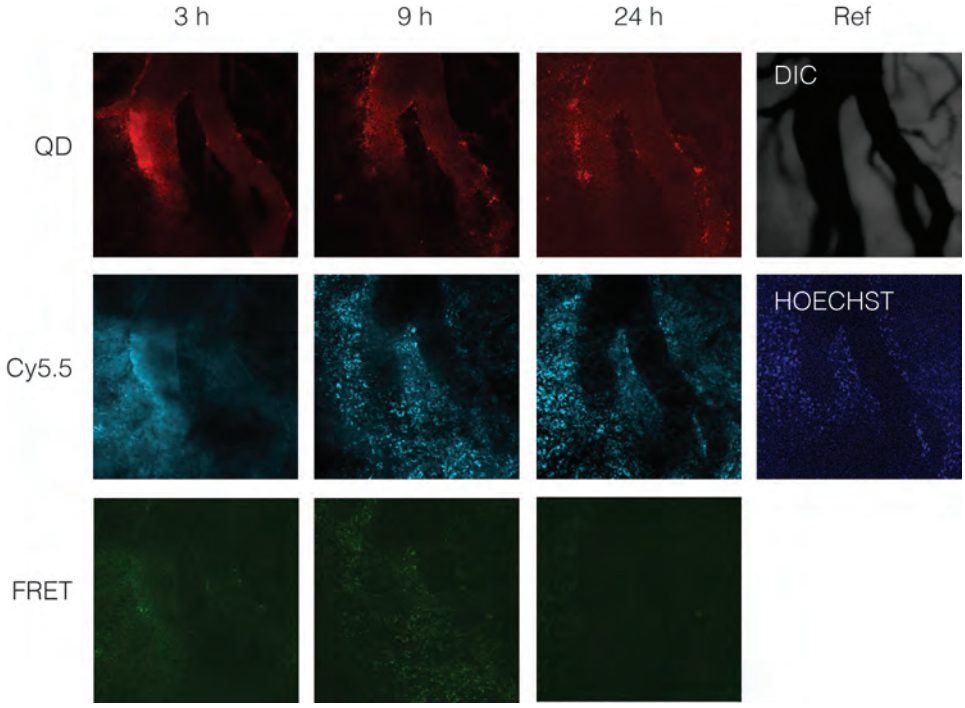

Figure A7.4. CLSM images of tumours grown in a window chamber model, after intravenous injection of 130 pmol/g QD610-Cy5.5-PEG. Images were recorded at 3, 9, 24 h post-injectionin three optical channels: QD (λ_{Exc} = 488 nm, λ_{Em}= 612-655 nm) are shown in red, Cy5.5 (λ_{Exc} = 633 nm, λ_{Em} = 698-719 nm) are shown in green, and FRET (λ_{Exc} = 488 nm, λ_{Em} = 698-719 nm) in cyan. HOECHST 33342 was injected 24 hours post injection of the nanoparticles to visualize cell nuclei facilitating the assessment of nanoparticle integrity and localization. HOECHST channel was excited at 780 nm and detected with a bandpass filter at 435-485 nm.

Summary

The aim of this thesis is to develop new luminescent nanoparticles, including quantum dots (QDs) and doped nanocrystals (NCs), for the application in biomedical research. Owing to their unique and incomparable optical properties, luminescent nanoparticles have been widely applied as fluorescent labels for both live cell imaging as well as in *in vivo* diagnostics. The studies in this thesis discuss both fundamentals and applications. As an introductory part, Chapter 1 gives a brief survey of the synthesis and optical properties of luminescent nanocrystals, and also concerns the surface modification and biocompatibility of functional nanocrystals. The individual studies constitute the later chapters and three parts are distinguished, involving the chemical synthesis, optical properties and bio-applications of nanocrystals, respectively.

The first part deals with lanthanide doped nanocrystals. Binary alkaline earth sulfides form an important class of host materials for a wide range of luminescent dopant ions. Especially, CaS:Ce^{3+}, Sm^{3+} and CaS:Eu^{2+}, Sm^{3+} are well-known afterglow materials, and if colloidally stable monodisperse nanoparticles of these sulfides can be made, they will be excellent candidates for non-toxic afterglow nanolabels for background-free biomedical imaging. To that end, in Chapter 2, small ~10 nm CaS and SrS colloidal NCs with a narrow size distribution were made through thermal decomposition of a metal-dithiocarbamate complex in oleylamine. In Chapter 3, this single source precursor method was further developed for the synthesis of Ce^{3+} and Eu^{2+} doped CaS and SrS NCs. The use of host and dopant precursors with similar decomposition temperatures is found to be one of the key factors to successful doping. Moreover, the application of two sophisticated doping strategies brought more efficient incorporation of dopant ions and flexibility on the doping methods. For the growth-doping strategy, an additional shell of the host material is grown around a doped nanocrystal, which internalizes the surface adsorbed Ce^{3+} or Eu^{2+} ions. For the nucleation-doping strategy, small nanocrystals of the dopant material are first synthesized and subsequently over-coated with a shell of the host material. The shell growth is accompanied by diffusion and intermixing of dopant ions into the shell, leading to successful doping. The single-source precursor approach proposed here has the potential to be widely applicable to the synthesis of other doped nanocrystals.

The second part of this thesis studies optical properties of QDs. In Chapter 4, the temperature dependent photoluminescence intensity and emission lifetime of

three representative highly efficient (60-70 % quantum yield) core-shell CdSe QDs systems are investigated at high temperatures (up to 200 °C), and they show different thermal quenching behaviors. Thermal cycling ('yoyo') experiments make it possible to differentiate between reversible and irreversible luminescence quenching processes. Irreversible quenching originates from thermally induced permanent structural changes, giving rise to trap states, and is present in CdSe/CdS/ZnS core-shell-shell QDs and CdSe/CdS dot core/rod shell nanorods, but interestingly not in CdTe/CdSe core/shell QDs. Reversible quenching contributes to luminescence quenching for QDs in all three core-shell systems in a similar temperature range (quenching between 100-180 °C). The possible mechanism for the reversible quenching is thermal induced temporary trap state formation or thermally activated escape of carriers to existing (surface) trap states. The results in this chapter have important implications for application of QDs in optical devices relying on QD luminescence at elevated temperatures.

The third part of this thesis contains a series of investigations applying QDs as nanoprobes to study the dissociation and lipid exchange dynamics of self-assembled lipidic nanoparticles (SALNPs), which is relevant to biomedical imaging applications. These nanoprobes contain a QD core and dye-labeled lipids in the self-assembled lipid corona. The efficiency of the Förster resonance energy transfer (FRET) from QD core to Cy5.5 is related to the number of dye-lipids attached to the QD core. Based on this FRET platform, by monitoring the time-dependent emission profile, the dynamics of the lipids can be followed.

In Chapter 5, a physical chemistry study is first carried out with this FRET platform, studying in situ the dynamics of lipid exchange and its dependence on concentration of free lipid molecules, temperature and solvent. A kinetic model is developed to describe the experimental data, allowing the rate constants and the activation energy for lipid exchange to be determined. The activation energy for lipid exchange on QD micelles is 155 kJ/mol in saline environment and 130 kJ/mol in pure water.

Next, in Chapter 6, this FRET principle is developed into a lipoprotein-based nanoparticle to study in vitro the lipoprotein-lipoprotein interactions, and the lipoprotein-cell interactions. Through comparing the rate of lipid exchange between high density lipoprotein (HDL) and other lipidic nanoparticles, the stabilizing features of the apoA-I on lipid self-assembled structures is confirmed. FRET fluorescence microscopy reveals the temporal fate of lipoproteins in association with the cell. When approaching the cell, the lipids from the HDL nanoparticle

exchange with the cell membrane and, once taken up by the cell, the lipids dissociate from the QD core.

Last, in Chapter 7, this nanocrystal based FRET technology is advanced by tuning its optical features to the near infrared (NIR), in order to monitor the dissociation and tumor accumulation of nanoparticles in real time by in vivo fluorescence imaging techniques. Self-assembled lipidic nanoparticles have been applied broadly as intravenously injectable agents for biomedical purposes. However, studies that address their dissociation kinetics are scarce. This chapter reveals that SALNPs are dynamic structures that progressively disintegrate due to a lipid exchange process after intravenous administration. Upon vascular extravasation and accumulation in the tumour interstitium this process continues. In case of the QD core SALNPs used in the current study, cellular internalization causes the QD cores to sequester in the tumour, lymph nodes and mononuclear phagocyte system (MPS) organs, while their coating lipids partially follow different clearance kinetics in the circulatory system and can also be cleared renally. The methods developed in this chapter can be used to evaluate differently formulated SALNPs and screen for compositions with improved stability, and may also contribute to enhancing the therapeutic outcome or improving the molecular imaging signature of this widely used class of nanoparticles.

Samenvatting in het Nederlands

Het doel van dit onderzoek is de ontwikkeling van nieuwe luminescerende nanodeeltjes, waaronder quantum dots (QDs) en gedoteerde nanokristallen, voor toepassing in biomedisch onderzoek. Nu al worden luminescerende nanodeeltjes gebruikt als fluorescerende labels voor medische beeldvorming, zowel in enkele levende cellen als *in vivo*. Het onderzoek in dit proefschrift omvat zowel de fundamentele aspecten van luminescerende nanodeeltjes als de biomedische toepassingen. Hoofdstuk 1 geeft een algemene introductie over de synthese en optische eigenschappen van luminescerende nanodeeltjes. Daarnaast beschrijft het hoe het oppervlak van nanodeeltjes kan worden gefunctionaliseerd om ze biocompatibel te maken. De daarop volgende hoofstukken bevatten het eigenlijke onderzoek. Dit bestaat uit drie delen, te weten de chemische synthese, de optische eigenschappen en de biomedische toepassingen van nanokristallen.

Het eerste deel beschrijft de synthese van lanthanide-gedoteerde nanokristallen. Sulfides van de aardalkali-metalen vormen een belangrijke klasse van gastroosters voor luminescerende lanthanide-ionen. Zo zijn CaS:Ce^{3+}, Sm^{3+} en CaS:Eu^{2+}, Sm^{3+} bekende nalichtende materialen. Monodisperse nanokristallen van deze materialen zouden zeer veelbelovend zijn als niet-giftige nalichtende-nanolabels voor achtergrondvrije biomedische beeldvorming. Met de ontwikkeling hiervan in gedachten, beschrijft Hoofdstuk 2 de synthese van colloïdale CaS en SrS nanokristallen. De thermische ontleding van metaal-dithiocarbamaat-complexen in oleylamine levert nanokristallen op met een gemiddelde diameter van ~10 nm en een nauwe grootteverdeling. Hoofdstuk 3 bouwt voort op deze methode, en beschrijft de dotering van CaS en SrS nanokristallen met Ce^{3+} en Eu^{2+}. Twee verschillende strategieën leiden tot succesvolle dotering. Bij beide is het cruciaal dat de uitgangsstoffen voor gastrooster en dotering vergelijkbare ontledingstemperaturen hebben. De groeidoteringsstrategie houdt de groei in van een schil van het gastrooster om een gedoteerd nanokristal, waarbij aan het oppervlak geadsorbeerde Ce^{3+}- of Eu^{2+}-ionen worden ingebouwd. Bij de nucleatie-doteringsstrategie wordt een klein nanokristal van doteringsmateriaal als kern gebruikt voor de groei van een schil van het gastrooster, waarbij diffusie leidt tot menging en inbouw. Deze twee methoden lijken algemeen toepasbaar te zijn voor de synthese van andere typen gedoteerde nanokristallen.

Het tweede deel van dit proefschrift behandelt de optische eigenschappen van QDs. Hoofdstuk 4 beschrijft de temperatuurafhankelijkheid tot 200°C van de inten-

siteit en levensduur van de luminescentie van QDs. Een vergelijking van drie typen kern/schil QDs met een hoge luminescentie efficiëntie (60-70% quantumopbrengst) toont verschillen in de temperatuurdoving. Jojo-experimenten van afwisselend opwarmen en afkoelen maken het onderscheid mogelijk tussen omkeerbare en onomkeerbare doving. Onomkeerbare doving vindt plaats in CdSe/CdS/ZnS kern/schil/schil QDs en in CdSe/CdS kern-in-staaf nanokristallen, maar opvallend genoeg niet in CdTe/CdSe kern/schil QDs. Alle drie de onderzochte systemen vertonen bovendien omkeerbare doving tussen 100°C en 180°C. Onomkeerbare doving kan worden toegeschreven aan permanente structurele veranderingen in de nanokristallen, terwijl omkeerbare doving een gevolg is van tijdelijke trap-toestanden of thermisch geactiveerde excitatie naar bestaande trap-toestanden.. De resultaten uit dit hoofdstuk hebben belangrijke implicaties voor het gebruik van de luminescentie van QDs in toepassingen waarbij de QDs een verhoogde temperatuur bereiken.

Het derde deel van dit proefschrift beschrijft een aantal studies waarin QDs worden gebruikt om lipide-uitwisseling van lipide-gebaseerde nanodeeltjes te bestuderen. Deze nanodeeltjes bestaan uit een centrale QD omgeven door een coating van lipiden waarvan een deel fluorescent gelabeld is. De efficiëntie van energieoverdracht (Förster resonance energy transfer; FRET) van de QD kern naar de fluorescerende labels is gerelateerd aan het aantal fluorescerende lipiden in de coating. Op deze manier geeft het tijdsverloop van de energieoverdracht direct informatie over de dynamica van de lipiden.

In Hoofdstuk 5 wordt dit FRET-systeem *in situ* gebruikt voor het volgen van de uitwisseling van lipiden, als functie van de concentratie van vrije lipiden, de temperatuur en het oplosmiddel. De experimentele data kunnen worden beschreven met een kinetisch model, waaruit de snelheidsconstanten en activeringsenergie voor de uitwisseling van vetten kunnen worden afgeleid. De activeringsenergie voor uitwisseling is 155 kJ/mol in buffer en 130 kJ/mol in zuiver water.

Vervolgens, in Hoofdstuk 6, wordt dit FRET-principe toegepast op een lipoproteïne-gebaseerd nanodeeltje. Hiermee wordt de interactie bestudeerd tussen lipoproteïnen onderling en tussen lipoproteïnen en cellen. Door de uitwisselingssnelheid te bestuderen tussen een lipoproteïne-nanodeeltje en andere lipide-nanodeeltjes kan de stabiliserende werking van de apolipoproteïne-component worden vastgesteld. Met FRET-fluorescentie microscopie wordt de complexe interactie van lipoproteïne-nanodeeltjes met cellen bestudeerd. Hieruit blijkt dat de coatingslipiden uitwisselen met het celmembraan, terwijl de centrale QD door de cel wordt opgenomen.

Hoofdstuk 7 beschrijft een onderzoek uitgevoerd met een verbeterde versie van het FRET-modelsysteem. De emissiegolflengte is verschoven naar het nabije-infrarood (NIR), zodat het uiteenvallen en de targeting van de nanodeeltjes *in vivo* en in real-time kunnen worden gevisualiseerd. Lipide-nanodeeltjes worden veelvuldig toegepast als intraveneus injecteerbare nanodeeltjes voor biomedische doeleinden. Studies die de dissociatiekinetiek *in vivo* bestuderen zijn echter nauwelijks voorhanden. In dit hoofdstuk wordt duidelijk dat de lipide-nanodeeltjes na toediening geleidelijk uiteenvallen via uitwisseling. Dit proces gaat door ook nadat de nanodeeltjes zich ophopen in de tumor. Voor de specifieke nanodeeltjes toegepast in deze studie hopen de QD-kernen zich op in de tumor, maar ook in de lymfeknopen, de lever en de milt, terwijl de lipiden een alternatieve afbraakroute volgen, onder andere via de nieren. De hier beschreven methoden kunnen ook worden toegepast op andere types van nanodeeltjes, om zo de samenstelling en stabiliteit van nanodeeltjes te verbeteren. Deze informatie kan uiteindelijk worden gebruikt om therapeutische of diagnostische eigenschappen van nanodeeltjes te verbeteren.

Acknowledgements

The four years of PhD is never a lonely and isolated journey. Without the support, patience and guidance of the following people, this work would not have been accomplished. It is to them that I owe my deepest gratitude. And every line I wrote here contains memories of the good times we spent together.

First and foremost, I would like to thank my three supervisors. **Andries**, thank you for offering me the PhD position on such an interesting topic. It is hard to forget the pleasure and frank conversation we had when we first met. I am so grateful to your scientific guidance, your kind support and considerable encouragement. Moreover, you do not only guide me in science and research, but also influence me by your wisdom, virtue and your attitude towards life. There is a Chinese proverb that fits here well: “For one day be my master and I respect you as my father for my lifetime.” I will be forever your student. Also, my sincere appreciation goes to my daily supervisor, **Celso**. It is your impressive lecture on quantum dots during the summer school that made me interested in them and decided to accomplish a PhD on it. You always patiently explain to me the principles of nanocrystal synthesis, and help me designing the route of experiments and give me valuable advises on my speeches. Whenever I encountered problems and difficulties in my experiments, your door was always open for me with suggestions and solutions. **Willem**, I am honored to be the first PhD you promoted in the Netherlands. Thanks for your professional, responsible and pleasant supervision. I really enjoy working with you, in the American pace, trying out inspiring and fancy ideas. I also learned from your working efficiently with a clear focus and solving problems practically.

I am greatly thankful to the reading committee of my thesis: **Cees Ronda, Daniël Vanmaekelbergh, Daniel Gamelin,** and **Hans Gerritsen**. Thank you for carefully reading my thesis and providing me with valuable scientific comments.

Also, special thanks go out to my dear collaborators. It is your expertise from different fields that made this thesis possible to become multidisciplinary. The first person I teamed up with is **Torjus,** a medical doctor. I still remember the exciting moment we shared when seeing the shining dots inside a cell. **Dave**, a microscopist and the ‘go-to-guy’. Thank you for the times we stayed in the darkroom where we were staring at those blinking dots, accompanied with your classic rock music. Many thanks go out to the theorist, **Philipp**. Your clear thought and solid logic both impressed and inspired me. **Kees**, thanks for your organic

chemistry input, which is an important step for the single-source precursor method we developed. **Sjoerd**, thanks for the cool work on intravital microscopy, and also for the helpful discussions on Skype. Thanks to **Rolf, Patrick, Thijs, Matti, Jan Andries** and all the others that have scientifically contributed to this thesis.

I am grateful to three Master students and two Bachelor students I had supervised. Their excellent works significantly contribute to this thesis. **Freddy**, I truly appreciate your scientific talent and enthusiasm, and also thank you a lot for the Dutch translation of the summary part. **Marie Anne**, I remember well the great time we spend on the “quantum dotjes”. **Tim**, thanks for your hard working and the pancake-skating trip we had together. **Charl** and **Ludo**, your contribution during your bachelor research are highly appreciated.

Moreover, I would like to express my deepest gratitude to all the colleagues of the CMI group. Thanks for creating the best working and relaxing atmosphere during the past years. My best officemate, **Dominika**, the first luckiest thing I have here is to have you sitting beside. My lovely Domino, with you, our office is the coziest and sweetest place. **Zachar**, it is absolute fun to fabricate a QD solar concentrator with you, and I truly enjoy our endless discussion on history, philosophy and religion. **Rosa**, I have learned a lot from you about lanthanides and up-conversion, as well as about Spanish food. **Francesca**, thank you for your shiny nanorods, You are also the manager of our leisure time. **Dariusz**, thanks for sharing your experience on QD synthesis and your knowledge on solar cells. **Marianna**, I am grateful for your suggestions about scientific career. **Wiel**, thank you for all the help in the Lab. **Zhixiang** and **Dechao**, it is amazing to have someone in the lab with who I can discuss science in Chinese. Special thanks to **Joren**, **Alek, Peter, Esther, Relinde, Ingmar, Wiebke, Mark, Bert, Joost**, **Ward** and all the **CMI members** whose name I haven’t mentioned yet. Last in this CMI list is the backbone of research in our lab. Many thanks to **Hans Ligthart**, thank you for your excellent technical support, and also for fixing up all the mess I have made. Your humor and optimism enlightened our daily life. **Stephan**, I really appreciate your programming and system skills. Whenever I faced an IT problem and knocked on your door, there would be a solution waiting. Also thanks **Hans Meeldijk**, for your teaching and helping me with TEM.

Last summer, I had a fantastic time in New York City as a visiting researcher. Without the help of friends at Sinai, I would never have such a great experience for both science and city life. First of all, I would like to say many thanks to **Inge**. Thank you for teaching me all the bio-skills. It is such a pleasure to work together with you. If it was not your expertise, patience, and carefulness, we could never

succeed in those high-risk experiments. **Jun**, thanks for taking care of me in New York. I feel like I have a big brother who can always give me suggestions on science and career. **François**, **Brenda,** thank you for all the help in the lab, and I really miss the great time we spent together. **Anita**, **Aneta**, **Mark**, **David**, I benefited a lot from our discussions, and thank you for your valuable suggestions. I would like to thank all the collaborators and supervisors at Sinai that helped me, specially **Can**, **Yu Zhou**, **Johnny**, **Juan**, **Jesus**, **Aurelian**, and **Zahi**.

In addition, I would like to thank **the people I met during conference or visit**. Thanks for the scientific discussion and your suggestions on my research and career.

Thanks to all my Chinese friends in the Netherlands, your company made me feel at home. Special thanks to **Bo Peng**, my best roommate and big brother. **Xin Jin**, thank you for your constructive suggestions and caring about me. **Xinhan Luo**, I enjoyed all the social activities we organized. **Na Yu**, **Yuxuan Fan**, **Lu Zhang, Hansin Chang (Taiwan), Hengyu Li**, **Yuan Gao**, **Yinhuan Kuang**, **Yanchao Liu**, **Xiangyu Rao**, **Ran Ni**, **Juan Yang**, **Qingyun Qian**, **Wenhao Luo**, **Ou Fu**, **Xinlin Zhang**, **Da Wang** (another fan of classical music), **Tian Song**, **Bing Liu** and **many others**, thank you all.

Finally, I would like to thank my family for their constant caring, support and love. 感谢无私奉献的爸爸妈妈，虽远隔重洋，却对我无时不刻的牵挂。你们永远是我心中最坚实和温暖的力量。感谢岳父岳母，你们的关心和理解使我们未来的路走的更加自信。感谢小姨和姨夫，我成长的每一步都离不开你们的引导和支持。感谢爷爷，家家，长辈们和兄弟姐妹们。感谢我的奶奶，您的在天之灵一直守护和保佑着我。
Thank my beloved wife, **Yaqin**. Most of time in the past few years, we were apart in distance, but never at heart. From China to Europe and to US, we have overcome much more difficulties than others, but yet we made it. You support me in daily life, guide me to be more mature, and strengthen me in my soul. You know how hard to describe my gratefulness to you…

List of Publications

This thesis is based on the following publications:

- Y. Zhao, F.T. Rabouw, C. de Mello Donegá, A. Meijerink, C. A. van Walree, Single-source precursor synthesis of colloidal CaS and SrS naocrystals, *Mat. Lett.* **2012** 80, 75-77. (Chapter 2)

- Y. Zhao, F.T. Rabouw, T. van Puffelen, C. van Walree, C. de Mello Donegá, and A. Meijerink, Lanthanide Doped CaS and SrS Luminescent Nanoparticles: A Single Source Precursor Approach for doping, to be submitted **2013**. (Chapter 3)

- Y. Zhao, C. Riemersma, F. Pietra, R. Koole, C. de Mello Donegá, A. Meijerink, High Temperature Luminescence Quenching of Colloidal Quantum Dots*, ACS Nano* **2012** 6 (10), pp 9058–9067 (Chapter 4)

- Y. Zhao, P. Schapotschnikow, T. Skajaa, T.J.H. Vlugt, W.J.M. Mulder, C. de Mello Donegá, and A. Meijerink, Investigation of lipid exchange dynamics of quantum dot core micelles via Förster resonance energy transfer, submitted **2013**. (Chapter 5)

- T. Skajaa,* Y. Zhao,* D. J. van den Heuvel, H. C. Gerritsen, D.P. Cormode, R. Koole, M.M. van Schooneveld, J.A. Post, E.A. Fisher, Z.A. Fayad, C. de Mello Donega, A. Meijerink, W.J.M. Mulder, Quantum Dot and Cy5. 5 Labeled Nanoparticles to Investigate Lipoprotein Biointeractions via Förster Resonance Energy Transfer. *Nano Lett.* **2010** 10 (12), 5131-5138 * contributed equally. (Chapter 6)

- Y. Zhao, I. van Rooy, S. Hak, F. Fay, J. Tang, C. de Lange Davies, M. Skobe, E.A. Fisher, A. Radu, Z.A. Fayad, C. de Mello Donegá, A. Meijerink and W.J.M Mulder, *In vivo Near-infrared FRET Imaging of Nanoparticle Accumulation and Dissociation Kinetics in Tumour-bearing Mice*, submitted **2013**. (Chapter 7)

Other publications:

- J. Shan, Y. Zhao, N. Granqvist, H. Tenhu, Thermoresponsive properties of N-isopropylacrylamide oligomer brushes grafted to gold nanoparticles: Effects of molar mass and gold core size, *Macromolecules* **2009** 42 (7), 2696-2701

- A.J. Mieszawska, A. Gianella, D.P. Cormode, Y. Zhao, A. Meijerink, R. Langer, O.C. Farokhzad, Z.A. Fayad, W.J.M. Mulder, Engineering of lipid-coated PLGA nanoparticles with a tunable payload of diagnostically active nanocrystals for medical imaging. *Chem. Commun.* 2012, **48**, 5835-5837

- Z. Krumer, S.J. Pera, R.J.A. van Dijk-Moes, Y. Zhao, A.F.P. de Brouwer, E. Groeneveld, W.G.J.H.M. van Sark, R.E.I. Schropp, C. de Mello Donegá, Tackling self-absorption in luminescent solar concentrators with type-II colloidal quantum dots, *Sol. Energ. Mat. Sol. Cells* **2013**, 111, 57-65.

- L.W.E. Starmans, M.B. Kok, H.M.H.F. Sanders, Y. Zhao, C. de Mello Donegá, A. Meijerink, W.J.M. Mulder, H. Grüll, G.J. Strijkers, K. Nicolay, Influence of cell-internalization on relaxometric, optical and compositional properties of targeted paramagnetic quantum dot micelles. *Contrast Media Mol. Imaging* **2011**, 6, 100-109.

The work discussed in this thesis was presented at the following international conferences:

- European Materials Research Society (EMRS) Meeting, May 2013, Strasbourg, France; two oral presentations.

- Materials Research Society (MRS) Spring Meeting, April 2013, San Francisco, CA, USA; two oral presentations and one poster presentation.

- NWO CW Meeting, February 2013, Veldhoven, The Netherlands, Oral presentation.

- International workshop on single molecule spectroscopy and ultrasensitive analysis in life sciences, 2011, Berlin, Germany. Poster presentation.

- International Conference on Luminescence and Optical Spectroscopy of Condensed Matter (ICL), 2011, Ann Arbor, MI, USA. Oral presentation. Early distinguished researcher prize.

- TMII symposium, 2011, New York, NY, USA; poster presentation.

- NaNaX4 2010, Munich, Germany; poster presentation, Best poster award.

Curriculum Vitae

Yiming Zhao was born on August 30th 1985 in Wuhan, China. In 2003, he obtained his high school diploma at No.1 Middle School Attached to Central China Normal University. In the same year, he began his chemistry studies at Wuhan University. He first came to Europe in September 2006, as an exchange student at University of Helsinki, Finland, where here he started to study polymer chemistry and research on thermal responsive polymer grafted on gold nanoparticles, under supervision of Prof. Heikki Tenhu. He decided to stay in Helsinki for his Master study and continue his polymer study. He obtained his Master of Science degree in January 2009 with grade excellent (5/5).

In February 2009, he joined the group of Condensed Matter and Interfaces (CMI) of the Debye Institute at Utrecht University, The Netherlands, as a PhD student, where he worked on a collaborative project under supervision of Prof. Andries Meijerink, Dr. Celso de Mello Donegá and Prof. Willem Mulder. As the project aimed at biomedical applications of luminescent nanocrystals, he performed chemical and physical studies on quantum dots and doped nanocrystals in Utrecht and biological studies in Mount Sinai School of Medicine (New York City). The results of his PhD research are described in this thesis, published in scientific journals, and presented at international conferences. He received a Best Poster Award at the NanaX 4 conference in 2010 (Munich, Germany) and the Early Distinguished Researcher Prize at the ICL conference in 2011 (Michigan, USA). During his PhD, he supervised three Master and two Bachelor students.